MINISTÉRIO DA CIÊNCIA, TECNOLOGIA E INOVAÇÃO
INSTITUTO NACIONAL DE PESQUISAS ESPACIAIS

sid.inpe.br/mtc-m21b/2015/01.30.12.04-TDI

DISCRETE MULTIOBJECTIVE OPTIMIZATION APPLIED TO THE SPACECRAFT ACTUATORS COMMAND PROBLEM AND TESTED IN A HARDWARE-IN-THE-LOOP RENDEZVOUS SIMULATOR

Willer Gomes dos Santos

Doctorate Thesis of the Graduate Course in Space Engineering and Technology/Space Mechanics and Control Division, guided by Drs. Evandro Marconi Rocco, and Toralf Boge, approved in February 26, 2015.

URL of the original document:
<http://urlib.net/8JMKD3MGP3W34P/3HRTNES>

INPE
São José dos Campos
2015

PUBLISHED BY:

Instituto Nacional de Pesquisas Espaciais - INPE
Gabinete do Diretor (GB)
Serviço de Informação e Documentação (SID)
Caixa Postal 515 - CEP 12.245-970
São José dos Campos - SP - Brasil
Tel.:(012) 3208-6923/6921
Fax: (012) 3208-6919
E-mail: pubtc@sid.inpe.br

COMMISSION OF BOARD OF PUBLISHING AND PRESERVATION OF INPE INTELLECTUAL PRODUCTION (DE/DIR-544):
Chairperson:
Marciana Leite Ribeiro - Serviço de Informação e Documentação (SID)
Members:
Dr. Gerald Jean Francis Banon - Coordenação Observação da Terra (OBT)
Dr. Amauri Silva Montes - Coordenação Engenharia e Tecnologia Espaciais (ETE)
Dr. André de Castro Milone - Coordenação Ciências Espaciais e Atmosféricas (CEA)
Dr. Joaquim José Barroso de Castro - Centro de Tecnologias Espaciais (CTE)
Dr. Manoel Alonso Gan - Centro de Previsão de Tempo e Estudos Climáticos (CPT)
Drª Maria do Carmo de Andrade Nono - Conselho de Pós-Graduação
Dr. Plínio Carlos Alvalá - Centro de Ciência do Sistema Terrestre (CST)
DIGITAL LIBRARY:
Dr. Gerald Jean Francis Banon - Coordenação de Observação da Terra (OBT)
Clayton Martins Pereira - Serviço de Informação e Documentação (SID)
DOCUMENT REVIEW:
Simone Angélica Del Ducca Barbedo - Serviço de Informação e Documentação (SID)
Yolanda Ribeiro da Silva Souza - Serviço de Informação e Documentação (SID)
ELECTRONIC EDITING:
Marcelo de Castro Pazos - Serviço de Informação e Documentação (SID)
André Luis Dias Fernandes - Serviço de Informação e Documentação (SID)

MINISTÉRIO DA CIÊNCIA, TECNOLOGIA E INOVAÇÃO
INSTITUTO NACIONAL DE PESQUISAS ESPACIAIS

sid.inpe.br/mtc-m21b/2015/01.30.12.04-TDI

DISCRETE MULTIOBJECTIVE OPTIMIZATION APPLIED TO THE SPACECRAFT ACTUATORS COMMAND PROBLEM AND TESTED IN A HARDWARE-IN-THE-LOOP RENDEZVOUS SIMULATOR

Willer Gomes dos Santos

Doctorate Thesis of the Graduate Course in Space Engineering and Technology/Space Mechanics and Control Division, guided by Drs. Evandro Marconi Rocco, and Toralf Boge, approved in February 26, 2015.

URL of the original document:
<http://urlib.net/8JMKD3MGP3W34P/3HRTNES>

INPE
São José dos Campos
2015

Cataloging in Publication Data

Santos, Willer Gomes dos.

Sa59d Discrete multiobjective optimization applied to the spacecraft actuators command problem and tested in a hardware-in-the-loop rendezvous simulator / Willer Gomes dos Santos. – São José dos Campos : INPE, 2015.

xxvi + 134 p. ; (sid.inpe.br/mtc-m21b/2015/01.30.12.04-TDI)

Thesis (Doctorate in Space Engineering and Technology/Space Mechanics and Control Division) – Instituto Nacional de Pesquisas Espaciais, São José dos Campos, 2015.

Guiding : Drs. Evandro Marconi Rocco, and Toralf Boge.

1. Actuators command 2. Spacecraft control system 3. Multiobjective optimization 4. Hardware-in-the-loop simulation 5. Orbital rendezvous I.Title.

CDU 629.7:519.863

Esta obra foi licenciada sob uma Licença Creative Commons Atribuição-NãoComercial 3.0 Não Adaptada.

This work is licensed under a Creative Commons Attribution-NonCommercial 3.0 Unported License.

Aprovado (a) pela Banca Examinadora em cumprimento ao requisito exigido para obtenção do Título de ***Doutor(a)*** em

Engenharia e Tecnologia Espaciais/Mecânica Espacial e Controle

Dr. Ijar Milagre da Fonseca

Presidente / ITA / SJCampos - SP

Dr. Evandro Marconi Rocco

Orientador(a) / INPE / SJCampos - SP

Dr. Toralf Boge

Toralf Boge

Orientador(a) / DLR / Alemanha - DE

Dr. Hans-Ulrich Pilchowski

Membro da Banca / INPE / SJCampos - SP

Dr. André Fenili

André Fenili

Convidado(a) / UFABC / Santo André - SP

Dr. Francisco das Chagas Carvalho

Francisco das Chagas Carvalho

Convidado(a) / ITA / São José dos Campos - SP

Este trabalho foi aprovado por:

( ) maioria simples

(X) unanimidade

Aluno (a): *Willer Gomes dos Santos*

São José dos Campos, 26 de Fevereiro de 2015

“Energy and persistence conquer all things”.

Benjamin Franklin

To him, who has already achieved the unknown but continues
present in my thoughts

ACKNOWLEDGEMENTS

The author of this thesis would like to thank his advisers, Dr. Evandro Marconi Rocco and Dr. Toralf Boge, for their advices and guidances throughout the PhD project. Without their assistance, this thesis would not have been possible. I would also like to thank my colleagues from the EPOS team at DLR, Heike Benninghoff and Florian Rems, for their support and persistence during the tests at EPOS facility. It also deserves acknowledgment my colleagues from the Space Mechanics and Control Division at INPE who have contributed with their relevant comments. I also express my gratitude to the members of the examiner committee for their valuable comments and suggestions which have improved the quality of this work. Finally but not less important, I thank to the CNPq and CAPES for their financial support during the PhD program (process number BEX 3512/13-4).

ABSTRACT

The challenge of commanding efficiently and autonomously spacecraft actuators has motivated the investigation of new optimization techniques in order to extend the spacecraft's life and to insure the fulfillment of all mission requirements. The control problem of spacecraft using actuators with conflicting characteristics has been explored in this thesis. Thus a novel autonomous command strategy based on a discrete multiobjective optimization approach has been proposed herein. This innovative methodology, called Actuator Multiobjective Command Method (AMCM), determines the best way to operate a given group of actuators according to predefined specifications and online acquired inputs. This function generates a set of feasible solutions and selects, based on a decision making method, the best compromise solution optimizing a group of objective functions simultaneously and completely online. It is assumed the final approach rendezvous scenario, due to its complexity, for testing the models. In addition, the hardware-in-the-loop rendezvous and docking simulator facility of the German Aerospace Center, called European Proximity Operations Simulator (EPOS), has been used to test and validate the proposed method. This facility uses two industrial robots to physically simulate the complete translational and rotational motion of two docking satellites. Furthermore, all elements of the guidance, navigation, and control loop have been developed and implemented accurately in a simulation framework and tested, at EPOS, under real-time environment conditions using rendezvous sensor-hardware. The developed software brings forward effectiveness and robustness proving to be able to generate reliable results in both non-real-time and real-time simulations.

Keywords: Actuators command. Spacecraft control system. Multiobjective optimization. Hardware-in-the-loop simulation. Orbital rendezvous.

OTIMIZAÇÃO MULTIOBJETIVO DISCRETA APLICADA AO PROBLEMA DE COMANDO DE ATUADORES DE SATÉLITE E TESTADA EM UM SIMULADOR DE APROXIMAÇÃO COM HARDWARE NA MALHA

RESUMO

O desafio de comandar eficientemente e autonomamente os atuadores de um veículo espacial tem motivado a investigação de novas técnicas de otimização a fim de prolongar a vida útil do veículo e garantir o cumprimento de todos os requisitos da missão. O problema de controle de espaçonaves usando atuadores com características conflitantes foi explorado nesta tese. Assim, uma nova estratégia de comando autônoma, baseada em uma abordagem de otimização multiobjectivo discreta, é proposta neste documento. Esta inovadora metodologia, chamada aqui de Método de Comando Multiobjetivo de Atuador (AMCM em inglês), determina o melhor modo de operar um dado grupo de atuadores de acordo com especificações predefinidas e dados adquiridos em tempo-real. Esta função gera um conjunto de soluções viáveis e seleciona, de acordo com um método de tomada de decisão, a melhor solução compromisso otimizando, consequentemente, um grupo de funções objetivos simultaneamente. O cenário de uma manobra de aproximação final é escolhido, devido a sua complexidade, para testar os modelos. Ademais, o simulador de encontro e acoplamento com hardware na malha do Centro Aeroespacial Alemão, chamado de Simulador Europeu de Operações de Proximidade (EPOS em inglês), foi utilizado para testar e validar os modelos propostos. Este simulador utiliza dois robôs industriais para fisicamente simular o movimento translacional e rotacional completo de dois satélites em operação de aproximação e acoplamento. Além disso, todos os elementos da malha de guiamento, navegação, e controle foram desenvolvidos e implementados em um ambiente de simulação e testados em tempo real no EPOS utilizando sensores reais. O software desenvolvido apresenta eficácia e robustez provando ser capaz de gerar resultados confiáveis tanto em simulações numéricas quanto em simulações em tempo real.

Palavras-chave: Comando de atuadores. Sistema de controle de satélites. Otimização multiobjetivo. Simulação com hardware na malha. Encontro orbital.

LIST OF FIGURES

Page

1.1 Typical automatic control system. 1
1.2 Spacecraft missions concerned with the mixed actuators problem: (a) Dawn spacecraft; (b) FUSE spacecraft; and (c) Cassini spacecraft. 2

2.1 Block diagram of the coupled rendezvous and attitude GNC loop. 8
2.2 Local orbital frame and inertial frame. 9
2.3 Relative motion starting from the R-bar axis. 12
2.4 Linearization error of the relative motion simulation. 12
2.5 ATV's reaction control system. 20
2.6 Characteristics of the thrust pulse. 21
2.7 Functional concept of the thruster management function (TMF). 24
2.8 An illustrative example of a reaction wheel. 24
2.9 Electromechanical model of a reaction wheel. 25
2.10 An illustrative example of magnetic torqrods. 26
2.11 Magnetic torque direction. 27
2.12 Component failure rate as a function of age (bathtub curve). 29
2.13 Pinhole model of the camera CCD sensor. 31
2.14 Expected error as function of the approach range. 32
2.15 Velocity profile used by the rendezvous guidance system. 33
2.16 Preference level and dominance relation. 35
2.17 Common shapes of Pareto front considering two objective functions. . . . 36
2.18 Representation of the ideal point and the nadir point. 37
2.19 Graphical representation of Weighted Sum Method. 40
2.20 The Smallest Loss Criterion. 42
2.21 Architecture of the Spacecraft Rendezvous and Attitude Simulator. . . . 44

3.1 Block diagram of the linear time-invariant control system. 45
3.2 Step response of the linear closed-loop for each actuator. 49
3.3 Closed-loop poles for a range of actuators' gains in the complex plane. . 50
3.4 Closed-loop zeros for a range of actuators' gains in the complex plane. . . 50
3.5 Settling time versus overshoot: the objective space and the Pareto front. 52
3.6 Flowchart of the multiobjective optimization process applied to the optimal design problem. 53
3.7 Step response of the linear closed-loop of the best compromise solutions. 54

4.1 Functional concept of the Actuator Multiobjective Command Method I. . 61

4.2 Flowchart of the multiobjective optimization process of AMCM-I. 62
4.3 Thrusters' location and orientation ($n = 12$). 63
4.4 Tradeoff scenario for the mixed actuators problem. 65
4.5 Combinatorial space of the discrete multiobjective problem: (a) 3D representation; (b) 2D representation. 66
4.6 Value path plot of AMCM-I for requested torque level of 0.015 Nm. . . . 67
4.7 Value path plot of AMCM-I for requested torque level of 0.050 Nm. . . . 67
4.8 Value path plot of AMCM-I for requested torque level of 0.085 Nm. . . . 68
4.9 AMCM-I commanded torque: (a) requested torque of 0.015 Nm; (b) requested torque of 0.050 Nm; (c) requested torque of 0.085 Nm. 69
4.10 Time angular response of different operation modes. 70
4.11 Performance parameters of the GNC loop: (a) angular error integrated over time; (b) fuel consumption; (c) electric charge consumption; (d) settling time of the angular response; (e) disturbance of coupling (normalized Z_3); and (f) risk of utilization (normalized Z_4). 71
4.12 Time translational position response of a spacecraft composed of actuators commanded by AMCM-I. 73
4.13 Time translational velocity response of a spacecraft composed of actuators commanded by AMCM-I. 73
4.14 Approach motion in target centered frame. 74
4.15 AMCM-I: GNC loop errors including the real position (left) and the guidance position (right). 74
4.16 Time angular response of a spacecraft composed of actuators commanded by AMCM-I. 75
4.17 Frequency of activation of each actuator. 76
4.18 Force pulses applied by the RCS (left) and total torque applied by reaction wheels, magnetic torqrods, and RCS (right). 77
4.19 Torque applied by the reaction wheels as a function of time. 77
4.20 Torque applied by the magnetic torqrods as a function of time. 78
4.21 Input voltage commands (left) and angular velocity (right) of the reaction wheels as a function of time. 78
4.22 Electromagnetic dipole moment commands of the magnetic torqrods as a function of time. 79
4.23 Propellant mass (left) and electric charge (right) consumptions as a function of time. 79

5.1 Functional concept of the Actuator Multiobjective Command Method II (AMCM-II). 83
5.2 Flowchart of the multiobjective optimization process of AMCM-II. 85

5.3 Thrusters' location and orientation ($n = 16$). 86
5.4 Value path plot of AMCM-II using all candidate solutions. 87
5.5 Value path plot of AMCM-II using only non-dominated solutions. 88
5.6 Time pulse activation: (a) solution 33, approach using all candidate solutions; (b) solution 78, approach using only non-dominated solutions. . . 88
5.7 Objective values for a single control cycle: (a) force error; (b) torque error; (c) propellant consumption; and (d) number of pulses. 89
5.8 Number of candidates and non-dominated solutions as a function of time. 89
5.9 Time translational (left) and angular response (right) of the final approach rendezvous. 90
5.10 AMCM-II: GNC loop errors including the real position (left) and the guidance position (right). 91
5.11 Force (left) and torque (right) pulses applied by the RCS of 16 thrusters. 91
5.12 Force (left) and torque (right) pulses, applied by the RCS of 16 thrusters, of a brief period of simulation. 92
5.13 Accumulated objective values throughout the simulation: (a) force error; (b) torque error; (c) propellant consumption; and (d) number of pulses. . 93
5.14 Objective values as a function of thrust level and nozzle inclination parameters: (a) force error (Z_1); (b) torque error (Z_2); (c) propellant consumption (Z_3); and (d) number of pulses (Z_4). 94
5.15 Failure scenario of the Case f1: (a) failure signal; (b) faulty thrusters. . . 96
5.16 Approach motion (left) and time angular response (right) for every failure cases. 96
5.17 Objective values of the failure scenario: (a) accumulated force error; (b) accumulated torque error; (c) propellant consumption; and (d) total number of pulses. 97

6.1 The robots of the European Proximity Operations Simulator (EPOS). . . 99
6.2 Components of EPOS system. 101
6.3 Concept of the EPOS control system. 101
6.4 EPOS control room. 102
6.5 Set-up of EPOS in closed-loop control system. 104
6.6 EPOS architecture for contact dynamic simulation. 105
6.7 Set-up for lander application simulation. 105
6.8 Ideal Robot Joint Coordinate (IJT). 106
6.9 Tool Coordinate System (left) and Base Coordinate System (right). . . . 106
6.10 Global Laboratory Coordinate System (GLB). 107
6.11 Closed-loop simulation concept including AMCM. 108
6.12 Visual camera sensor coupled to Robot 2. 108

6.13 Tracking edges of the target mock-up at 10 m (left) and 20 m (right). . . . 109
6.14 EPOS simulation mode. 110
6.15 Commanded translational (left) and rotational (right) position as a function of time: ideal actuator case. 111
6.16 Commanded translational (left) and rotational (right) position as a function of time: AMCM-I case. 112
6.17 Commanded translational (left) and rotational (right) position as a function of time: AMCM-II case. 112
6.18 Relative position error of the real camera sensor: ideal actuator case. . . . 113
6.19 Relative position error of the real camera sensor: AMCM-I case. 114
6.20 Relative position error of the real camera sensor: AMCM-II case. 114
6.21 Applied force (left) and torque (right) as a function of time: ideal actuator case. 115
6.22 Applied force (left) and torque (right) as a function of time: AMCM-I case. 116
6.23 Applied force (left) and torque (right) as a function of time: AMCM-II case. 116
6.24 Estimated position (left) and velocity (right) as a function of time: ideal case. 117
6.25 Estimated position (left) and velocity (right) as a function of time: AMCM-I case. 117
6.26 Estimated position (left) and velocity (right) as a function of time: AMCM-II case. 118
6.27 Motion of the Robot 1 in the IJT coordinate frame for the AMCM-I case. 118
6.28 Motion of the Robot 2 in the IJT coordinate frame for the AMCM-I case. 119

LIST OF TABLES

Page

3.1 Parameters of the linear closed-loop control system. 48
3.2 Best compromise solution and extreme cases of the design optimization problem. 54
3.3 Performance overall mean analysis of the design optimization problem. . 55

4.1 Combination table which solves the combinatorial problem. 59
4.2 Simulation parameters. 64
4.3 Performance overall mean analysis of the mixed actuators problem. . . . 72

5.1 RCS parameters for configuration with 16 thrusters. 86
5.2 Performance overall mean analysis of the thrusters operation problem. . 93
5.3 Thrusters failure case's parameters. 95

6.1 EPOS motion capabilities. 103
6.2 EPOS test plan. 110

LIST OF ABBREVIATIONS

ACS – Application Control System
AMCM – Actuator Multiobjective Command Method
AOCS – Attitude and Orbit Control System
ATV – Automated Transfer Vehicle
CCD – Charge Coupled Device
CDF – Concurrent Design Facility
CEF – Concurrent Engineering Facility
CLW – Clohessy Wiltshire Coordinate System
CoM – Center of Mass
DLR – *Deutsches Zentrum für Luft-und Raumfahrt*
EPOS – European Proximity Operations Simulator
FMC – Facility Monitoring and Control
FUSE – Far Ultraviolet Spectroscopic Explorer
GLB – Global Laboratory Coordinate System
GNC – Guidance, Navigation, and Control
HIL – Hardware-in-the-loop
HTV – H-II Transfer Vehicle
IDC – Ideal Robot Device Coordinate System
IGRF – International Geomagnetic Reference Field
IA – Ideal Actuator approach
IJT – Ideal Robot Joint Coordinate
LEO – Low Earth Orbit
LP – Linear Programming
LRC – Local Robot Control
MIB – Minimum Impulse Bit
MDO – Multidisciplinary Design Optimization
ESOPRoM – Simultaneous Engineering and Multidisciplinary Design Optimization
PID – Proportional-Integral-Derivative
PWPF – Pulse Width Pulse Frequency
RCS – Reaction Control System
RvD – Rendezvous and Docking
SLC – Smallest Loss Criterion
SRAS – Spacecraft Rendezvous and Attitude Simulator
TIMED – Thermosphere, Ionosphere, Mesosphere Energetics and Dynamics
TCS – Tool Coordinate System
TMF – Thruster Management Function
WSM – Weighted Sum Method

LIST OF SYMBOLS

$\mathbf{A}$ – configuration matrix
$\mathbf{B}$ – Earth's magnetic field matrix
$\mathbf{c}, \mathbf{i}, \mathbf{r}$ – multiobjective coefficients
F – requested force and torque vector
F^a – force and torque applied by the reaction control system
F_n – thrust nominal force
G_x, G_y, G_z – gravity gradient moments
$\dot{h}_w$ – reaction wheel torque
$\mathbf{I}_f$ – final specific impulse vector
I_{sp} – specific impulse
$\mathbf{J}_s$ – satellite's moment of inertia
$\mathbf{m}$ – magnetic dipole moment
m_c, m_t – spacecraft mass
m_p – propellant mass
n – number of decision variables
$\mathbf{p}$ – combinatorial vector
$\mathbf{P}$ – average thrust applied by the reaction control system
$\mathbf{q}$ – quaternion
$\mathbf{r}$ – vector radius
$\mathbf{r}_b$ – thruster distance vector from the center of mass of the vehicle body
t – thruster activation
t_{pulse} – pulse length command
$\mathbf{T}_c$ – controller's torque command
$\mathbf{T}_{db}$ – external disturbance torque
$\mathbf{T}_m$ – magnetic control torque
$\mathbf{T}_r$ – reaction control system control torque
T^a_r, T^a_w, T^a_m – test torque theoretical functions of actuators
$u(h)$ – discrete control signal
$\mathbf{x}$ – decision variable vector
$\mathbf{x}^b$ – best compromise solution
$\mathbf{x}^*$ – ideal solution
$\mathbf{Z}(\mathbf{x})$ – vector of objective functions
α – thruster's elevation angle
β – thruster's azimuth angle
$\bar{\eta}$ – performance overall mean
μ – Earth's gravitational constant
ω_s – satellite angular velocity
ω_w – flywheel angular velocity
ϕ – rotation around the X_b axis (Euler angle)
ψ – rotation around the Z_b axis (Euler angle)

ρ – atmospheric density
θ – rotation around the Y_b axis (Euler angle)
Δh_a – actuator sample period
Δh_c – control cycle
$\Delta \gamma_D$ – differential drag force per unit of mass
$\mathbf{\Omega}$ – skew-symmetric matrix of the angular velocity

Subscripts

c – chaser vehicle
m – magnetic torqrod
r – reaction control system
t – target vehicle
w – reaction wheel

CONTENTS

Page

1 INTRODUCTION 1
1.1 Objectives 5
1.2 Thesis Structure 6

2 MATHEMATICAL MODELING OF THE GNC LOOP 7
2.1 Overview 7
2.2 Relative Motion Dynamics 8
2.2.1 Hill equations 10
2.2.2 Analysis of the relative motion dynamics 11
2.3 Attitude dynamics and kinematics 13
2.4 Environmental disturbances in the translational and rotational motions . 17
2.4.1 Translational disturbance: Residual atmospheric drag 18
2.4.2 Rotational disturbance: Gravity gradient moment 18
2.5 Discrete PID Controller 19
2.6 Actuators 20
2.6.1 Reaction Control System 20
2.6.2 Reaction Wheels 24
2.6.3 Magnetic Torqrods 25
2.6.4 Basic concept of reliability 28
2.7 Navigation System 30
2.8 Guidance System 32
2.9 Multiobjective Optimization 33
2.9.1 Solution methods of multiobjective optimization problems 37
2.9.1.1 Weighted Sum Method 39
2.9.1.2 Smallest Loss Criterion 41
2.10 Spacecraft Rendezvous and Attitude Simulator 42

3 DESIGN OF A LINEAR TIME-INVARIANT CONTROL SYSTEM 45
3.1 Problem definition 45
3.2 Numerical analysis 47
3.3 Discrete multiobjective optimization approach 51

4 AMCM-I: A SOLUTION TO THE MIXED ACTUATORS PROBLEM 57
4.1 Actuator Multiobjective Command Method I 57
4.2 RCS Configuration 61
4.3 Purely Numerical Simulations 63
4.3.1 Control Cycle Analysis 65
4.3.2 Comparative Analysis of AMCM-I 69
4.3.3 Complete Rendezvous and Attitude Simulation using AMCM-I 72

5 AMCM-II: A SOLUTION TO THE REAL-TIME OPERATION PROBLEM OF SPACECRAFT THRUSTERS 81
5.1 Actuator Multiobjective Command Method II 81
5.2 RCS Configuration 84
5.3 Purely Numerical Simulations 84
5.3.1 Control Cycle Analysis 84
5.3.2 Complete Rendezvous and Attitude Simulation using AMCM-II 89
5.3.3 Thruster Design Analysis 93
5.3.4 A Thruster Failure Case 95

6 VALIDATION TESTS AT EPOS FACILITY 99
6.1 About EPOS 2.0 100
6.1.1 Control concept 100
6.1.2 Capabilities and performances 103
6.1.3 Facility simulation methods 103
6.1.4 EPOS coordinate systems 104
6.2 EPOS test campaign 107
6.3 Results based on HIL Rendezvous Simulations 111

7 CONCLUSIONS AND COMMENTS 121
7.1 Contributions 123
7.2 Future works 124

REFERENCES 125

1 INTRODUCTION

Actuators are devices or mechanisms capable of converting energy - typically electric current, hydraulic fluid pressure, or pneumatic pressure - into action, or motion in case of a mechanical system. The verb *actuate* comes from Medieval Latin *actuatus* (circa 1590s) and from Latin *actus*, past participle of *agere* which means "to do, set in motion, chase, stir up". Someone can find hundred actuators in his daily life at home, transport, work, and entertainment, but most people are scarcely aware of them. Some examples of actuators are solenoids, electric motors, hydraulic and pneumatic cylinders. Usually, they belong to a larger system, called automatic control system (Figure 1.1), that may includes also many sensors, processing elements, as well as auxiliary components such as power supplies and drive mechanisms. Early rudimentary applications of automatic control system appeared in Greece around 270 B.C. with the development of float regulator mechanisms, such as the water clock of Ktesi-bios (BENNETT, 1996).

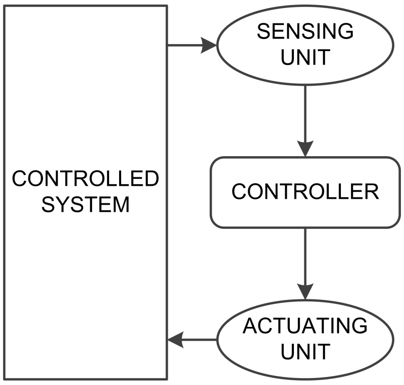

Figure 1.1 - Typical automatic control system.

Electric motors have existed since its invention in 1824 by Michael Faraday (IDA, 2014) whereas actuators based on thermal expansion have been used since the mid-1880s. Most applications of automatic control system in 19th century had the basic objectives of controlling temperatures, pressures, liquid levels, and the speed of rotating machinery. Nowadays, actuators are used for almost all conceivable applications and they are found in all engineering disciplines. In fact, with the growth of advanced machines and instruments with higher performance, new outstanding actuators have been developed in several field of applications, such as industry, medicine, welfare, global environment, and space engineering. Those innovative actuators - which include for example: smart material actuators, micro-actuators, nano-actuators - represent the key technology for the next generation (HIGUCHI et al., 2010).

Several categories can be used to classify an actuator, such as power output, range and type of motion, resolution, accuracy, peak force/torque, heat dissipation, speed characteristics, frequency response, power requirements, among others (BISHOP, 2002). Therefore, they are critical components of every control system. Within the context of spacecraft missions, the performance and robustness of an attitude and orbit control subsystem (AOCS) is highly dependent on sensors and actuators. The most common spacecraft actuators are thrusters, reaction wheels, and magnetic torqrods. Those devices are designed to provide force and/or torque throughout the spacecraft's life in order to counteract orbital disturbances and to perform attitude and orbital maneuvers. Thrusters can provide force and/or torque whereas reaction wheels and magnetic torqrods are on-board actuators used only for attitude control. This thesis is concerned with two fields of the spacecraft operations: the mixed actuators problem and the thrusters operation problem.

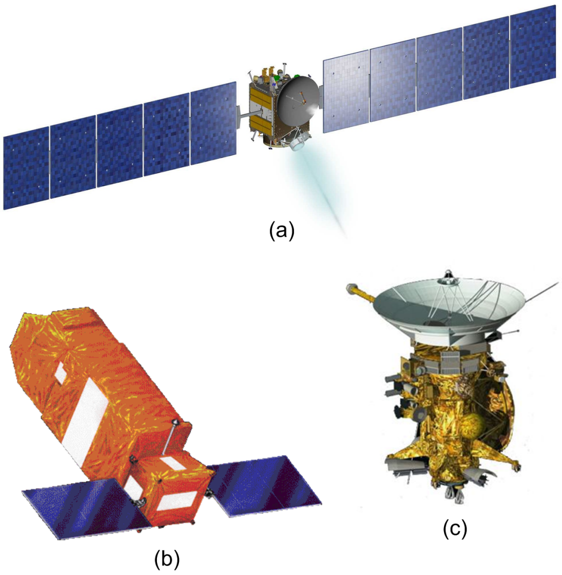

Figure 1.2 - Spacecraft missions concerned with the mixed actuators problem: (a) Dawn spacecraft; (b) FUSE spacecraft; and (c) Cassini spacecraft.

Over the past years, the spacecraft control problem by using mixed actuators have been the subject of extensive study in several space missions (Figures 1.2). A mixed actuators mode is a hybrid approach to control the spacecraft using a combination of actuators. A hybrid attitude control mode might be used as a contingency means for controlling a spacecraft that has lost the use of one or more of its operating reaction wheels. The first NASA Spacecraft Hybrid Attitude Workshop, that was held in Maryland in April of 2013, aimed to better understand the technical challenges, risks, and benefits of a potential hybrid attitude control mode operations on their science mission spacecraft. Example of such missions include Kepler, Dawn, Mars Odyssey, Cassini, Far Ultraviolet Spectroscopic Explorer (FUSE), and Thermosphere, Ionosphere, Mesosphere Energetics and Dynamics (TIMED). This NASA's interest is driven by a number of recent reaction wheel failures on aging (DENNEHY, 2014).

Won (1999) compares several control methods for attitude control of a satellite with thrusters, magnetic torques and reaction wheels. Tracking control laws for a control system with three momentum wheels and a set of thrusters are implemented in Hall et al. (2002). Reaction wheels failures in the FUSE satellite prompted modifications of the three-axis attitude-control so that to restore its functionality using a hybrid controller with magnetic torqrods and reaction wheels (ROBERTS et al., 2004). A mixed mode using reaction wheels and thrusters has also been uploaded to the spacecraft Dawn in early 2011 (BRUNO, 2012). Recently, Macala et al. (2014) have evaluated the feasibility of using two reaction wheels and a set of thrusters in a contingency scenario in order to meet the Cassini spacecraft pointing requirements. Their results indicated that better attitude-control performance can be achieve with a hybrid approach.

Another interesting problem which has received great attention is the real-time operation of the Reaction Control System (RCS). The RCS technology uses a set of thrusters in a special set-up to provide force and torque simultaneously (SIDI, 1997; LEY et al., 2009). RCS is commanded by modulated firing pulses that allow the control of translational and rotational motion on all axes. The purpose of the on-board thruster management function (TMF) is to select specific thrusters and to calculate their firing command duration in order to realize the force and torque commands requested by the spacecraft's controller. RCS can be used for attitude-control during re-entry, for station-keeping in orbit, for close maneuvering during docking procedures, among others applications. Recently, some new optimization algorithms in this field have been proposed, especially investigations concerning the optimal thruster combinations table in order to simplify real-time on-board computations (ANKERSEN et al., 2005; SERVIDIA; NA, 2005; WANG; XIE, 2009). In particular, considerable effort has been made to improve the TMF of the Automated Transfer Vehicle (ATV) responsible for carrying out replenishment missions to the International Space Station (GONNAUD; PASCAL, 2000; SILVA et al., 2006). In general, research focuses on the optimization of a single objective function, usually the fuel consumption (WIKTOR, 1994; JIN et al., 2006), to determine the best selection of thrusters.

Due to the increasingly strict economical constraints, space agencies have encouraged the developments of new optimization algorithms to be applied to the spacecraft control. In order to meet the multidisciplinary tasks of the control system, multi-objective optimization methods have been proposed as an alternative approach to conventional optimization techniques (COHON, 2003). A survey of multiobjective optimization methods for application in engineering has been presented by Marler and Arora (2004). This field has attracted considerable attentions in recent decades and many results have been reported (BALS et al., 1997; FAN et al., 2002; LUO et al., 2007; MORADI et al., 2010; ZHANG; ZENG, 2012; ROCCO et al., 2002; VENDITTI et al., 2010). An interesting example is the integration of multidisciplinary design optimization (MDO) with the concurrent engineering methodology of a space mission. MDO allows designers to consider all relevant disciplines simultaneously. The optimum of the simultaneous problem is superior to the design found by optimizing each discipline sequentially, since it can exploit the interactions between the disciplines. Some space centers that have used this methodology are the *Concurrent Design Facility* (CDF) from ESA, *Concurrent Engineering Facility* (CEF) from DLR, *TeamX* from NASA, and the *Simultaneous Engineering and Multidisciplinary Design Optimization* (ESOPRoM) from INPE (CHAGAS et al., 2014; LAU et al., 2014).

An effective and well established technique for testing complex real-time embedded systems is through hardware-in-the-loop (HIL) simulations. The basic concept of HIL simulations is to include a real hardware in the simulation loop instead of using just purely mathematical models. Furthermore, the testing and evaluation of the system are carried out in real-time. HIL simulations have been used for more than 40 years and one of the first uses was for flight simulation (BASIC, 2005). Nowadays, HIL simulations have been applied to several fields, such as automotive, power engineering, robotics, space systems, offshore systems, among others. Numerical analysis of the limit cycle of the RCS and their validation through HIL simulations is presented by Jeon and Jung (2012). In this thesis, the proposed models have been integrated and tested in the HIL rendezvous and docking simulator of the German Aerospace Center, called European Proximity Operations Simulator (EPOS) (BOGE et al., 2012). Recently, many relevant experiments have been carried out at this facility (MA. et al., 2012; BENNINGHOFF et al., 2014) which uses two industrial robots to physically simulate the complete translational and rotational motion of two docking satellites.

At EPOS, the entire guidance, navigation, and control (GNC) loop is tested under real-time conditions using rendezvous sensor-hardware. Inputs and outputs of an embedded system (here: a visual camera sensor) are connected to a correspondent counterpart - called HIL-simulator - which simulates the real environment of the system.

1.1 Objectives

The main objective of this thesis is to explore the actuators arrangements and associated operations strategies for spacecraft control problems and to propose a novel solution based on multiobjective optimization techniques. Four design requirements have been taken into account: flexible software architecture; optimal control; autonomous decision making; and computational efficiency. That means the proposed software should have an architecture as flexible as possible that permits substitution of actuators models without flight software code modifications. The optimization method should occur autonomously and online. In addition, it is worth mentioning that it is not the purpose of this thesis to analyze and quantify the computational load of the proposed algorithm. Here, computational efficiency means that the optimization algorithm be able of running in a real-time environment.

The proposed models should be tested in the scenario of rendezvous close approach, due to the complexity of this process, taking into account the coupling between the rendezvous and attitude closed-loop control systems. Models for all components of the complete GNC loop have to be developed and implemented accurately in a simulation framework. Moreover, specific objectives can be addressed:

a) Develop a novel approach to solve the command problem of spacecraft actuators with conflicting characteristics. The actuators model shall include RCS, reaction wheels, and magnetic torqrods.

b) Propose a novel solution to the real-time operation problem of RCS considering a group of conflicting objectives to be optimized simultaneously rather than a single optimization problem.

c) Validate the proposed methods in a real-time environment through HIL simulations.

1.2 Thesis Structure

Chapter 2 covers the necessary background and concepts for the comprehension of the proposed methods. Every component of the GNC loop is described in detail. An optimal design of a linear time-invariant control system based on multiobjective optimization is discussed in Chapter 3. Chapter 4 presents the proposed solution to the mixed actuators problem whereas the real-time operation problem of RCS is analyzed and solved in Chapter 5. The validation of the proposed methods through HIL simulations is described in Chapter 6. Final conclusions and comments are drawn in Chapter 7.

2 MATHEMATICAL MODELING OF THE GNC LOOP

In this chapter the notation, formulation, and modeling of the spacecraft control system are presented. The objective here is to provide the fundamental background for the comprehension of the following chapters. Readers who have studied the topic will find this like a review while those with no background can consider it an introduction to the topic. For a complete development of the theory, the reader is referred to the references indicated throughout the chapter. Concerning the formulation assumed in this thesis, the vectors are defined as column vectors and they are expressed, as well as matrices, in bold letters.

2.1 Overview

The realistic motion of the final approach rendezvous process of two satellites is implemented in numerical models. Rendezvous and docking (RvD) technology is a key element in space missions such as assembly in orbit of larger units, re-supply of orbital platforms, exchange of crew in orbital stations, on-orbiting services, among others. RvD techniques have been studied and improved since its first execution in 1966 (FEHSE, 2003). The rendezvous process consists of a sequence of orbital maneuvers and controlled trajectories where the active vehicle (chaser) is successively led into the vicinity of, and eventually into contact with, the target vehicle. During the final approach phase, AOCS plays an important role mainly because the chaser's six degrees of freedom of motion must be simultaneously controlled. In general, the chaser vehicle approaches using closed-loop controlled straight line trajectories while the docking port of the target vehicle is continuously acquired and followed. Actually exist several strategies of performing the approach to the target vehicle, as described in Fehse (2003).

A complete block diagram of the coupled rendezvous and attitude GNC loop is depicted in Figure 2.1. The chaser's GNC system has to act so that the relative position and velocity become zero and it has to simultaneously synchronize the attitude of both spacecraft. The translational motion is controlled via thrusters whereas the attitude control system can use thrusters, reaction wheels and/or magnetic torqrods. The GNC loop has multiple sample times (FEHSE, 2003): the actuators models work with a frequency of 100 Hz; the relative pose estimation is provided with an update rate of 5 Hz; the controller, guidance, and attitude sensor models work with 10 Hz, whereas the dynamics models execute with a frequency of 250 Hz. The hearth of this thesis is the model highlighted by a red block, called Actuator Multiobjective Command Method, which has the main function of optimally commanding the actuators. This model will be widely discussed afterward in Chapters 4 and 5. The remaining models are separately explored in the following sections.

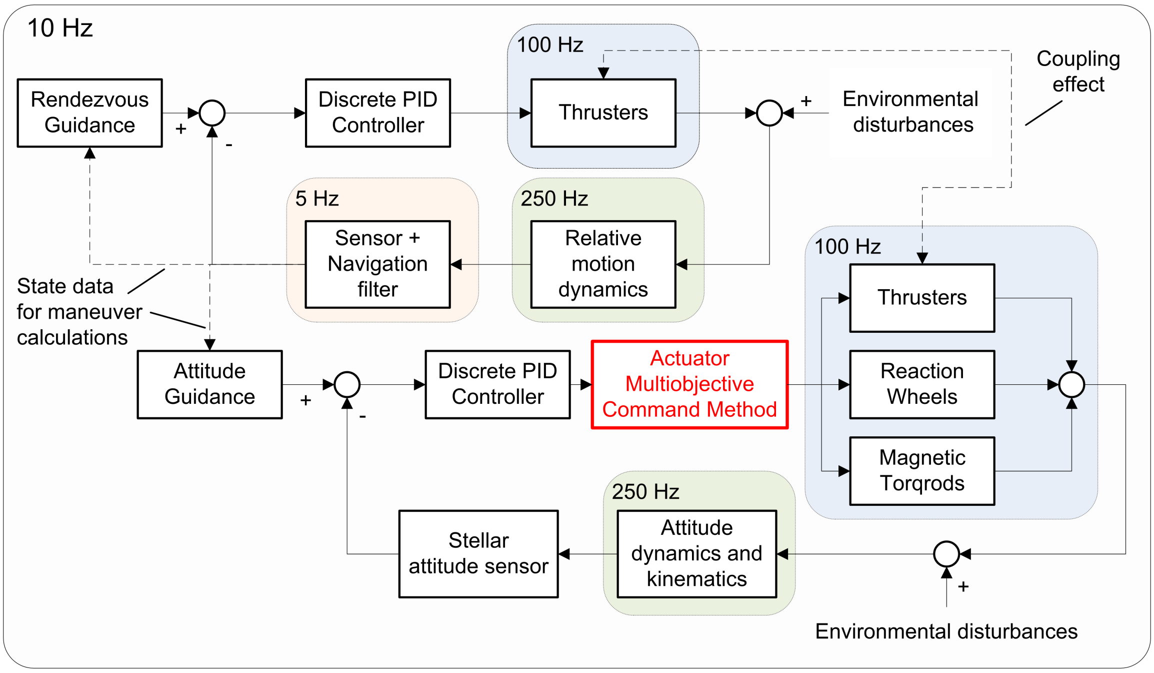
10 Hz
Rendezvous Guidance
+
-
Discrete PID Controller
100 Hz
Thrusters
+
Environmental disturbances
Coupling effect
5 Hz
Sensor + Navigation filter
250 Hz
Relative motion dynamics
100 Hz
Thrusters
State data for maneuver calculations
Attitude Guidance
+
-
Discrete PID Controller
Actuator Multiobjective Command Method
Reaction Wheels
Magnetic Torqrods
250 Hz
Stellar attitude sensor
Attitude dynamics and kinematics
+
Environmental disturbances

Figure 2.1 - Block diagram of the coupled rendezvous and attitude GNC loop.

2.2 Relative Motion Dynamics

During the close range rendezvous the chaser is a few tens of meters from the target and therewith the relative navigation assumes greater importance. Consider X, Y and Z as axes of the inertial coordinate frame and x, y and z as the axes of the target centered local orbital frame, also called in the rendezvous literature by V-bar, H-bar, and R-bar, respectively; $\mathbf{r}_c$ and $\mathbf{r}_t$ are the vector radius of the chaser and target, respectively, as shown in Figure 2.2.

Hence the relative acceleration, $\ddot{\mathbf{s}} \in \mathbb{R}^6$ can be expressed as

$$\ddot{\mathbf{s}} = \ddot{\mathbf{r}}_c - \ddot{\mathbf{r}}_t \tag{2.1}$$

General equations for motion under the influence of a central force are written as (FEHSE, 2003)

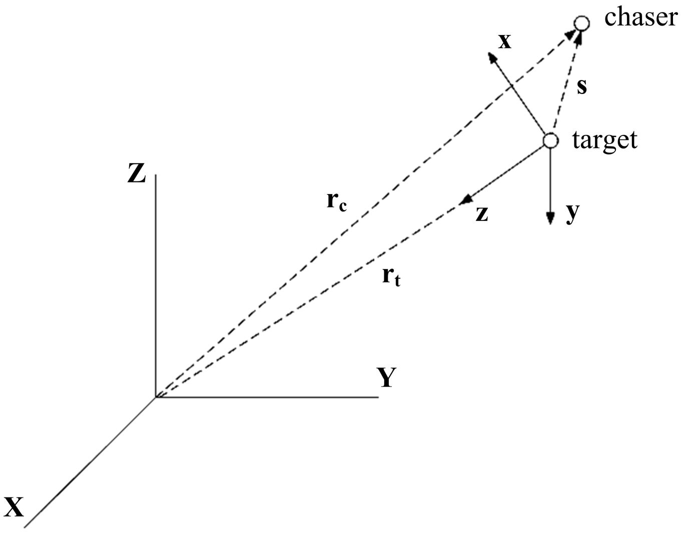

Figure 2.2 - Local orbital frame and inertial frame.

$$\begin{aligned}\ddot{\mathbf{r}}_t &= -\mu\frac{\mathbf{r}_t}{r_t^3} \\ \ddot{\mathbf{r}}_c &= -\mu\frac{\mathbf{r}_c}{r_c^3} + \mathbf{f}_u\end{aligned} \tag{2.2}$$

where μ is the Earth's gravitational constant and $\mathbf{f}_u \in \mathbb{R}^3$ is the specific force vector of control. The Equations 2.1 and 2.2 represent the nonlinear dynamics of the system.

Given the target absolute state (position and velocity) and the chaser relative state in the inertial coordinate frame, we can obtain the chaser absolute state by the following equations

$$\begin{aligned}\mathbf{r}_c &= \mathbf{r}_t + \mathbf{s} \\ \dot{\mathbf{r}}_c &= \dot{\mathbf{r}}_t + \dot{\mathbf{s}} + \boldsymbol{\omega} \times \mathbf{s}\end{aligned} \tag{2.3}$$

where $\boldsymbol{\omega} \in \mathbb{R}^3$ is the orbital angular velocity vector, whose value can be found by,

$$\boldsymbol{\omega} = \frac{\mathbf{h}_o}{r_t^2} \tag{2.4}$$

and $\mathbf{h}_o \in \mathbb{R}^3$ is the orbital specific angular momentum.

Usually, the initial relative state is provided in the target centered local orbital frame. However, to obtain the chaser absolute state is necessary the transformation to the inertial coordinate frame. The unit vectors of the local orbital frame are mathematically defined as (FEHSE, 2003),

$$\begin{aligned} \hat{\mathbf{x}} &= \hat{\mathbf{y}} \times \hat{\mathbf{z}} \\ \hat{\mathbf{y}} &= -\hat{\mathbf{h}}_o \\ \hat{\mathbf{z}} &= -\hat{\mathbf{r}}_t \end{aligned} \tag{2.5}$$

The direction cosine matrix, $\mathbf{A}_c \in \mathbb{R}^{3\times3}$, consists of unit vectors components and it is given by

$$\mathbf{A}_c = \begin{bmatrix} \hat{\mathbf{x}}^T \\ \hat{\mathbf{y}}^T \\ \hat{\mathbf{z}}^T \end{bmatrix} \tag{2.6}$$

The relative state vector in the inertial coordinate frame can be obtained according to the following transformation (SIDI, 1997)

$$\mathbf{s} = \mathbf{A}_c^T \mathbf{s}_b \tag{2.7}$$

where $\mathbf{s}_b \in \mathbb{R}^6$ is the relative state vector in the target centered local orbital frame.

2.2.1 Hill equations

The target centered local orbital frame is a non-inertial frame and it is rotating around the central body with an orbital rate ω. It is common to express the relative motion by linear time-varying differential equations, as shown in Fehse (2003),

$$\begin{aligned}
\ddot{x} - 2\omega\dot{z} &= f_{ux} \\
\ddot{y} + \omega^2 y &= f_{uy} \\
\ddot{z} + 2\omega\dot{x} - 3\omega^2 z &= f_{uz}
\end{aligned} \tag{2.8}$$

where ω is the orbital angular velocity that for the special case of circular orbits is considered constant and can be expressed by,

$$\omega^2 = \frac{\mu}{r_t^3} \tag{2.9}$$

and f_{ux}, f_{uy} and f_{uz} are the components of the specific force vector of control. The Equations 2.8 represent the linear dynamics of the relative motion and are known as Hill equations. The derivation of these equations starts from the linearization of the nonlinear equations and can be consulted in Fehse (2003) and in Arantes Jr. et al. (2010). An alternative solution to solve the Hill equations also for elliptical orbits has been proposed by Yamanaka and Ankersen (2002).

2.2.2 Analysis of the relative motion dynamics

A comparative analysis between the nonlinear and linear dynamics has been performed in order to evaluate the error originating from the linearization process. Yamanaka and Ankersen (2002) described that if the distance between the chaser and the target is much smaller than the distance between the target and the center of the gravity field, i.e., $|\mathbf{r}| \gg |\mathbf{s}|$, then the linear equations can be surely applied. Herein, two independent simulations have been carried out: one considering nonlinear relative dynamics equations (Equation 2.2) and the other using Hill equations to describe the linear motion (Equation 2.8). It is assumed a scenario where the chaser starts at 10 m away from the target in the direction of the R-bar axis. The complete initial condition is: $x_0, y_0 = 0$; $z_0 = 10$ m; $\dot{x}_0, \dot{y}_0, \dot{z}_0 = 0$. The target vehicle is on a circular orbit of 400 km of altitude and 30 degrees of inclination. The relative motion of both types of dynamics (linear and nonlinear) can be seen in Figure 2.3. Note that after two orbits, the chaser is approximately 750 m away from the target.

Figure 2.4 shows the error in the relative position originated from the linearization process as a function of the target's distance. Here, four target orbits has been

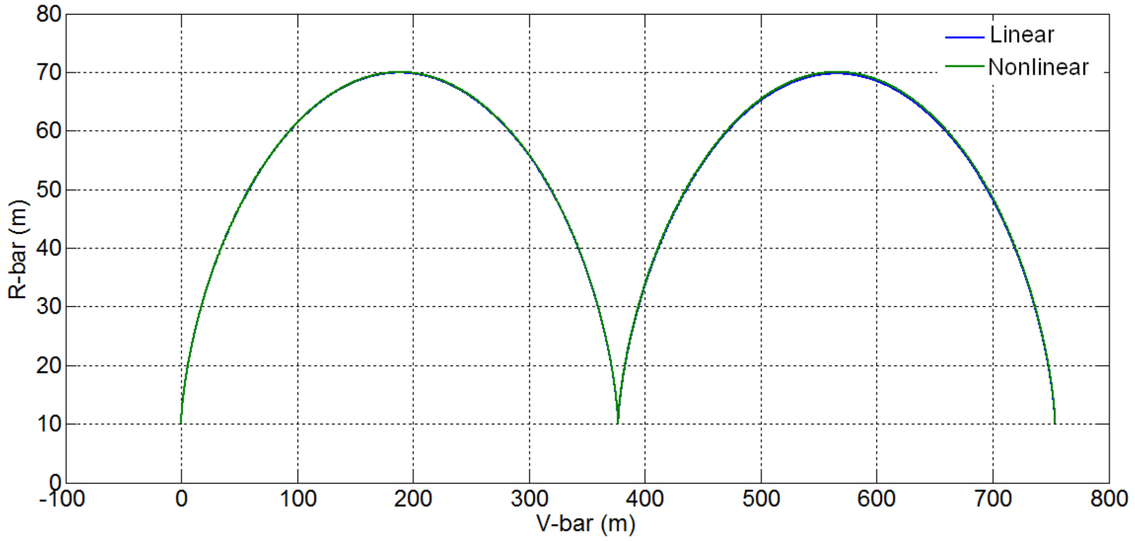

Figure 2.3 - Relative motion starting from the R-bar axis.

considered as the stopping criterion.

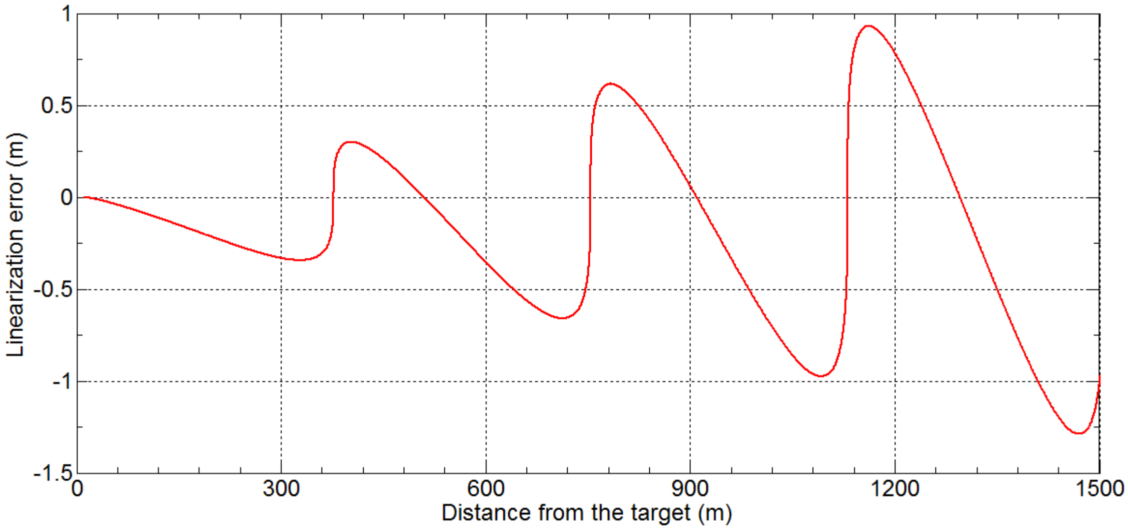

Figure 2.4 - Linearization error of the relative motion simulation.

As can be noted, Hill equations lose their accuracy insofar as the distance between the spacecraft increases; reaching an error of the order of 1 m in 1500 m from the target. However, for short distances of few tens of meters, as the case of the final approach rendezvous phase, the linearization error can be negligible. Thus, the linear dynamics expressed by Hill equations is chosen in this thesis to represent the relative motion dynamics. A complete study about both types of relative dynamics can be seen in Gomes dos Santos and Rocco (2013).

2.3 Attitude dynamics and kinematics

The rotational dynamics of a rigid body determines how the attitude parameters vary with the time for a given angular velocity. We can write the angular momentum, $\mathbf{h} \in \mathbb{R}^3$, of a rigid body as

$$\mathbf{h} = \mathbf{I}\boldsymbol{\omega} \tag{2.10}$$

where $\mathbf{I} \in \mathbb{R}^{3\times3}$ is the inertia matrix and $\boldsymbol{\omega} \in \mathbb{R}^3$ is the inertial angular velocity vector. The torque vector $\mathbf{N} \in \mathbb{R}^3$ can be expressed as

$$\frac{d\mathbf{h}}{dt} = \mathbf{N} \tag{2.11}$$

Let us suppose that a rigid body is moving in an inertial frame. This motion can be described by the translational motion of its center of mass (CoM), together with a rotational motion of the body about some axis along its CoM. In the following analysis we shall use the well-known operator equation acting on a given vector **A**,

$$\dot{\mathbf{A}}_i = \dot{\mathbf{A}}_b + \boldsymbol{\omega}_0 \times \mathbf{A}_i \tag{2.12}$$

which simply states that the rate of change of the vector **A** as observed in the fixed coordinate system (denoted by the subscript "i") equals the rate of change of the vector **A** as observed in the rotating coordinate system (denoted by the subscript "b") with angular velocity $\boldsymbol{\omega}_0$ (HIBBELER, 2010; SIDI, 1997). Applying this concept to the angular momentum vector **h**, we can write

$$\mathbf{N} = \dot{\mathbf{h}}_i = \dot{\mathbf{h}}_b + \boldsymbol{\omega}_0 \times \mathbf{h}_i \tag{2.13}$$

where $\dot{\mathbf{h}}_b$ is the time derivative of $\mathbf{h}$ measured from the body coordinate system and the term $\boldsymbol{\omega}_0 \times \mathbf{h}_i$ represents the change of $\mathbf{h}_i$ caused by the rotation of the body axes frame. If we consider the rotating frame fixed in and move with the body, then the inertia matrix is constant and $\boldsymbol{\omega}_0 = \boldsymbol{\omega}$ (HIBBELER, 2010). Using the relation of Equation 2.10, Equation 2.13 turns out

$$\mathbf{N} = \mathbf{I}\dot{\boldsymbol{\omega}} + \boldsymbol{\omega} \times \mathbf{I}\boldsymbol{\omega} \tag{2.14}$$

In the special case of the body axes being coincident along the principal axes of inertia, the inertia matrix $\mathbf{I}$ is diagonal (the inertia products are zero) and Equation 2.14 becomes (SIDI, 1997)

$$\begin{aligned} N_x &= I_x\dot{\omega}_x + (I_z - I_y)\omega_z\omega_y \\ N_y &= I_y\dot{\omega}_y + (I_x - I_z)\omega_x\omega_z \\ N_z &= I_z\dot{\omega}_z + (I_y - I_x)\omega_y\omega_x \end{aligned} \tag{2.15}$$

The Equation 2.15 represents three scalar, coupled, nonlinear, ordinary differential equations, called Euler's equations of rotational dynamics. The solution of these equations gives the angular velocity at a given instant. The attitude of a spacecraft can be represented by various alternative kinematic parameters, such as Euler angles, Euler axis and principal angle, Euler symmetric parameters (quaternion), Rodrigues parameters, and modified Rodrigues parameters (TEWARI, 2007). Quaternion and Euler angles are used to describe the attitude kinematics in this work. Here the Euler angles 3-2-1 convention is used, i.e., an orientation described by three consecutive rotations: first a rotation around the X_b axis by an angle ϕ, then a rotation around the Y_b axis by an angle θ, and finally a rotation around the resulting Z_b axis by an angle ψ. The kinematic differential equations of an orbiting rigid body represented by the Euler angles ϕ (roll), θ (pitch), and ψ (yaw), for the orientation 3-2-1 is given by (WIE, 1998; GARCIA, 2011)

$$\begin{bmatrix} \dot{\phi} \\ \dot{\theta} \\ \dot{\psi} \end{bmatrix} = \frac{1}{\cos(\theta)} \begin{bmatrix} \cos(\theta) & \sin(\phi)\sin(\theta) & \cos(\phi)\sin(\theta) \\ 0 & \cos(\phi)\cos(\theta) & -\sin(\phi)\cos(\theta) \\ 0 & \sin(\phi) & \cos(\phi) \end{bmatrix} \begin{bmatrix} \omega_x \\ \omega_y \\ \omega_z \end{bmatrix} + \boldsymbol{\omega_{ri}} \quad (2.16)$$

The angular velocity of the reference frame with respect to the inertial frame, $\boldsymbol{\omega_{ri}}$, is then give by

$$\boldsymbol{\omega_{ri}} = \frac{\omega_0}{\cos(\theta)} \begin{bmatrix} \sin(\psi) \\ \cos(\theta)\cos(\psi) \\ \sin(\theta)\sin(\psi) \end{bmatrix} \quad (2.17)$$

where ω_o represents the constant orbital rate.

Due to the singularities, Euler angles are not used to represent the attitude in numerical models, unless it is guaranteed that the attitude is far from singular points, otherwise significant numerical errors may occur. Representation by quaternions provides a more convenient parametrization than the Euler angles, because there are no trigonometric functions which require a longer processing time. A quaternion ($\mathbf{q} \in \mathbb{R}^4$) is a special set composed of four mutually dependent scalar parameters (q_1, q_2, q_3 and q_4), such that the first three form a vector, called the vector part, and the fourth represents the scalar part. The kinematic differential equation represented by quartenions is expressed by (TEWARI, 2007),

$$\dot{\mathbf{q}} = \frac{1}{2}\boldsymbol{\Omega}\mathbf{q} \quad (2.18)$$

where $\boldsymbol{\Omega} \in \mathbb{R}^{4\times4}$ is the skew-symmetric matrix of the angular velocity components,

$$\boldsymbol{\Omega} = \begin{bmatrix} 0 & \omega_z & -\omega_y + \omega_0 & \omega_x \\ -\omega_z & 0 & \omega_x & \omega_y + \omega_0 \\ \omega_y - \omega_0 & -\omega_x & 0 & \omega_z \\ -\omega_x & -\omega_y - \omega_0 & -\omega_z & 0 \end{bmatrix} \quad (2.19)$$

The kinematic equations together with Euler's equations of rotational dynamics complete the set of differential equations needed to describe the change in attitude of a rigid body under the influence of a time-varying torque. The direction cosine matrix (or rotation matrix) is very important for the transformation among the attitude representations. To simplify the notation, we shall abbreviate cos(_) to $c\_$ and sin(_) to $s\_$. With this convention, the rotation matrix for the orientation 3-2-1 in term of the Euler angles is given by (SIDI, 1997)

$$\mathbf{C}_{321} = \begin{bmatrix} c\theta c\psi & c\theta s\psi & -s\theta \\ -c\phi s\psi + s\phi s\theta c\psi & c\phi c\psi + s\phi s\theta s\psi & s\phi c\theta \\ s\phi s\psi + c\phi s\theta c\psi & -s\phi c\psi + c\phi s\theta s\psi & c\phi c\theta \end{bmatrix} \tag{2.20}$$

The direction cosine matrix can also be expressed in terms of the quaternions

$$\mathbf{C_q} = \begin{bmatrix} q_1^2 - q_2^2 - q_3^2 + q_4^2 & 2(q_1q_2 + q_3q_4) & 2(q_1q_3 - q_2q_4) \\ 2(q_1q_2 - q_3q_4) & -q_1^2 + q_2^2 - q_3^2 + q_4^2 & 2(q_2q_3 + q_1q_4) \\ 2(q_1q_3 + q_2q_4) & 2(q_2q_3 - q_1q_4) & -q_1^2 - q_2^2 + q_3^2 + q_4^2 \end{bmatrix} \tag{2.21}$$

Therefore, the following expressions can be used to calculate the quaternions elements from the elements of the rotation matrix $\mathbf{C}_{321}$ (defined in Equation 2.20)

$$\begin{aligned} q_1 &= \frac{c_{23} - c_{32}}{4q_4} \\ q_2 &= \frac{c_{31} - c_{13}}{4q_4} \\ q_3 &= \frac{c_{12} - c_{21}}{4q_4} \end{aligned} \tag{2.22}$$

where c_{ij} represents the element (i,j) of $\mathbf{C}$; and q_4 is given by

$$q_4 = \pm\frac{1}{2}\sqrt{1 + c_{11} + c_{22} + c_{33}} = \pm\frac{1}{2}\sqrt{1 + \text{ trace } C} \tag{2.23}$$

Certainly, the derivation given above is valid only if $q_4 \neq 0$. If q_4 is close to zero, then one can employ an alternative derivation, such as the following

$$\begin{aligned} q_2 &= \frac{c_{12} + c_{21}}{4q_1} \\ q_3 &= \frac{c_{31} + c_{13}}{4q_1} \\ q_4 &= \frac{c_{23} - c_{32}}{4q_1} \end{aligned} \tag{2.24}$$

where

$$q_1 = \pm\frac{1}{2}\sqrt{1 + c_{11} + c_{22} + c_{33}} \tag{2.25}$$

Similarly, the two remaining alternatives derivations of the quaternion from the rotation matrix involve division by q_2 and q_3, and can be found in Tewari (2007). Likewise, the Euler angles for the transformation 3-2-1 can be determined from the elements of the rotation matrix $\mathbf{C_q}$ (defined in Equation 2.21)

$$\begin{aligned} \phi &= \arctan(c_{23}/c_{33}) \\ \theta &= -\arcsin(c_{13}) \\ \psi &= \arctan(c_{12}/c_{11}) \end{aligned} \tag{2.26}$$

Of course, neither c_{11} nor c_{33} cannot be zero; otherwise the angles ϕ and ψ cannot be determined. In such a case, the Euler angle representation is said to be singular, and becomes useless.

2.4 Environmental disturbances in the translational and rotational motions

Residual atmospheric drag and gravity gradient moment have been considered in this work as external disturbances. The former disturbs the translational motion whereas the latter disturbs the attitude motion. Both perturbations play an important role in low Earth orbit (LEO) satellites and they are continuously counteracted by the control systems. It is assumed here that the residual atmospheric drag does not affect the attitude motion.

2.4.1 Translational disturbance: Residual atmospheric drag

The drag force generated by the residual atmosphere on a spacecraft is given by

$$F_D = -\frac{\rho}{2} V_x^2 C_D A \tag{2.27}$$

where V_x is the orbital velocity; C_D is the drag coefficient; and A is the cross section of the body. Since both vehicles are affected by drag, and as the difference of their absolute velocities is negligible, the differential drag force per unit of mass acting on the chaser with respect to the target in a circular orbit, in this case $V_x = \omega r$, is described by (FEHSE, 2003)

$$\Delta\gamma_D = -\frac{\rho}{2}\omega^2 r^2 \frac{1}{C_{Bc}}\left(1 - \frac{C_{Bc}}{C_{Bt}}\right) \tag{2.28}$$

where $C_{Bi} = \frac{m_i}{C_D A_i}$ $(i = c, t)$ is the ballistic coefficient of the vehicle; m is the mass of the target; and the subscripts c and t indicate chaser and target, respectively. This thesis follows the convention of the U.S. Standard Atmosphere (TEWARI, 2007) to compute the Earth's atmospheric density ρ. Such model takes into account the altitude of the spacecraft up to 2000 km. The properties of the atmosphere is crucial for the analysis and design of spacecraft. Over the last decades, aerodynamic forces have been studied as a new actuation technique, called aeroassisted maneuvers, to change the trajectory and velocity of a spacecraft (GOMES DOS SANTOS, 2011; GOMES DOS SANTOS et al., 2013; GOMES DOS SANTOS et al., 2014).

2.4.2 Rotational disturbance: Gravity gradient moment

One important external moment generated due to the variation of the gravity force along the vehicle dimensions, inherent in LEO satellites, is the gravitational moment. This disturbance is capable of overwhelming the attitude control system of a large spacecraft in low orbit if not properly compensate for (TEWARI, 2007). It is quite acquainted that an asymmetric body subject to a gravitational field will experience a torque tending to align the axis of least inertia with the field direction. The gravity gradient moment components are defined as follows (FONSECA et al., 1985; SIDI, 1997)

$$
\begin{aligned}
G_x &= \frac{3\mu}{2r_i^3}(I_z - I_y)\sin(2\phi)\cos^2(\theta) = \frac{3\mu}{r_i^3}(I_z - I_y)c_{23}c_{33} \\
G_y &= \frac{3\mu}{2r_i^3}(I_z - I_x)\sin(2\theta)\cos(\phi) = \frac{-3\mu}{r_i^3}(I_z - I_x)c_{13}c_{33} \\
G_z &= \frac{3\mu}{2r_i^3}(I_x - I_y)\sin(2\theta)\sin(\phi) = \frac{-3\mu}{r_i^3}(I_x - I_y)c_{13}c_{23}
\end{aligned}
\tag{2.29}
$$

where r_i $(i = c, t)$ is the distance from the Earth's center of mass to the spacecraft.

2.5 Discrete PID Controller

Several types of controllers can be used in a control system, according to their application, such as LQR, LQG, PID, PID-fuzzy, H_∞, among others. Most industrial controllers are Proportional-Integral-Derivative (PID) due to its flexibility, low cost and robustness. For applications in RvD maneuvers, PID controllers usually satisfy the requirements of the spacecraft control system (FEHSE, 2003). The objective of the control function is to calculate the force and torque commands needed to be applied to the spacecraft to correct the deviations in the state. Here a discrete PID controller has been designed in order to ensure the stability of the GNC loop, to keep low steady state errors, and to have a good noise rejection capability. The discrete control signal is given by (ÄSTRöM; WITTENMARK, 1997)

$$
u(h) = K_p e(h) + \left[I(h + \Delta h_c) - \frac{K_p \Delta h_c}{T_i} e(h) \right] S_w + K_p T_d \dot{e}(h) \tag{2.30}
$$

where $e(h)$ and $\dot{e}(h)$ are the position and velocity errors, respectively, between the desired and the estimated state; K_p is the proportional gain; T_i is the integral time constant; T_d is the derivative time constant; Δh_c is the controller sample period; $I(h + \Delta h_c)$ is the integral control signal; and the parameter S_w switches the integral action in order to avoid the integral windup effect (JOHNSON; MORADI, 2005). This phenomenon is usually created by nonlinear actuators. If the actuator output is in the saturation region then the control signal has no effect on the actuator output. The practical consequence of this behavior is the reversing of the process to open-loop control or the exhibition of excessive overshoot in the process output.

2.6 Actuators

In the literature, it is common to find works which assume the behavior of actuators as ideal, i.e., the control signal, delivered by the controller, is interpreted as force and torque. However, it is evident that actuators dynamics, as the nonlinear behavior of thrusters or of electromechanical devices, can affect the control system's performance. Considerable effort has been made to model the complex and nonlinear dynamics behavior of actuators and its impact on spacecraft control systems in order to meet the increasing requirements of space applications (KRISTIANSEN; HAGEN, 2009). The most common spacecraft actuators are thrusters, reaction wheels, and magnetic torqrods. The following subsections describe the mathematical modeling of those actuators.

2.6.1 Reaction Control System

Reaction control system (RCS) is a special configuration of thrusters which provide force and torque simultaneously. This technology is usually applied to spacecraft responsible for RvD maneuvers, e.g., the ATV designed by the European Space Agency (see Figure 2.5). The position and attitude controllers generate force and torque commands of varying amplitude along the body axes.

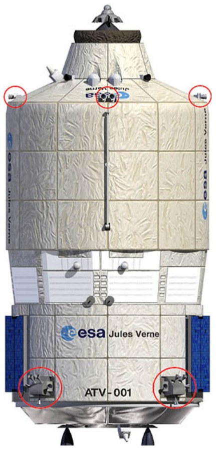

Figure 2.5 - ATV's reaction control system.
Source: Adapted from European Space Agency (2011).

Since thrusters are activated in on-off mode, the thruster management function

(TMF) has to be properly designed for the realization of such requests. In order to have a varying amplitude thruster control, thrusters are used in a quasi-linear mode by applying the pulse width pulse frequency modulation (PWPF) (SIDI, 1997). This technique modulates the pulse width and distance proportionally to the level of the controller commands. The pulse length can vary from zero to the control sample interval. The lower limit of pulse duration delivered by a thruster, called minimum impulse bit (MIB), is a constraint on the achievable GNC performance. The amplitude modulation of the force within the control cycle can be approximate (see Figure 2.6), as a first order, as (FEHSE, 2003)

$$F_{av} = F_n \frac{t_{pulse}}{t_{k+1} - t_k} \tag{2.31}$$

where F_{av} corresponds to the output of the controller; F_n is the thruster nominal force; and t_{pulse} is the pulse length commanded to the thruster control electronics.

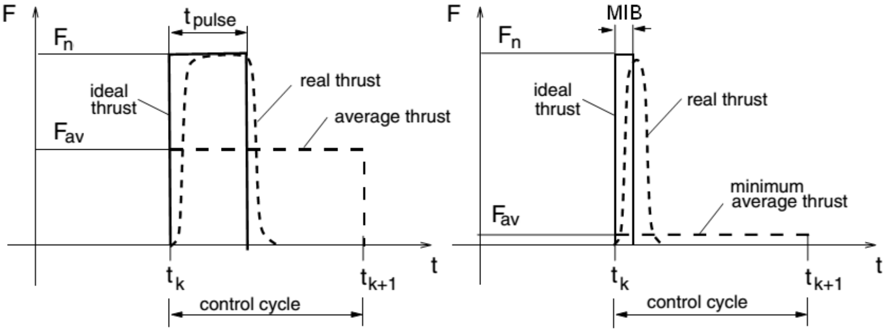

Figure 2.6 - Characteristics of the thrust pulse.
Source: Adapted from Fehse (2003).

The way how the thrusters are selected and commanded, in order to simultaneously apply force and torque, is called thruster coupling problem. There are two main approaches to manage the thrusters: fixed and flexible. The former case assumes a fixed allocation of thrusters such that all possible thruster combinations are stored in a catalog and associated with force and torque commands. This approach is rather fast and requires low computational effort. However, the fixed case is valid only for a specific thruster accommodation with a fixed CoM. In addition, the method provides suboptimal solutions with respect to propellant consumption and performance of the control system (LEY et al., 2009). An alternative to this problem is the flexible case.

With this approach, the optimal set of thrusters and the firing command duration are defined on-board by a real-time algorithm instead of being defined a priori as in the fixed case. The flexible approach, proposed earlier by Crawford (1969), involves the solution of a linear programming (LP) problem based on the simplex method (PRESS et al., 2007). The main drawback of this approach is the high computational load when numerous thrusters are used simultaneously.

In this thesis, the thruster coupling problem is treated using a flexible approach. The selection of the specific thrusters and their firing duration which realize the controller commands involve the solution of a linear optimization problem, expressed as follows (FEHSE, 2003)

$$\mathbf{F} = \mathbf{A}\mathbf{x} \tag{2.32}$$

where $\mathbf{F} = [F_1, F_2, F_3, T_4, T_5, T_6]^T \in \mathbb{R}^6$ is the requested control vector composed of three components of force and torque, respectively; since n is the number of thrusters, then $\mathbf{A} = [A_1, A_2, \cdots, A_n] \in \mathbb{R}^{6\times n}$ is the configuration matrix where its columns $A_i = [f_{ix}, f_{iy}, f_{iz}, t_{ix}, t_{iy}, t_{iz}]^T$ $(i = 1,\ 2,\ ...,\ n)$ define the force and torque components of the thrusters based on their positions and orientations in the body coordinate frame; and $\mathbf{x} = [x_1 \cdots x_n]^T \in \mathbb{R}^n$ is a normalized vector which represents the firing duration commands. The vector $\mathbf{x}$ is subject to the linear constraint of $0 \leq \mathbf{x} \leq 1$ which means that all thrusters are unidirectional.

As defined in Sidi (1997), the components of the thrust vector of a single thruster, $\mathbf{F}_s \in \mathbb{R}^3$, along the body axes are given by

$$\begin{aligned} F_{sx} &= F_n \cos(\alpha)\cos(\beta) \\ F_{sy} &= F_n \sin(\alpha) \\ F_{sz} &= F_n \cos(\alpha)\sin(\beta) \end{aligned} \tag{2.33}$$

where α and β are the elevation and azimuth angles, respectively, which define the direction of the thrust. Both angles are fixed and they represent design characteristics of the spacecraft. Therefore, the torque components of a single thruster, $\mathbf{T}_s \in \mathbb{R}^3$, about the CoM of the spacecraft can be expressed as

$$\mathbf{T}_s = \mathbf{r}_b \times \mathbf{F}_s = \begin{bmatrix} r_{by}\sin(\beta)\cos(\alpha) - r_{bz}\sin(\alpha) \\ r_{bz}\cos(\alpha)\cos(\beta) - r_{bx}\cos(\alpha)\sin(\beta) \\ r_{bx}\sin(\alpha) - r_{by}\cos(\alpha)\cos(\beta) \end{bmatrix} F_n \tag{2.34}$$

where $\mathbf{r}_b \in \mathbb{R}^3$ is the distance vector of the thruster from the CoM in the body axes frame. Both Equations 2.33 and 2.34 are useful for defining the configuration matrix $\mathbf{A}$.

According to Equation 2.32, when A is a non-singular square matrix ($n = 6$) the problem has a straightforward and single solution. However, the RCS usually has a number of thrusters n greater than the number of degrees of freedom ($n \gg 6$). Therefore, depending also on the position and orientation of the thruster there may be an infinite number of combinations of $\mathbf{x}$ which fulfill the desired force and torque vector $\mathbf{F}$. In this work, a standard linear optimization program computes all basic feasible solutions, if any, to the system of constraints. The operational constraints of the TMF are summarized below:

Remark 1. When the magnitude of the commanded outputs cannot be accomplished, then the vector $\mathbf{x}$ is computed in order to achieve at least the requested directions.

Remark 2. The force and torque commands, requested by the controller, can be satisfied through a combination of 6 thrusters per selection (ANKERSEN et al., 2005; MARTEL, 2004; PENA et al., 2000). Thus, the real-time algorithm evaluates all possible combinations of the configuration matrix but using just a maximum of 6 from a total of n thrusters, per control cycle, in order to keep a low computational effort.

Remark 3. For achievable controller commands, all feasible solutions from Equation 2.32 satisfy exactly the linear equation system if high-precision numbers are used. Nevertheless, significant errors can be introduced due to the rounding quantization process which depends on the actuator's sample frequency.

In addition to the rounding and quantization errors, random errors, bias, and delays can also be considered in the modeling. A deeper investigation about the thruster coupling problem is addressed in Chapter 5 where a new solution is proposed. Figure 2.7 shows the functional concept of the real-time TMF.

An important parameter that plays a great role in the design of RCS is the type of propulsion system. The basic equation of propellant mass consumption $m_p(t)$ is

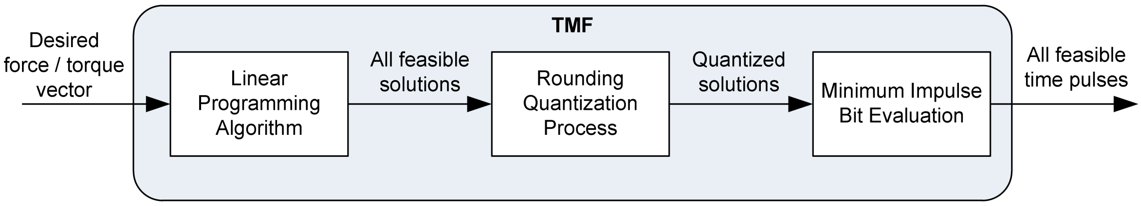
TMF
Desired force / torque vector
Linear Programming Algorithm
All feasible solutions
Rounding Quantization Process
Quantized solutions
Minimum Impulse Bit Evaluation
All feasible time pulses

Figure 2.7 - Functional concept of the thruster management function (TMF).

defined as (SUTTON; BIBLARZ, 2001)

$$m_p(t) = \int_{t_0}^{t} \frac{F_s(\tau)}{I_{sp}\mu} d\tau \tag{2.35}$$

where F_s is the applied thrust; and I_{sp} is the specific impulse of the propellant. When very short pulses (near the MIB) are activated, the specific impulse is significantly reduced, increasing the propellant consumption consequently (SIDI, 1997).

2.6.2 Reaction Wheels

Reaction wheels, illustrated in Figure 2.8, are able to provide very accurate response for reasonably fast maneuvers through the principle of conservation of angular momentum. The reaction torque is realized from the response of a flywheel whose rate of velocity change is proportional to its output. An electric motor drives the flywheel rotation implying in a variable adjustment of torque. The error between the commanded and the applied torque is mainly caused by nonlinear friction disturbances inherent to the nonlinear physical characteristics of the electric motor (GE; CHENG, 2006). It is worth mentioning that such disturbances are also responsible for increasing the electric charge consumption.

Figure 2.8 - An illustrative example of a reaction wheel.
Source: L-3 Communications Space & Navigation (2014).

The dynamic model of a electromechanical motor is used to represent the reaction wheel (SIDI, 1997), as shown in Figure 2.9. Furthermore, it is assumed a physical set-up of three identical reaction wheels whose axes of rotation are aligned with the body axes frame.

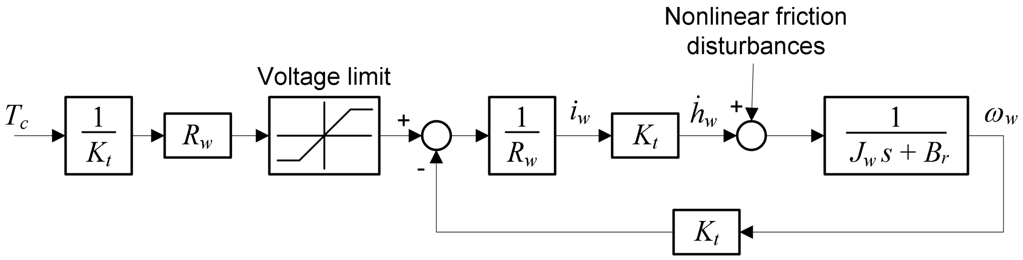

Figure 2.9 - Electromechanical model of a reaction wheel.
Source: Adapted from Sidi (1997).

In Figure 2.9, T_c is the torque command of the controller; K_t is the flywheel torque coefficient; R_w is the electrical resistance of the motor armature; i_w is the motor current; $\dot{h}_w$ is the achieved inertial torque; ω_w is the flywheel angular velocity; J_w is the flywheel moment of inertia; and B_r is the viscous damping coefficient of the rotor.

2.6.3 Magnetic Torqrods

Torqrods (also known as torque rods, torque bars, magnetotorques or magnetic coils), illustrated in Figure 2.10, are widely used in the attitude control of spacecraft and they are reliable and cost efficient devices, specially for LEO satellites. They can be used for active damping in gravity gradient attitude-stabilized spacecraft, unloading of momentum exchange devices, counteracting attitude drift due to environmental disturbance torques, or just to execute an attitude maneuver. The main advantage of torqrods is not be a consumable device (such as fuel for thrusters), thus reducing weight. However, the major disadvantage of these devices is that the applied torque is constrained in a plane perpendicular to the Earth's magnetic field vector and depends on the strength of it as well (LEY et al., 2009).

The control torque is generated through the interaction between the on-board electromagnetic dipole moment and the geomagnetic field. Such dipole moment is induced by a set of three orthogonal current-driven coils. In particular, it turns out that it is not possible to control all three spacecraft axes using only magnetic ac-

Figure 2.10 - An illustrative example of magnetic torqrods.
Source: Space Research on Unique Technology (2014).

tuators. Hence, at least, one reaction wheel is usually used in cooperation with magnetic torqrods. Nevertheless, the variability of the geomagnetic field along the spacecraft orbit plays an important role for the behavior of such actuators ensuring the controllability of the attitude dynamics. The most accepted model for Earth's magnetic field is the International Geomagnetic Reference Field (IGRF) developed by the International Association of Geomagnetism and Aeronomy. The IGRF is a set of Gaussian coefficients that is revised, typically every five years, to remain up to date and as accurate as possible. The 11th-generation IGRF (FINLAY et al., 2010) presents coefficients until degree 13 and has been used in this work. The complete theory about the geomagnetic field, and its computation in several coordinate systems, can be seen in Wertz (1978).

The magnetic control policy is based on the principle of perpendicularity (SIDI, 1997; SILANI; LOVERA, 2005) which takes into account only the component of the commanded torque vector, $\mathbf{T}_c \in \mathbb{R}^3$, perpendicular to the geomagnetic field vector, $\mathbf{b} \in \mathbb{R}^3$ (see Figure 2.11). Then the magnetic control torque, $\mathbf{T}_m \in \mathbb{R}^3$, is expressed by

$$\mathbf{T}_m = \mathbf{B}\mathbf{m} = \frac{1}{|\mathbf{b}|^2}\mathbf{B}\mathbf{B}'\mathbf{T}_c \tag{2.36}$$

where $\mathbf{m} \in \mathbb{R}^3$ is the magnetic dipole moment; and the matrix $\mathbf{B} \in \mathbb{R}^{3\times3}$ is composed of the components of the Earth's magnetic field in the body reference frame, such as

$$\mathbf{B} = \begin{bmatrix} 0 & b_z & -b_y \\ -b_z & 0 & b_x \\ b_y & -b_x & 0 \end{bmatrix} \tag{2.37}$$

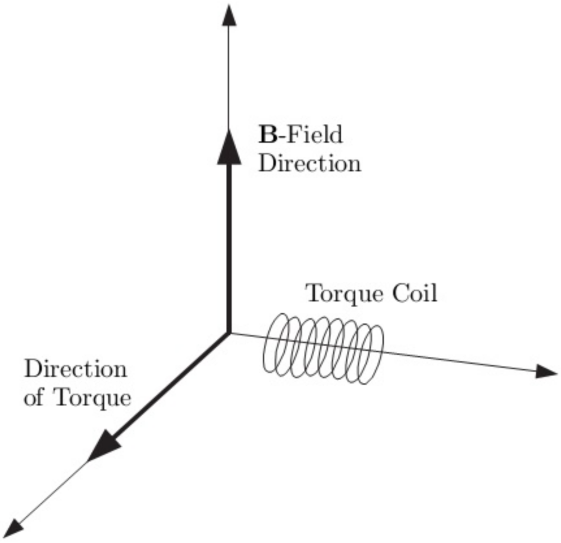

Figure 2.11 - Magnetic torque direction.

The torqrod, composed of a magnetic coil, generates a magnetic moment when energized whose equation is describe by (WERTZ, 1978)

$$\mathbf{m} = i_m N A_m \kappa \hat{\mathbf{j}} \tag{2.38}$$

where i_m is the electrical current; N is the number of coils; A_m is the cross-sectional area of the loop; κ is the permeability of the core material; and $\hat{\mathbf{j}} \in \mathbb{R}^3$ is a unit vector in the direction of the magnetic coil dipole. In general, the torqrod core can be of ferromagnetic materials or air cores.

In this work, we assume a physical set-up of three magnetic torqrods aligned with the spacecraft principal axes. As the set of actuators have already been introduced, thus we can define the Euler's dynamic equation of a satellite attitude motion composed of reaction thrusters, reaction wheels and magnetic torqrods as (SIDI, 1997)

$$\mathbf{J}_s \dot{\boldsymbol{\omega}}_s = \mathbf{T}_m + \mathbf{T}_r + \mathbf{T}_{db} - \dot{\mathbf{h}}_w - \boldsymbol{\omega}_s \times (\mathbf{J}_s \boldsymbol{\omega}_s + \mathbf{J}_w \boldsymbol{\omega}_w) \tag{2.39}$$

where $\mathbf{J}_s \in \mathbb{R}^3$ is the moment of inertia of the satellite; $\boldsymbol{\omega}_s \in \mathbb{R}^3$ is the angular velocity of the satellite body relative to the inertial coordinate frame; $\mathbf{T}_m \in \mathbb{R}^3$ is the magnetic control torque; $\mathbf{T}_r \in \mathbb{R}^3$ is the torque applied by the RCS; $\mathbf{T}_{db} \in \mathbb{R}^3$ is the external disturbance torque; $\dot{\mathbf{h}}_w \in \mathbb{R}^3$ is the inertial torque applied by the reaction wheel; $\mathbf{J}_w \in \mathbb{R}^3$ is the moment of inertia of the reaction wheel; and $\boldsymbol{\omega}_w \in \mathbb{R}^3$ is the angular velocity of the reaction wheel.

2.6.4 Basic concept of reliability

Reliability is the probability of a device performing its purpose adequately for the period of time intended under the operating conditions encountered. It means that reliability mathematically predicts the equipment's behavior under expected operating conditions. The measure of an equipment's reliability is the frequency at which failures occur in time. If there are no failures, the equipment is one hundred per cent reliable; if the failure frequency is very low, the equipment's reliability is usually still acceptable; if the failure frequency is high, the equipment is unreliable. The requirement for reliability is different for each application. In the transatlantic cable service, for instance, the underwater amplifiers must operate for 20 years or so without failure, because the cost of raising the cable to repair a failure would be very high (DUMMER; WINTON, 1968).

The true reliability is never exactly known, but numerical estimates can be obtained by the use of statistical methods and probability calculations. How close the statistically estimated reliability comes to the true reliability depends on the amount of testing, the completeness of field service reporting all successes and failures, and other essential operational data. When a device is subject only to failures which occur at random intervals, and the expected number of failures is the same for equally long operating periods, its reliability is mathematically defined by the well-acquaintance exponential equation (BAZOVSKY, 1961)

$$R(t) = e^{-\lambda t} \tag{2.40}$$

where λ is a constant called failure rate; and t is an arbitrary operating time for which we want to know the reliability of the device. The device's life period in which the above equation is valid is generally referred to as the useful life of the device. However, in certain cases it is more meaningful to use a different parameter to express the equipment's operational life. For instance, in the cases of switching devices, the number of operating cycles is a more appropriate measure of life than the number of operating hours.

The most important criterion in reliability analysis is to know how often the device break down. For that, it is used the reciprocal value of the failure rate, called mean time between failures, m_f, and given by

$$m_f = \frac{1}{\lambda} \tag{2.41}$$

It is a time parameter which completely describes the reliability of an exponentially behaving device. Therefore, the reliability function, $R(t)$, can also be written in the form

$$R(t) = e^{-t/m_f} \tag{2.42}$$

Let us now plot the curve of the failure rate against the lifetime T of a very large sample of a homogeneous component population (BAZOVSKY, 1961). The resulting failure rate graph, also called bathtub curve, is shown in Figure 2.12.

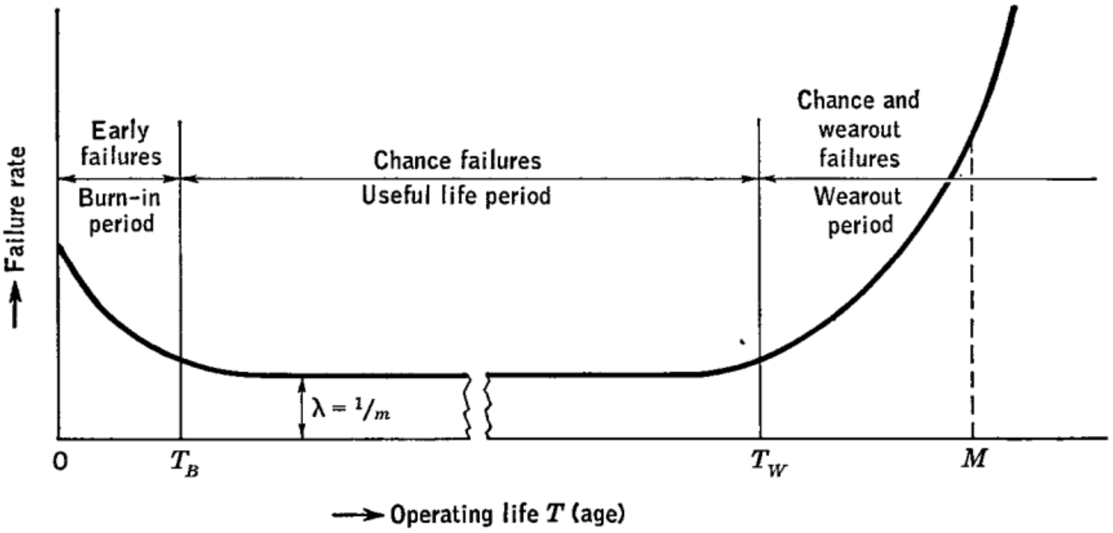

Figure 2.12 - Component failure rate as a function of age (bathtub curve).
Source: Bazovsky (1961).

At the time $T = 0$, the components will initially exhibit a high failure rate. Such failures are called early failures and in most cases result from poor manufacturing and quality-control techniques during the manufacturing process. Early failures take place usually during the first minutes or hours of operation. After this period, the failure rate decreases rapidly and stabilizes to an approximately constant value at the time T_B, when the weak components have died out. This period of life is called the useful life period, because it is in this period that the components can be used to the greatest advantage, and the exponential law has its best approximation. In this period occurs the so-called chance failures (also called catastrophic failures) which are caused by sudden stress accumulations beyond the design strength of the component. Chance failures occur at random intervals, irregularly and unexpectedly. When the components reach the life T_w, wear out begins to make itself noticeable. The failure rate increases rather rapidly from this time. The time M is the mean wear out life of the population. Wear out failures are a symptom of component aging. The part considered in this thesis is the constant failure rate period.

2.7 Navigation System

The chaser relative position and attitude are measured by a vision sensor and smoothed by a navigation filter. The extended Kalman filter (JAZWINSKI, 1970) is used to estimate the relative position. This filter is an estimator with real-time characteristics, i.e., it tries to minimize the variance of the estimation error at each sample time. The estimated chaser state is also used by the guidance function to compute the reference states. For the purely software simulations, a pinhole model [1] (BOGE et al., 2011; HARTLEY; ZISSERMAN, 2004) of the vision camera charge coupled device (CCD) sensor - whose real device belongs to the EPOS set-up - is used. The magnitude of the expected error of the relative position is pre-estimated based on a geometrical projection of the target on the camera CCD sensor, i.e., the measurements errors vary with the approach distance. The chaser's absolute attitude is provided by an accurate stellar attitude sensor with an update rate of 10 Hz. Noise and bias are assumed in both sensor models. The navigation performance of position estimation can be analyzed using the geometric relations between the camera CCD and the target (see Figure 2.13).

It turns out in the following mathematical relation

---

[1] The pinhole camera model describes the mathematical relationship between the coordinates of a 3D point and its projection onto the image plane of an ideal simple camera, where the camera aperture is described as a point and no lenses are used to focus light.

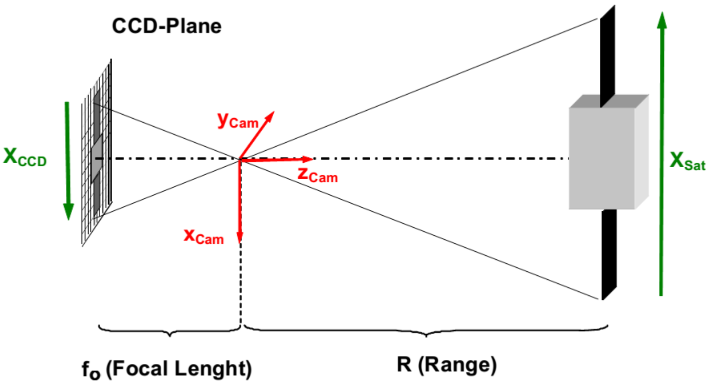

Figure 2.13 - Pinhole model of the camera CCD sensor.
Source: Adapted from Boge et al. (2011).

$$\frac{X_{CCD}}{f_o} = \frac{X_{sat}}{R} \tag{2.43}$$

Defining X_{CCD} as the required measurement parameter, then the partial derivations are

$$\begin{aligned} \frac{\partial X_{CCD}}{\partial X_{cam}} &= \frac{f_o}{R} \\ \frac{\partial X_{CCD}}{\partial Z_{cam}} &= \frac{f_o X_{sat}}{R^2} \end{aligned} \tag{2.44}$$

Therefore, according to Equations 2.44 the magnitude order of resulting lateral error (∂X_{cam}) and range error (∂Z_{cam}) can be pre-estimated as follows (BOGE et al., 2011)

$$\begin{aligned} |\partial X_{cam}| &= \frac{R}{f_o} \partial X_{CCD} \\ |\partial Z_{cam}| &= \frac{R^2}{f_o X_{sat}} \partial X_{CCD} \end{aligned} \tag{2.45}$$

Assuming one pixel error ($\partial X_{CCD} = 1$), a camera resolution of 640×480 pixels, and a satellite surface with dimensions of 1.8×2.3 m, the resulting position error can be analyzed for a range of R, as shown in Boge et al. (2011) and reproduced here in Figure 2.14.

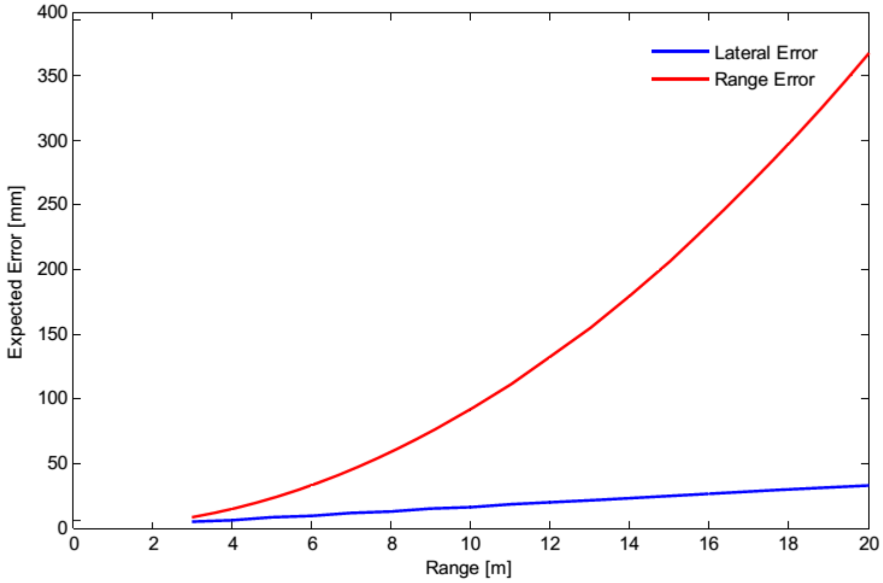

Figure 2.14 - Expected error as function of the approach range.
Source: Adapted from Boge et al. (2011).

2.8 Guidance System

The guidance function provides reference values at each sample time generating position and attitude profiles for the respective control system. Thereby, the reference values are compared with the estimated values, provided by the navigation system, in order to compute the control commands by the control system. Regarding the rendezvous guidance function, an acceleration profile has been implemented in order to reach the desired approach velocity. The rendezvous guidance profile consists of an acceleration phase, a constant velocity phase, and a deceleration phase (FEHSE, 2003), as shown in Figure 2.15. This thesis considers a typical straight line approach on V-bar axis. In addition, the formulation of the guidance laws have to take into account the capacity of the propulsion system.

For the rotational motion, the attitude guidance system calculates over time the necessary rotation to keep the chaser body frame aligned with the target docking axis. It can be mathematically expressed as follows

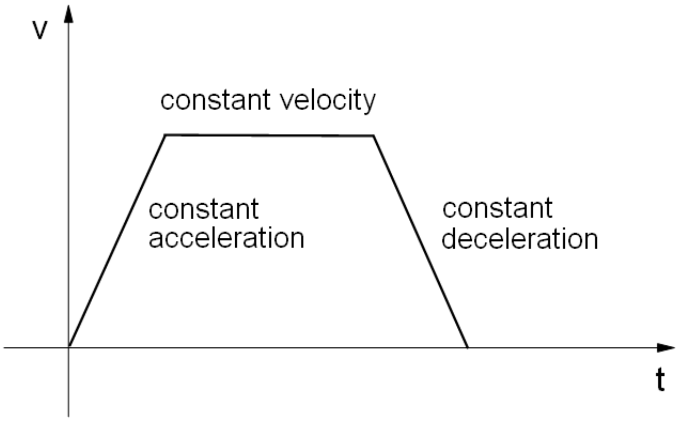

Figure 2.15 - Velocity profile used by the rendezvous guidance system.
Source: Adapted from Fehse (2003).

$$\begin{aligned}\hat{\mathbf{x}}_g &= \hat{\mathbf{d}}_r \\ \hat{\mathbf{y}}_g &= -\hat{\mathbf{h}}_o \\ \hat{\mathbf{z}}_g &= \hat{\mathbf{x}}_g \times \hat{\mathbf{y}}_g\end{aligned} \tag{2.46}$$

where $\hat{\mathbf{x}}_g, \hat{\mathbf{y}}_g, \hat{\mathbf{z}}_g$ are the unit vectors of the attitude guidance subsystem; and $\hat{\mathbf{d}}_r$ is the unit vector of the relative distance in the target centered local orbital frame.

2.9 Multiobjective Optimization

Multiobjective optimization is the process of systematically and simultaneously optimizing a group of conflicting objective functions. The problem analysis involving multiobjectives concepts started mainly in the areas of economics, sociology, psychology and operations research. Nowadays, its application to real-world problems in several fields has received much more attention. For instance, in the field of space missions, two common important objectives are the time of flight of the spacecraft to reach its destiny, and the cost of the fuel consumption (generally measured by the change in velocity). As these objectives are typically contradicting, the cheapest trajectory is certainly not the fastest one and vice versa. Several methods have been developed to find a solution that satisfy all objectives in the best way (COLLETTE; SIARRY, 2003).

The objective function (also called cost function or optimization criterion) is the name of a function which the optimization algorithm tries to optimizes, that is, to find a minimum or maximum value. Likewise, decision variables are values gathered together in the vector $\mathbf{x}$. It is by modifying this vector that is performed the search for an optimum of the objective function. A general multiobjective optimization problem can be defined, in mathematical terms, as follows (COHON, 2003)

$$\begin{aligned} &\min\ \mathbf{Z}(\mathbf{x}) \\ &\mathbf{x} \in F_d \end{aligned} \tag{2.47}$$

where the vector $\mathbf{Z}$ consists of the objective functions $Z_i : F_d \rightarrow \mathbb{R}$ under consideration, that is

$$\mathbf{Z}(\mathbf{x}) = [Z_1(\mathbf{x}), Z_2(\mathbf{x}), ..., Z_p(\mathbf{x})]^T \tag{2.48}$$

where $\mathbf{x} \in \mathbb{R}^n$ is a vector of n decision variables; p is the number of objective functions; and $F_d \in \mathbb{R}^k$ (for $k \geq 1$) is the feasible design space given by

$$F_d = \{\mathbf{x} \in \mathbb{R}^k | g_i(x) \geq 0, i = 1, 2, ..., m; \mathbf{x} \geq 0\} \tag{2.49}$$

We can discern two major types of optimization problems: discrete problems and continuous-variable problems. This thesis is concerned with the discrete case. The difference among them is that the former, also called by multiobjective combinatorial optimization (EHRGOTT; GANDIBLEUX, 2003), is characterized by a predefined set of alternatives available for the decision variables. By its nature, discrete multiobjective optimization deals with non-continuous problems, although the objectives functions are, not always but usually, linear functions. Some examples of application of this field are flow problems, shortest path, knapsack problems, transportation plans, among others. For instance, the famous traveling salesman problem deals with the minimization of the length of a journey made by a salesman who has to visit a fixed number of towns before coming back to the starting town.

A multitude of solutions is found when the multiobjective optimization problem is solved. However, only a small subset of these solutions will be of interest. For a solution to be interesting, there must exists a domination relation between the solution considered and the other solutions. In this sense, we say that a vector $\mathbf{x}_1$ dominates a vector $\mathbf{x}_2$ if: $\mathbf{x}_1$ is at least as good as $\mathbf{x}_2$ for all the objectives, and $\mathbf{x}_1$ is strictly better than $\mathbf{x}_2$ for at least one objective. Hence, solutions which dominate the others but do not dominate themselves - that is, a solution that cannot be improved in any of the objectives without degrading at least one of the other objectives - are called optimal solutions in the Pareto sense (or non-dominated solutions) (COLLETTE; SIARRY, 2003).

When we apply the concept of dominance, four areas can be defined. A preference level is associated with each area. These areas are represented in Figure 2.16.

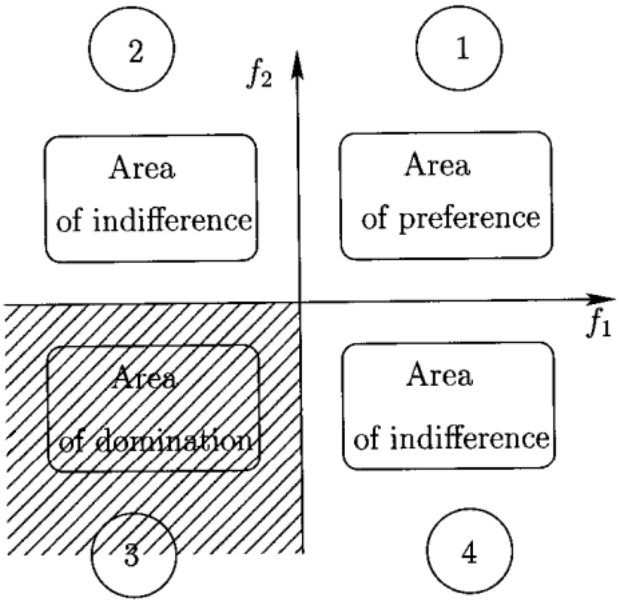

Figure 2.16 - Preference level and dominance relation.
Source: Collette and Siarry (2003).

For example, if this figure is centered on solution A and we compare this solution with solution B, then we have the following possibilities:

- if solution B belongs to area 1, then solution A is preferred to solution B;

- if solution B belongs to area 3, then solution A is dominated by solution B;

- if solution B belongs to area 2 or 4, then we cannot say if we prefer solution A in comparison to solution B or if we prefer solution B in comparison to solution A.

The set of solutions selected from the sorting rule, based on the definition of domination, produces what is called tradeoff surface (COLLETTE; SIARRY, 2003) (non-inferior set (COHON, 2003) or Pareto front (PARETO, 1992)). Those optimal values have the same degree of optimality due to the conflicting behavior between the objectives. The shape of the Pareto front depends on the type of problem we are dealing with. Some common shapes of Pareto front are shown in Figure 2.17.

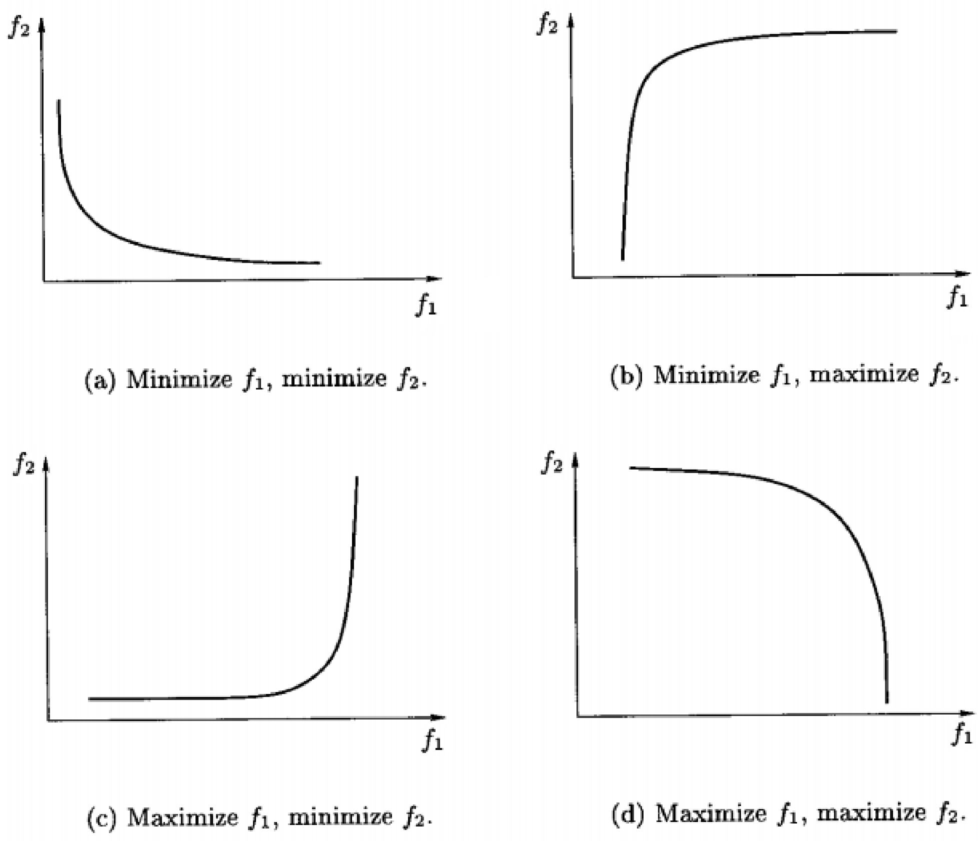
f_2
f_1
(a) Minimize f_1, minimize f_2.
f_2
f_1
(b) Minimize f_1, maximize f_2.
f_2
f_1
(c) Maximize f_1, minimize f_2.
f_2
f_1
(d) Maximize f_1, maximize f_2.

Figure 2.17 - Common shapes of Pareto front considering two objective functions.
Source: Collette and Siarry (2003).

Two characteristic points associated with the Pareto front are defined: ideal point and nadir point. The coordinate of the former point are obtained by minimizing each objective function separately. While the coordinates of the later point correspond to the worst values obtained for each objective function when the solution set is restricted to the Pareto front. The ideal point is used sometimes as a reference point whereas the nadir point is used to restrict the search space. Both points are illustrated in Figure 2.18. Unlike the single objective optimization, where the optimal objective value is unique, the solution of a multiobjective optimization problem leads to a group of optimal values with the same degree of optimality. Since is not possible to order the non-dominated solutions, then the ordinary notion of optimality should be dropped. Nevertheless, in many practical situations of engineering, a systematic method to select an alternative is necessary. In this case, a decision making method should be used.

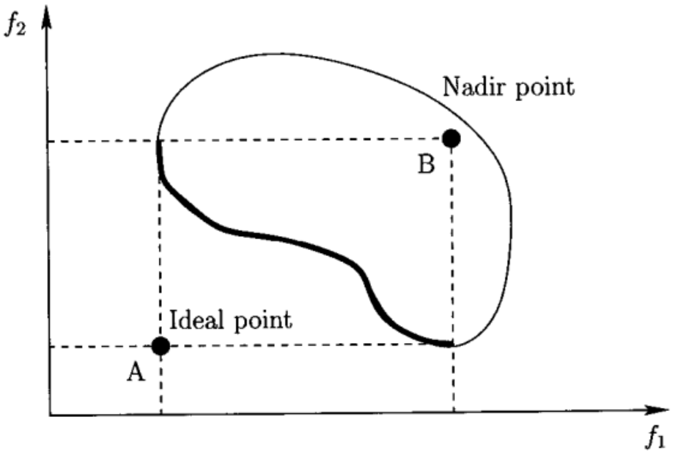

Figure 2.18 - Representation of the ideal point and the nadir point.
Source: Collette and Siarry (2003).

2.9.1 Solution methods of multiobjective optimization problems

According to Collette and Siarry (2003), the optimization methods can be classified into five categories:

- **scalar methods**: is the most common approach. The objective is to transform the multiobjective problem into a mono-objective optimization problem;

- **interactive methods**: belong to the family of progressive methods. The solution is defined during the running of the optimization method;

- **fuzzy methods**: allow to consider imprecision and uncertainty of human knowledge, as well as the progressive transitions between states;
- **methods which use a meta-heuristic**: are general optimization methods dedicated to hard optimization problem. The main meta-heuristics are simulated annealing, tabu search and genetic algorithms;
- **decision aid methods**: obtain the set of solutions based on the setting up of an order relation between the elements of a set.

The method in these five sets can be sorted into three families of multiobjective optimization methods:

- *a priori* preference methods: the decision maker defines the tradeoff to be applied before running the optimization method. In this family are most of the scalar methods;
- *progressive* preference methods: the decision maker improves the tradeoff to be applied during the running of the optimization methods. Here, we find interactive methods;
- *a posteriori* preference methods: the decision maker imposes preferences directly on solutions computed by the optimization method.

However, we could complement such classification of Collette and Siarry (2003) with a sixth category: **equilibrium methods**. Here, the solution does not depend on a decision marker's preference. A systematic methodology seeks for an equilibrium solution without prioritize any objective. In this category, we could include methods as the Smallest Loss Criterion (SLC) (ROCCO, 2002) and the Nash arbitration method (NASH JR., 1950). A compilation including many multiobjective optimization methods with emphasis on engineering is presented by Marler and Arora (2004). Some methods commonly used in the literature are the Weighted Sum method, the Constraint method, the Surrogate Worth Tradeoff method, the Multiobjective Simplex method, among others.

The goal of the optimization strategy discussed in this thesis is to use a decision making method that optimizes all objectives simultaneously and selects the best compromise solution during the running of the closed-loop simulation. Based on this assumption, an alternative decision making method has been applied: the Smallest

Loss Criterion. The Weighted Sum method has also been used, in Chapter 5, in comparison analysis with the SLC. Both methods are discussed in the following subsections.

2.9.1.1 Weighted Sum Method

This method is the most common approach to solve the multiobjective optimization problem. It combines all objectives in order to obtain an unique objective function that is formed by the average of the original objectives multiplied by a weight vector, such as (COLLETTE; SIARRY, 2003; MARLER; ARORA, 2004)

$$Z_{mean}(\mathbf{x}) = \sum_{i=1}^{p} w_i Z_i(\mathbf{x}) \tag{2.50}$$

Usually, the weigths, w_i, must respect the following relation: $w_i \geqslant 0$ for all $i \in 1, ..., p$ and

$$\sum_{i=1}^{p} w_i = 1 \tag{2.51}$$

Therefore, the problem can be treated as a single optimization problem and then the multiobjective formulation does not need to be applied. The utilization of weights rules out the necessity of a more complex algorithm of optimization, but it introduces new parameters to be found and optimized. Hence, the solution depends on the correct determination of these factors. Therefore, this determination, in an iterative process, becomes an optimization process by itself. A graphical representation of such method can be obtained for a problem with two objective functions. The problem is stated as follows

$$\begin{aligned} &\text{min} \;\; Z_1(\mathbf{x}) \\ &\text{min} \;\; Z_2(\mathbf{x}) \\ &\text{with} \;\; \mathbf{g}(\mathbf{x}) \leqslant 0 \\ &\text{and} \;\; \mathbf{h}(\mathbf{x}) = 0 \end{aligned} \tag{2.52}$$

where $\mathbf{x} \in \mathbb{R}^n$ is the decision variables; $\mathbf{g}(\mathbf{x}) \in \mathbb{R}^m$ and $\mathbf{h}(\mathbf{x}) \in \mathbb{R}^j$ represent m inequality constraints and j equality constraints, respectively. This set of constraints delimits a restricted subspace to be searched for the optimal solution. So the new objective function has the following analytical form

$$Z_{mean}(\mathbf{x}) = w_1 Z_1(\mathbf{x}) + w_2 Z_2(\mathbf{x}) \tag{2.53}$$

This is the analytical expression for a line in the Z_1, Z_2 plane. Indeed, if we try to minimize $Z_{mean}(\mathbf{x})$, in fact we look for a constant C of the following line equation, which must be as small as possible

$$Z_2(\mathbf{x}) = -\frac{w_1}{w_2} Z_1(\mathbf{x}) + C \tag{2.54}$$

In Figure 2.19, the set S corresponds to the set of values of the pair (Z_1, Z_2) which respect the constraints defined by $\mathbf{g}(\mathbf{x})$ and $\mathbf{h}(\mathbf{x})$. Lines L_1 and L_2 correspond to two distinct pairs of weights (w_1, w_2). This method consists of making lines L_1 and L_2 tangential to the set S. The solution sought corresponds to the tangent point. Repeating this process for several weight values, the solution will produce a Pareto front. However, this method can only be applied to sets S that are convex, otherwise it does not allow one to discover all the solutions on the Pareto front.

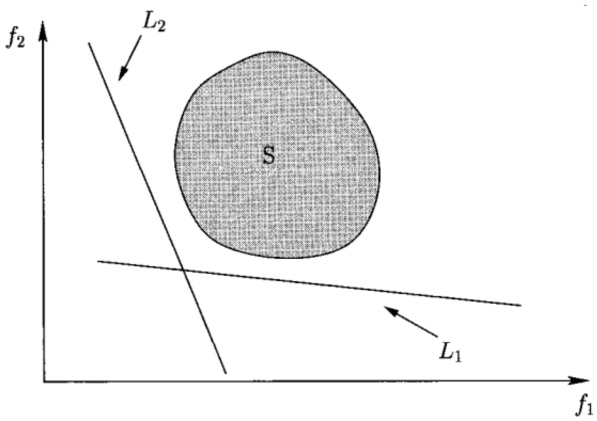

Figure 2.19 - Graphical representation of Weighted Sum Method.
Source: Collette and Siarry (2003).

2.9.1.2 Smallest Loss Criterion

As mentioned earlier, some methods prioritize a given objective and reduce the problem to a single objective problem. In real situations, it would be helpful to apply a methodology capable to find the solution that assists all the objectives simultaneously without considering the interference of a human (decision maker). Recently, an alternative to the typical decision making methods has been proposed: the Smallest Loss Criterion (SLC) (ROCCO, 2002; ROCCO et al., 2003; ROCCO et al., 2005b; ROCCO et al., 2005a; ROCCO et al., 2013). This method yields a single solution point, called best compromise solution, $\mathbf{x}^b \in \mathbb{R}^n$, without prioritize any objective.

This decision making method pursues the solution of smaller loss for all objectives, mathematically it relies on finding the barycenter [2] - which represents the equilibrium point at the objective space - of a normalized p-dimensional figure, where p represents the number of objective functions of the problem.

The barycenter solution, $\mathbf{Z}(\mathbf{x}^*) \in \mathbb{R}^p$, is computed as follows

$$\mathbf{Z}(\mathbf{x}^*) = \frac{\sum_{i=1}^{k} \mathbf{z}_i}{k} \tag{2.55}$$

where k represents the number of candidate solutions; and $\mathbf{z} \in \mathbb{R}^p$ is the normalized objective vector. The normalization process is important to disregard the dimension of each objective. Therefore, the optimal solution of a multiobjective problem would be the central point of the normalized p-dimensional figure that has as vertexes the optimal solutions of each objective function. SLC evaluates the Euclidean distance, at the objective space, from the barycenter to all candidate values. Since the closest candidate value from the barycenter is found, then a mapping to the decision space defines the best compromise solution. The function to be minimized, $\mathbf{Z}(\mathbf{x}^b) \in \mathbb{R}^p$, is given by

$$\mathbf{Z}(\mathbf{x}^b) = \min |\mathbf{Z}(\mathbf{x}) - \mathbf{Z}(\mathbf{x}^*)| = \min \left\{ \sum_{1}^{p} [Z_i(\mathbf{x}) - Z_i(\mathbf{x}^*)]^2 \right\}^{1/2} \tag{2.56}$$

Figure 2.20 illustrates an example of the method applied to three conflicting ob-

---

[2] Barycenter (also called centroid or geometric center) is the arithmetic mean position of all points in all coordinate directions (PROTTER; MORREY JR., 1970).

jectives. In this example, $S1$, $S2$ and $S3$ are the optimal values of each one of the objectives, considered separately. B is the barycenter of the triangle formed by the segments $\overline{S1}\ \overline{S2}$, $\overline{S2}\ \overline{S3}$ and $\overline{S3}\ \overline{S1}$. So, if the barycenter B is chosen as a solution for the multiobjective problem, the segment $\overline{S1}\ \overline{B}$ represents the loss regarding to the objective, and in the same way, the segments $\overline{S2}\ \overline{B}$ and $\overline{S3}\ \overline{B}$ represent the loss concerning to objectives 2 and 3. Therefore we can conclude that if the three objectives are equally considered, the best solution is that one which coincides with the barycenter of the triangle.

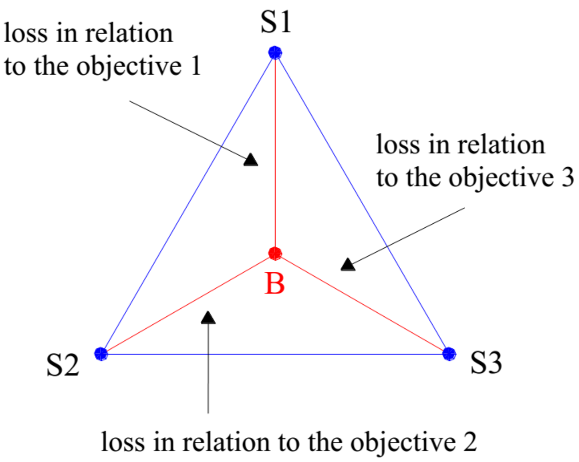

Figure 2.20 - The Smallest Loss Criterion.
Source: Rocco et al. (2003).

2.10 Spacecraft Rendezvous and Attitude Simulator

All elements of the complete GNC loop, as described earlier in Section 2.1 and depicted in Figure 2.1, have been implemented in Matlab/Simulink ® simulation environment, specially using Embedded Matlab functions. The set of models is called here Spacecraft Rendezvous and Attitude Simulator (SRAS). Besides the typical components of GNC loop, such simulator also includes the main contributions of this thesis: the AMCM-I and AMCM-II models. SRAS has been designed to operate in closed-loop controlling both translational and rotational motions at each instant of time, determined by simulation step defined as one of the input parameters for the simulator. SRAS is composed of several subsystems (Simulink blocks) which represents each element of the GNC loop. This particular software architecture allows a great flexibility for changes, improvements and replacements. This concept of software architecture has been firstly applied by Rocco (2008) to orbital transfer maneuvers. Thereafter, it has been used in optimization of low-thrust maneuvers (MARCELINO, 2009; COSTA FILHO, 2010; VENDITTI et al., 2013; OLIVEIRA et al., 2013; GONCALVES et al., 2013) and in investigations of control of aerobraking maneuvers (GOMES DOS SANTOS, 2011; GOMES DOS SANTOS et al., 2013; GOMES DOS SANTOS et al., 2014). The software architecture of SRAS is illustrated in Figure 2.21.

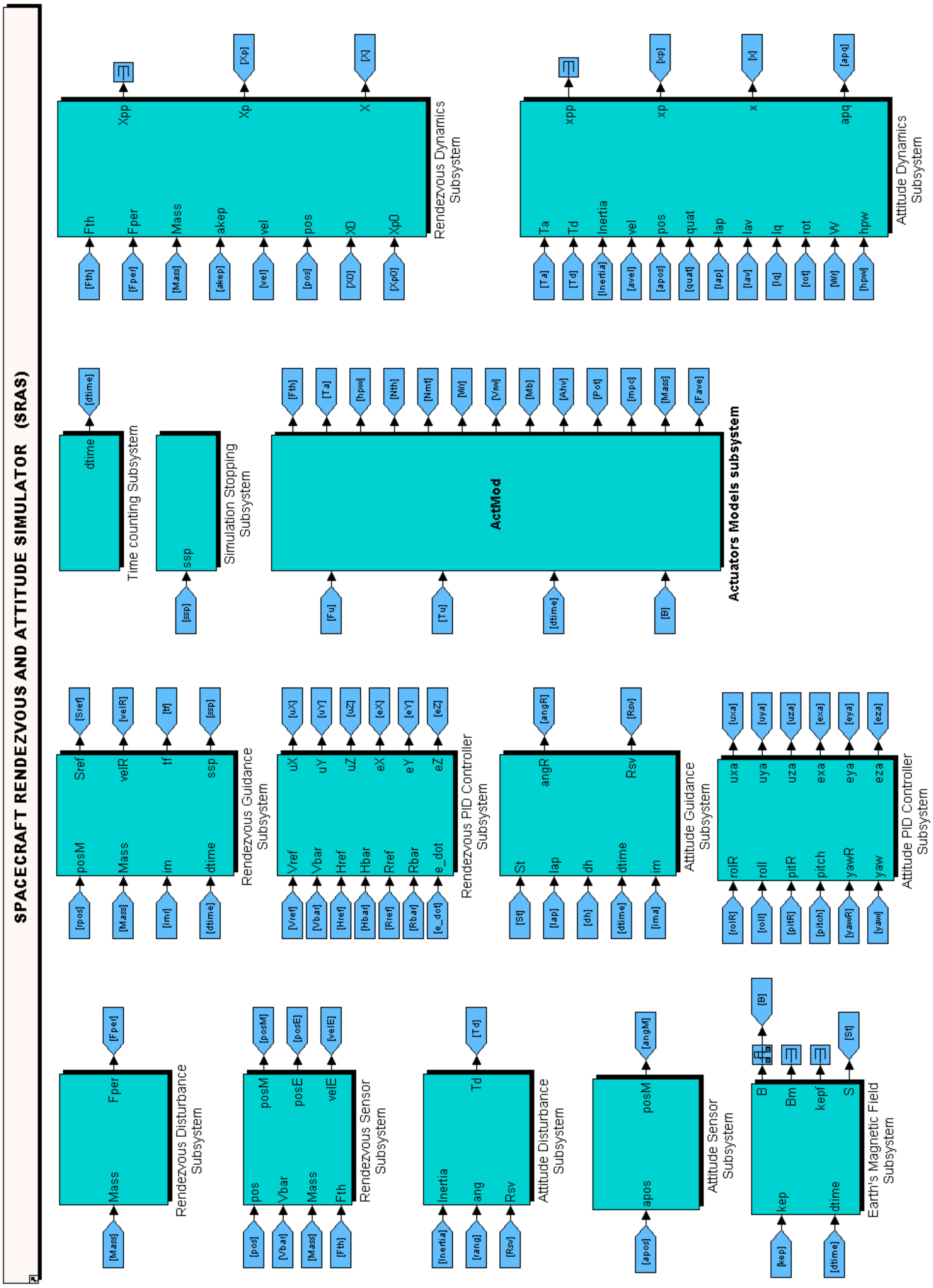
SPACECRAFT RENDEZVOUS AND ATTITUDE SIMULATOR (SRAS)
Rendezvous Dynamics Subsystem
Fth
Fper
Mass
akep
vel
pos
X0
Xp0
Xpp
Xp
X
Attitude Dynamics Subsystem
Ta
Td
Inertia
vel
pos
quat
lap
lav
lq
rot
W
hpw
xpp
xp
x
apq
Time counting Subsystem
dtime
Simulation Stopping Subsystem
ssp
ActMod
Actuators Models subsystem
[Fu]
[Tu]
[dtime]
[B]
[Fth]
[Ta]
[hpw]
[Nth]
[Nmt]
[Wr]
[Vmw]
[Mb]
[Ahv]
[Pot]
[mpo]
[Mass]
[Fave]
Rendezvous Guidance Subsystem
posM
Mass
im
dtime
Sref
velR
tf
ssp
Rendezvous PID Controller Subsystem
Vref
Vbar
Href
Hbar
Rref
Rbar
e_dot
uX
uY
uZ
eX
eY
eZ
Attitude Guidance Subsystem
St
lap
dh
dtime
im
angR
Rsv
Attitude PID Controller Subsystem
rolR
roll
pitR
pitch
yawR
yaw
uxa
uya
uza
exa
eya
eza
Rendezvous Disturbance Subsystem
Mass
Fper
Rendezvous Sensor Subsystem
pos
Vbar
Mass
Fth
posM
posE
velE
Attitude Disturbance Subsystem
Inertia
ang
Rsv
Td
Attitude Sensor Subsystem
apos
posM
Earth's Magnetic Field Subsystem
kep
dtime
B
Bm
kepf
S

Figure 2.21 - Architecture of the Spacecraft Rendezvous and Attitude Simulator.

3 DESIGN OF A LINEAR TIME-INVARIANT CONTROL SYSTEM

The contribution of this thesis begins to be presented from this chapter. Before analyzing nonlinear complex control systems, the proposed methodology is applied to a more simple case: the optimal design problem of a linear time-invariant control system composed of three different types of linear actuators. The best selection of actuators gains is defined based on a discrete multiobjective optimization approach. The transfer functions, as well as the transient response, have been derived and evaluated throughout this work. In addition, stability conditions have been analyzed for a range of closed-loop poles and zeros. The discrete multiobjective optimization problem is formulated with a couple of objective functions: overshoot and settling time of the closed-loop response. The Smallest Loss Criterion (SLC) has been used to find the best compromise solution from a group of candidate solutions. It is worth mentioning that the objective is not to specify actuators. But for a given set of three conflicting linear actuators (a fixed scenario) there shall be defined the best way to operate them.

3.1 Problem definition

Assuming a closed-loop control system composed of three linear parallel actuators, as shown in Figure 3.1, is desired to determine the gains K_n (n = 1, 2, and 3) that commands the actuators in order to satisfy the performance parameters.

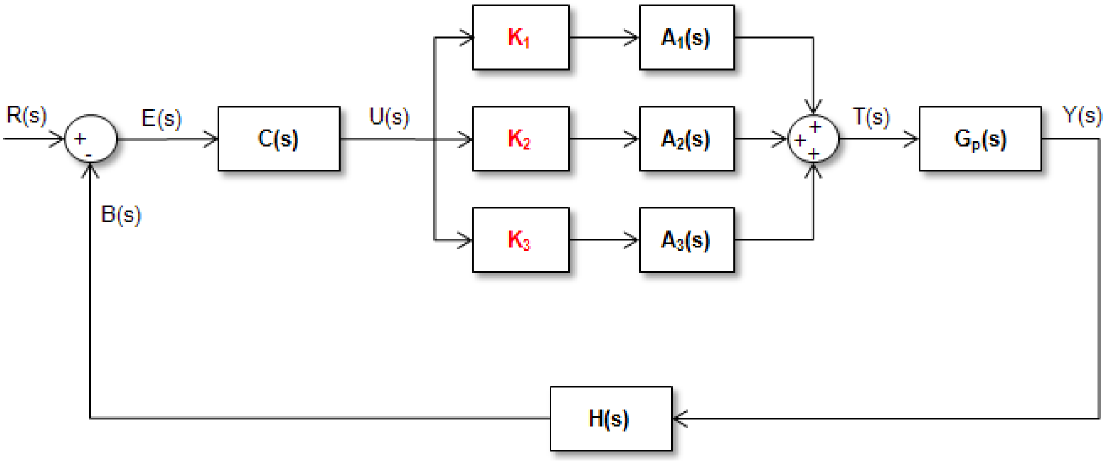

Figure 3.1 - Block diagram of the linear time-invariant control system.

The system's input and output in frequency domain are represented by $R(s)$ and $Y(s)$, respectively; $C(s)$ is the control function; $A_n(s)$ (n = 1, 2, and 3) are the actuators models; $G_p(s)$ is the process (plant) function; and $H(s)$ is the sensor function. A PID controller is used to provide the control signal, $U(s)$, whose transfer function is given by

$$C(s) = K_p \left(1 + \frac{1}{T_i s} + T_d s\right) = \left(\frac{K_d s^2 + K_p s + K_i}{s}\right) \tag{3.1}$$

The plant is modeled as a rotational dynamics and expressed as

$$G_p(s) = \frac{1}{J s^2} \tag{3.2}$$

where J is the inertia moment. Here, an ideal sensor is assumed, i.e., $H(s) = 1$. The actuators are expressed as first-order systems with different time constants, as follows

$$A_1(s) = \frac{1}{as+1} \ , \ A_2(s) = \frac{1}{bs+1} \ , \ A_3(s) = \frac{1}{cs+1} \tag{3.3}$$

The open-loop transfer function of the complete system can be described as

$$G_o(s) = \frac{Y(s)}{E(s)} = \frac{\begin{array}{l} \left(K_1 K_d bc + K_2 K_d ac + K_3 K_d ab\right) s^4 + \{K_1[K_p bc + K_d \left(b+c\right)] + ... \\ +K_2[K_p ac + K_d \left(a+c\right)] + K_3[K_p ab + K_d \left(a+b\right)]\}s^3 + ... \\ +\{K_1[K_i bc + K_p \left(b+c\right) + K_d] + K_2[K_i ac + K_p \left(a+c\right) + K_d] + ... \\ +K_3[K_i ab + K_p \left(a+b\right) + K_d]\}s^2 + \{K_1[K_i \left(b+c\right) + K_p] + ... \\ +K_2[K_i \left(a+c\right) + K_p] + K_3[K_i \left(a+b\right) + K_p]\}s + ... \\ K_1 K_i + K_2 K_i + K_3 K_i \end{array}}{J abc s^6 + J \left(ac + bc + ab\right) s^5 + J \left(a+b+c\right) s^4 + J s^3} \tag{3.4}$$

The closed-loop transfer function is determined in order to evaluate the transient response and the stability of the system, as follows below

$$G_c(s) = \frac{Y(s)}{R(s)} = \frac{G(s)}{1 + G(s)H(s)} \tag{3.5}$$

turning it out in

$$G_c(s) = \dfrac{\begin{array}{l} (K_1K_dbc + K_2K_dac + K_3K_dab)\,s^4 + \{K_1[K_pbc + K_d\,(b+c)] + ... \\ +K_2[K_pac + K_d\,(a+c)] + K_3[K_pab + K_d\,(a+b)]\}s^3 + ... \\ +\{K_1[K_ibc + K_p\,(b+c) + K_d] + K_2[K_iac + K_p\,(a+c) + K_d] + ... \\ +K_3[K_iab + K_p\,(a+b) + K_d]\}s^2 + \{K_1[K_i\,(b+c) + K_p] + ... \\ +K_2[K_i\,(a+c) + K_p] + K_3[K_i\,(a+b) + K_p]\}s + ... \\ K_1K_i + K_2K_i + K_3K_i \end{array}}{\begin{array}{l} Jabcs^6 + J\,(ac + bc + ab)\,s^5 + [(K_1K_dbc + K_2K_dac + K_3K_dab) + ... \\ +J\,(a+b+c)]s^4 + \{K_1[K_pbc + K_d\,(b+c)] + K_2[K_pac + K_d\,(a+c)] + ... \\ +K_3[K_pab + K_d\,(a+b)] + J\}s^3 + \{K_1[K_ibc + K_p\,(b+c) + K_d] + ... \\ +K_2[K_iac + K_p\,(a+c) + K_d] + K_3[K_iab + K_p\,(a+b) + K_d]\}s^2 + ... \\ \{K_1[K_i\,(b+c) + K_p] + K_2[K_i\,(a+c) + K_p] + K_3[K_i\,(a+b) + K_p]\}s + ... \\ K_1K_i + K_2K_i + K_3K_i \end{array}} \tag{3.6}$$

3.2 Numerical analysis

Controller tuning is the process of selecting the controller parameters to meet given performance specifications. Here, the PID controller has been tuned firstly using the Ziegler-Nichols rules (OGATA, 2010) and afterward performing a manual fine tuning. The goal of such process is to ensure the stability of the entire control system. The Ziegler-Nichols rules carry out the tuning based on experimental step responses or based on the value of K_p that results in marginal stability when only the proportional control action is used. For the tuning of the PID controller of this case, the actuators' gains have been considered as unity gains ($K_n = 1$, for $n = 1$, 2, and 3). The assumed parameters of the linear closed-loop control system are shown in Table 3.1.

In many practical situations, the desired performance characteristics of control systems are specified in terms of time-domain quantities, called performance parameters, such as: delay time, rise time, peak time, maximum overshoot, and settling time (OGATA, 2010). The importance of each parameter depends on the application

Table 3.1 - Parameters of the linear closed-loop control system.

Parameter	Value
K_p	1
K_i	$1 \cdot 10^{-5}$
K_d	20
J	100
a	3
b	6
c	7

of the control system under analysis. In this case of study, we assumed the settling time and overshoot parameters for analyzing. Settling time is the time required for the response curve to reach and stay within a range about the final value of size specified by absolute percentage of the final value (usually 2% or 5%). Whereas the maximum overshoot is the maximum peak value of the response curve measured from unity.

The actuators' time constants have been defined in order to achieve conflicting transient response for a step input, as shown in Figure 3.2. In this plot, it is presented the step response for each actuator as a function of time. Note that the actuator 1, which has the smallest time constant, provides the smallest overshoot and the highest settling time. On the other hand, the actuator with the highest time constant (actuator 3) presents the smallest settling time but the highest overshoot. While actuator 2 presents an intermediate response. As can be seen, there is a tradeoff between overshoot and settling time according to the time constants, that is, a conflicting scenario.

Replacing the constant parameters indicated in Table 3.1 into Equation 3.6, we have

$$G_c(s) = \frac{\begin{array}{l}(840K_1 + 420K_2 + 360K_3)\, s^4 + (302K_1 + 221K_2 + 198K_3)\, s^3 + ... \\ (33K_1 + 30K_2 + 29K_3)\, s^2 + (K_1 + K_2 + K_3)\, s + ... \\ (K_1 + K_2 + K_3) \cdot 10^{-5}\end{array}}{\begin{array}{l}12600s^6 + 8100s^5 + (840K_1 + 420K_2 + 360K_3 + 1600)\, s^4 + ... \\ (302K_1 + 221K_2 + 198K_3 + 100)\, s^3 + (33K_1 + 30K_2 + 29K_3)\, s^2 + ... \\ (K_1 + K_2 + K_3)\, s + (K_1 + K_2 + K_3) \cdot 10^{-5}\end{array}} \tag{3.7}$$

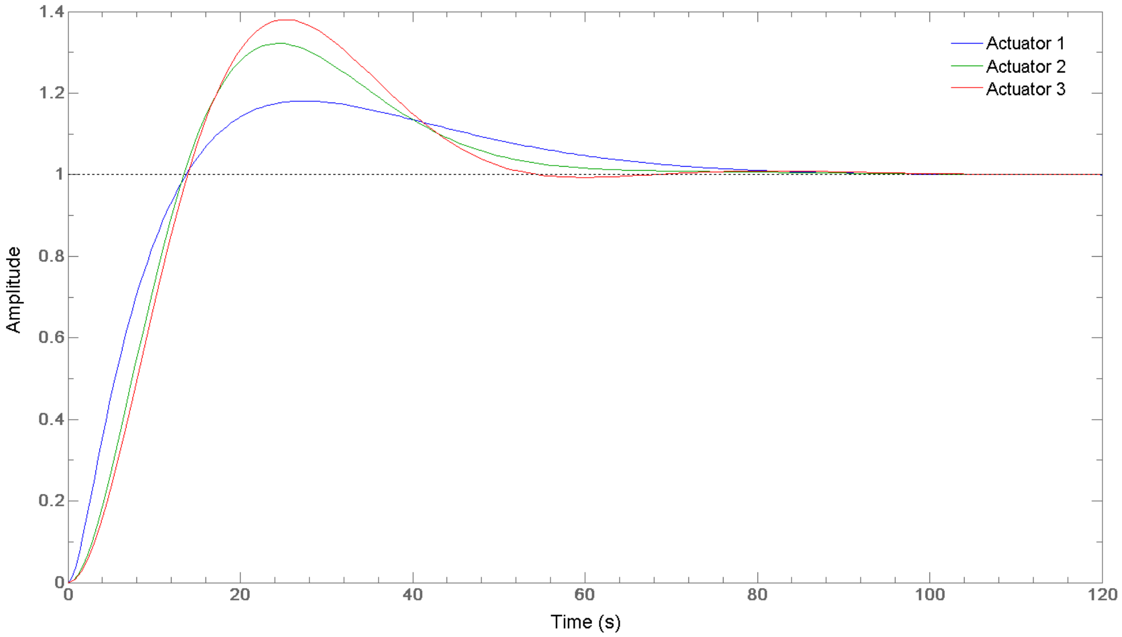

Figure 3.2 - Step response of the linear closed-loop for each actuator.

The number and location of closed-loop poles and zeros give us important information about the stability of the system and the type of the transient response. The type of transient response is determined by the closed-loop poles while the shape of the transient response is primarily determined by the closed-loop zeros (OGATA, 2010). A stable system must have all its closed-loop poles in the left-half s-plane. In addition, a slight change in the pole-zero configuration may cause significant changes in the performance of the system. Hence, it is important to know the behavior of the closed-loop poles and zeros insofar as the actuators' gains (K_1, K_2 and K_3) change. This analysis is shown in Figure 3.3 for the closed-loop poles and in Figure 3.4 for the closed-loop zeros. In both cases, the actuators' gains are evaluated in a range from 0 to 1 with a step of 0.1. The circle grid lines represent the natural frequency (ω_n) range whereas the straight grid lines represent the damping coefficients (ζ).

Note that all closed-loop poles lie on the left-half s-plane, i.e., no matter which set of gains is used, the system is stable. However, the system has some poles lying on the imaginary axis of the s-plane. It means that they have non-decaying oscillatory components in its homogeneous response, and are defined to be marginally stable. Another point to be observed in Figure 3.3 is that there are many poles close to the imaginary axis and some poles far away from the imaginary axis. As defined in many textbooks of control theory (OGATA, 2010; TEWARI, 2002), a control system's response is largely dictated by those poles that are the closest to the imaginary axis,

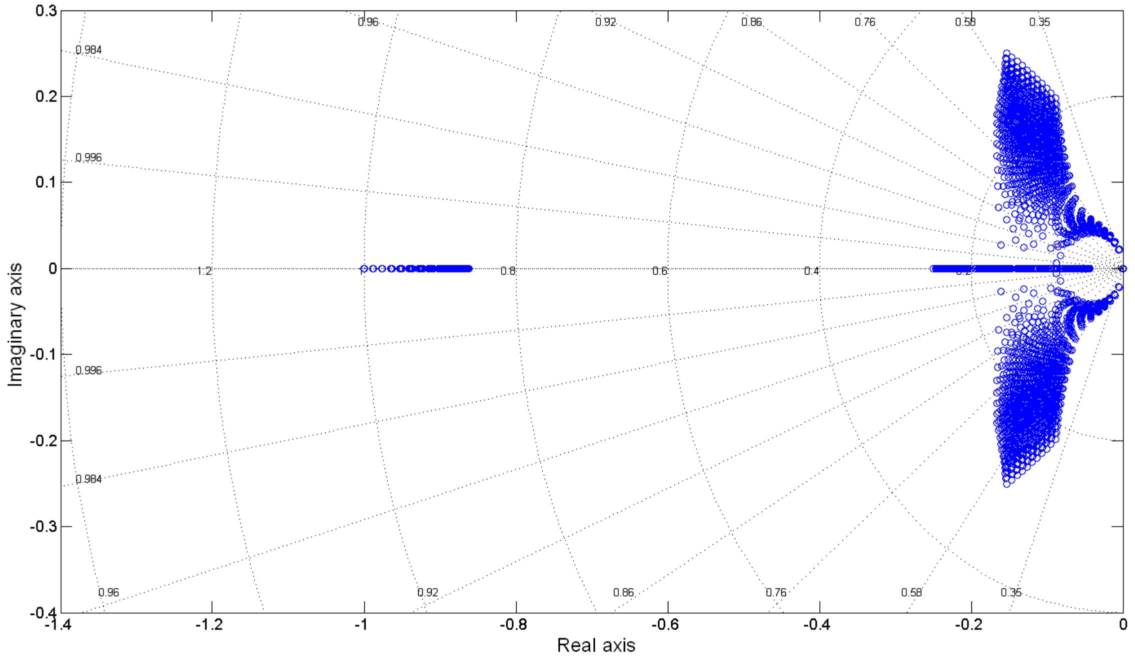

Figure 3.3 - Closed-loop poles for a range of actuators' gains in the complex plane.

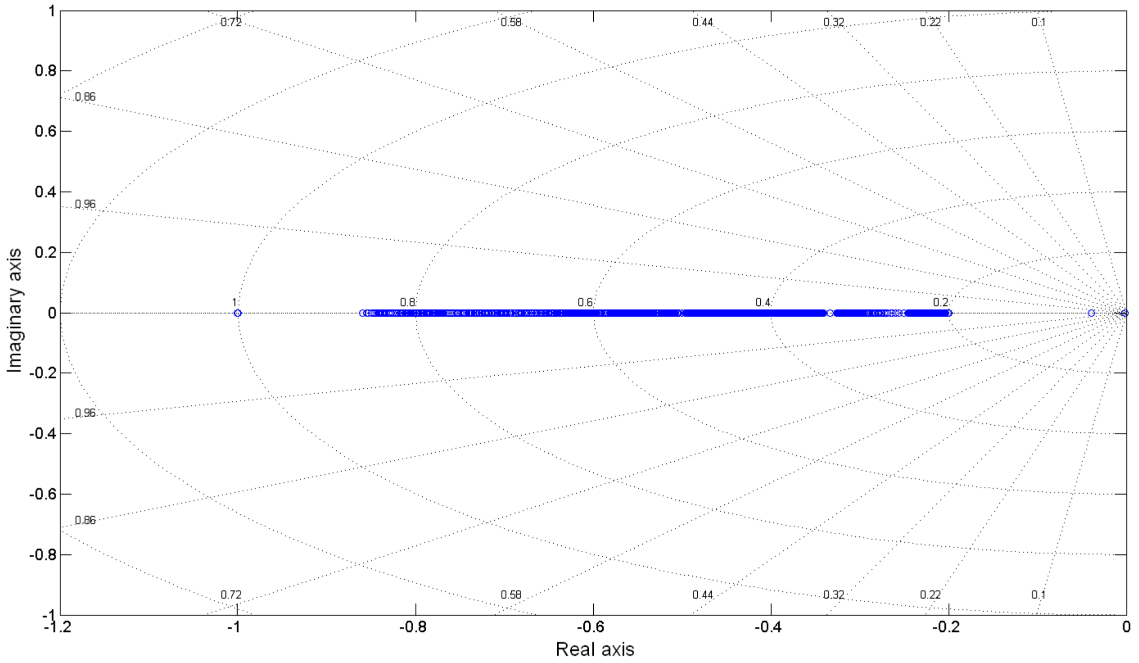

Figure 3.4 - Closed-loop zeros for a range of actuators' gains in the complex plane.

i.e. the poles that have the smallest real part magnitudes. Such poles that dominate the control system's performance are called the dominant poles.

In addition, the dynamic behavior of the control system can be described in terms of both parameters ω_n and ζ. If $0 < \zeta < 1$, the closed-loop poles are complex conjugates and lie in the left-half s-plane. The system is then called under-damped, and the transient response is oscillatory. If $\zeta = 1$, the system is called critically damped. Over-damped systems correspond to $\zeta > 1$. The transient response of critically damped and over-damped systems do not oscillate. But if $\zeta = 0$, the transient response does not die out.

Therefore, we can see in Figure 3.3 that several system performances can be achieved according to the set of gains used. Changing the actuators' gains, the transient response can vary from an oscillatory to a damped response. In other words, we can say that different values of overshoot and settling time, the main performance parameters, can be achieved as the gains change.

3.3 Discrete multiobjective optimization approach

In this case, we have a couple of objectives (overshoot and settling time) to be simultaneously minimized and three decision variables (K_1, K_2, and K_3). Moreover, a finite set of candidate solutions defines the discrete optimization problem. Plotting the objective space of this problem, we can visualize the tradeoff between the objectives. Figure 3.5 shows the settling time versus the overshoot where each point represents a combination of three gains. The blue points represent the non-dominated solutions (which compose the Pareto front) whereas the red points are the dominated solutions.

For choosing a solution, a decision making method should be used. Applying the SLC, as defined in Chapter 2, the best compromise solution can be computed. Two types of approaches have been used by the SLC: the former considers all points of the objective space while the latter assumes only the points which belong to the Pareto front. Figure 3.6 presents the flowchart of the multiobjective optimization process of the case under analysis. Firstly, the decision space is created assuming a range of actuators' gains as described earlier. Then the objective space is generated by evaluating the settling time and overshoot provided by the closed-loop transfer function for each candidate solution. The non-dominated solutions shall be sorted out for the approach considering only the Pareto front. The next step is the identification of the maximum value of each objective. The normalization process divides all objective values by the respective maximum of each objective. Afterward, the optimal solution (minimum values) of each objective is identified and the barycenter point is computed (according to Equation 2.55). Then it is evaluated the Euclidean

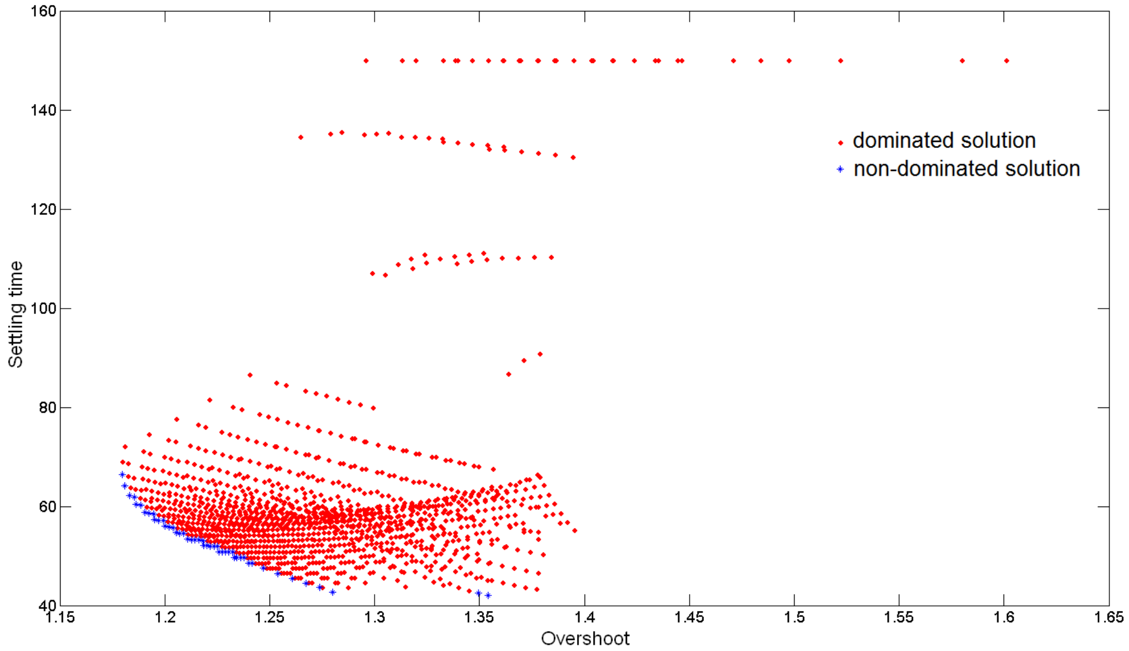

Figure 3.5 - Settling time versus overshoot: the objective space and the Pareto front.

distance from the barycenter point to all candidate solutions (according to Equation 2.56). Finally, the closest solution to the barycenter point is defined as the best compromise solution.

Table 3.2 exhibits the decision values as well the objective values for both approaches. In addition, the proposed methods have been compared with the extreme cases where only one actuator is used. We can note that the approach using only non-dominated solutions was a little bit better (an average reduction of 3%) than the approach using all points of the objective space. In addition, we can see that the solutions found by the SLC are solutions which seek an equilibrium among the objective functions. Table 3.2 also quantify the performance parameters, previously shown in Figure 3.2, of each actuator option. Using the gains defined by the SLC which represent the best compromise solutions, then the step time response can be visualized in Figure 3.7.

Nevertheless, it is not trivial to analyze the efficiency of a multiobjective problem due to the conflicting behavior among the objectives. Therefore, a single performance parameter, called **performance overall mean** ($\bar{\eta}$), has been created in order to provide an additional way of comparing the results. This parameter represents the average of all normalized objective values, as follows

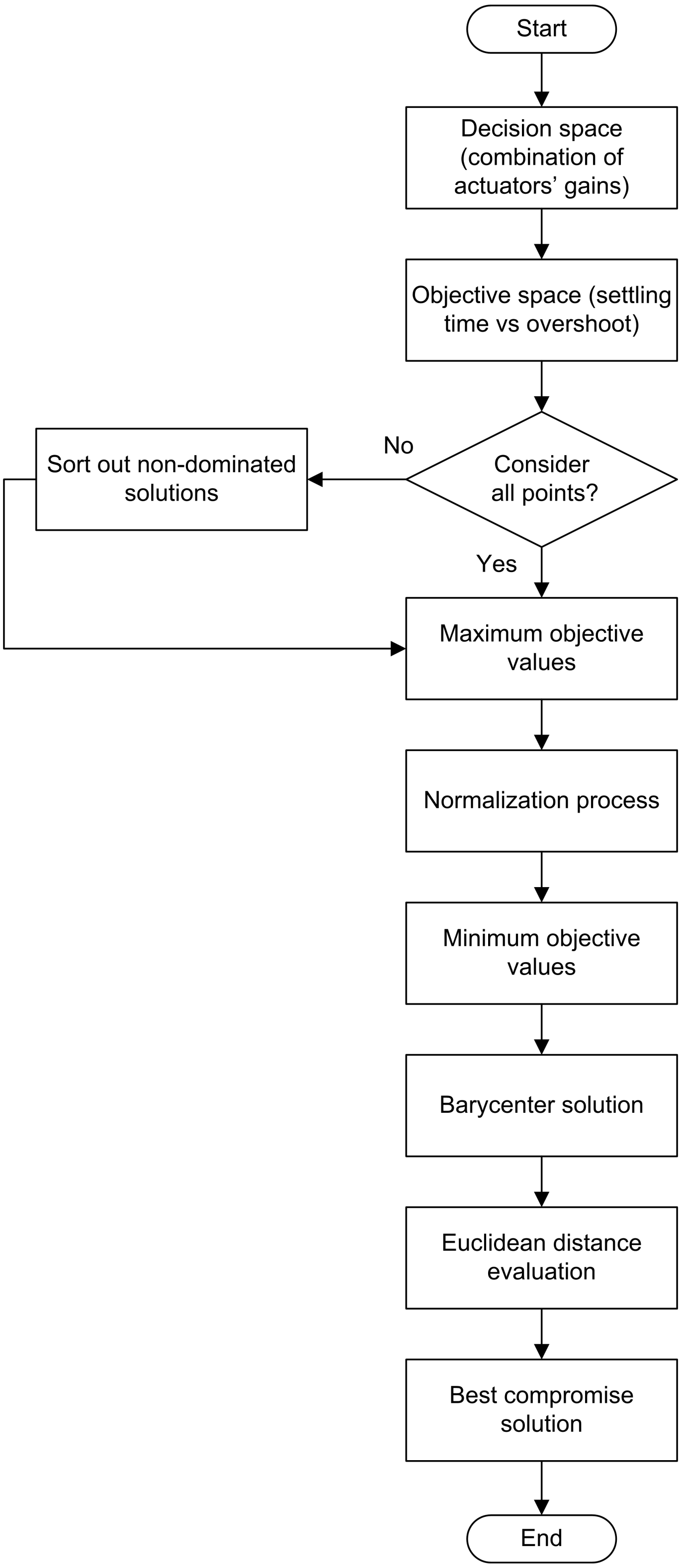
Start
Decision space (combination of actuators' gains)
Objective space (settling time vs overshoot)
Consider all points?
No
Sort out non-dominated solutions
Yes
Maximum objective values
Normalization process
Minimum objective values
Barycenter solution
Euclidean distance evaluation
Best compromise solution
End

Figure 3.6 - Flowchart of the multiobjective optimization process applied to the optimal design problem.

Table 3.2 - Best compromise solution and extreme cases of the design optimization problem.

Approach	K_1	K_2	K_3	Overshoot	Settling time
All points	0.6	0.9	0.4	1.27	54.43
Only Pareto front	1.0	0.6	0.4	1.22	53.11
Actuator 1	1	0	0	1.18	72.09
Actuator 2	0	1	0	1.32	57.74
Actuator 3	0	0	1	1.38	50.25

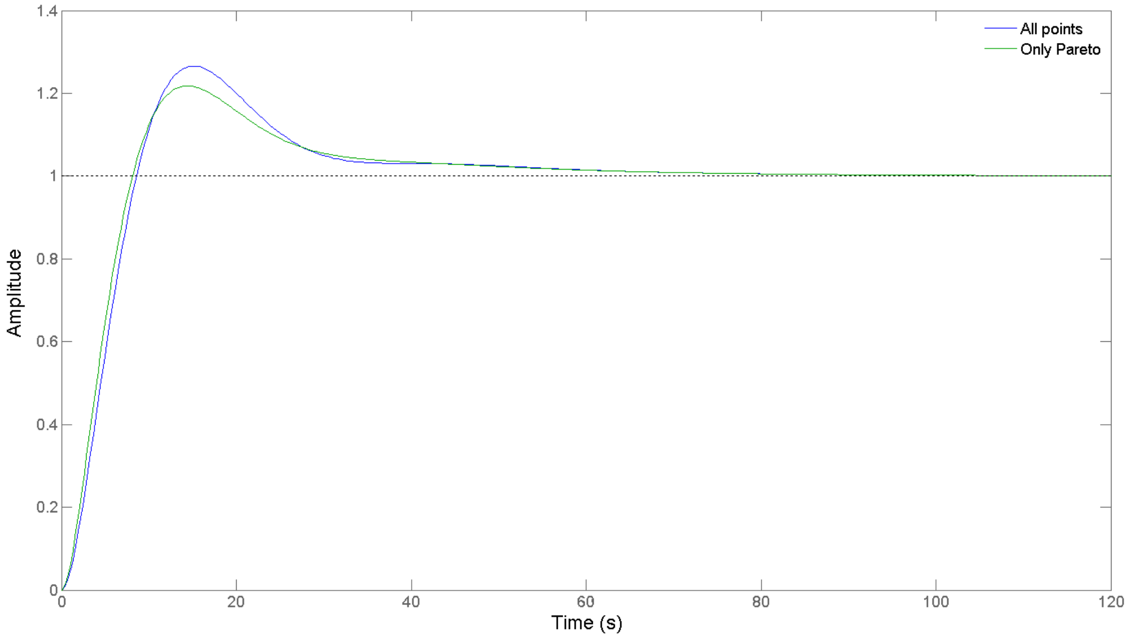

Figure 3.7 - Step response of the linear closed-loop of the best compromise solutions.

$$\bar{\eta} = \frac{\sum_{i=1}^{p} z_i}{p} \tag{3.8}$$

where z represents the normalized objective values, i.e., the original objective values divided by the maximum corresponding objective value; and p is the number of objective functions. In this sense, applying this comparison parameter to the objective values presented in Table 3.2 turns out in Table 3.3.

The performance overall mean evidenced that the alternative with the lowest value is the multiobjective approach using the SLC considering only the optimal values from the Pareto front. However, even the approach using all candidate solutions presented

Table 3.3 - Performance overall mean analysis of the design optimization problem.

Approach	Overshoot	Settling time	$\bar{\eta}$
All points	0.92	0.75	0.84
Only Pareto front	0.88	0.74	**0.81**
Actuator 1	0.85	1.00	0.93
Actuator 2	0.96	0.80	0.88
Actuator 3	1.00	0.70	0.85

a better values than the other options. The analysis covered in this chapter was a brief example of multiobjective optimization application and an introduction to the actuators command problem. The optimal design problem of a linear time-invariant control system composed of three conflicting parallel linear first-order actuators have been solved herein. It has been shown that a good performance, in terms of overshoot and settling time, can be achieved using a systematic multiobjective methodology when a fixed scenario is provided. Unlike this case, nonlinear complex systems will be treated in the following chapters.

4 AMCM-I: A SOLUTION TO THE MIXED ACTUATORS PROBLEM

The spacecraft control problem using a set of actuators with conflicting characteristics is investigated in this chapter. A novel approach, called **Actuator Multiobjective Command Method I** (AMCM-I), based on a discrete multiobjective optimization technique is proposed. The method is included in a coupled translational and attitude control system applied to the final approach rendezvous. Furthermore, all elements of the guidance, navigation and control loop have been developed and implemented in a simulation framework, as described in Chapter 2. A reaction control system, a set of reaction wheels, and a set of magnetic torqrods are the group of actuators under analysis. The AMCM-I is responsible for commanding the necessary torque for the actuators at every control cycle based on the requested torque level and the current situation of the actuators dynamics.

4.1 Actuator Multiobjective Command Method I

Here, the discrete multiobjective optimization problem is formulated with four objectives functions: torque error (Z_1), fuel and electrical charge consumption (Z_2), disturbance of coupling (Z_3), and risk of utilization (Z_4). All these elements are the components of the objective function vector, $\mathbf{Z}(\mathbf{x})$, which shall be minimized. The mathematical formulation of AMCM-I is given by

$$\begin{array}{lrcl}
\text{Minimize} & \mathbf{Z}(\mathbf{x}) & = & [Z_1(\mathbf{x}), Z_2(\mathbf{x}), Z_3(\mathbf{x}), Z_4(\mathbf{x})] \\
 & \mathbf{x} & = & \dfrac{\mathbf{p}}{k}|T_c| \\
 & & & \\
 & Z_1(x_1, x_2, x_3) & = & T_r^a(x_1) + T_w^a(x_2) + T_m^a(x_3) - |T_c| \\
 & Z_2(x_1, x_2, x_3) & = & c_1x_1 + c_2x_2 + c_3x_3 \\
 & Z_3(x_1, x_2, x_3) & = & i_1x_1 + i_2x_2 + i_3x_3 \\
 & Z_4(x_1, x_2, x_3) & = & r_1x_1 + r_2x_2 + r_3x_3 \\
 & & & \\
\text{subject to} & x_1, x_2, x_3 & \geqslant & 0 \\
 & p_1 + p_2 + p_3 & = & k \\
 & \Rightarrow x_1 + x_2 + x_3 & = & |T_c| \\
 & k & = & \dfrac{\Delta h_c}{\Delta h_a}
\end{array} \tag{4.1}$$

where Δh_a is the actuator sample period; Δh_c is the controller sample period; k is the number of subsets; and T_c is the control torque requested by the PID controller.

The first objective function, Z_1 (*torque error*), measures the difference among the requested torque from the PID controller and the total applied torque. The second objective function, Z_2 (*fuel and electrical charge consumption*), represents the total amount of propellant mass and electrical charge consumed by the set of actuators. The third objective function, Z_3 (*disturbance of coupling*), represents the actuator's disturbance effect on the spacecraft axes. The last objective function, Z_4 (*risk of utilization*), takes into account the failure rate of each actuator, as defined in Chapter 2. All objectives functions are evaluated at every control cycle and they measure, in a general way, the cost and efficiency of the actuators.

The discrete decision variable vector, $\mathbf{x}$, represents combinatorial combinations of the torque control signal commanded to the actuators. The decision variable vector is composed of three components (x_1, x_2, x_3) which represent the command torque signal to the actuators: reaction thrusters, reaction wheels, and magnetic torqrods, respectively. The coefficients c_j, i_j and r_j (with j = 1,2 and 3) are constant values used in the equations Z_2, Z_3, and Z_4, respectively. Such coefficients allow to establish the tradeoff among the objective functions. Therefore, a conflicting scenario has been designed such that, for instance, the actuator which exhibits the lowest coupling disturbance effect, it can also present the highest failure rate; as well as the cheapest actuator, in terms of consumption, can present the highest level of coupling disturbance. These coefficients have been defined according to the characteristics of the actuators. It is worth mentioning that the set of actuators is defined a priori. It is not the purpose of this work to find an optimal configuration of actuators. Although the modeling of the actuators is based on realistic parameters provided by suppliers. Therefore the focus of this thesis is, for a given set of actuators with conflicting characteristics, there shall be defined the best way to operate them.

The vector $\mathbf{p} \in \mathbb{R}^n$ denotes the combinatorial variable whose function is to quantize the torque command of the controller to generate the decision variables. The combinatorial problem, addressed in Equation 4.1, can be solved using the k-combination with repetitions equation (also called by k-multicombinations). This theory allows to calculate the number of ways to sample k elements from a set of n elements allowing for duplicates. Hence, the number of multisubsets of size k is then the number of non-negative integer solutions of the linear Diophantine equation (BRUALDI, 1992), given as follows

$$x_1 + x_2 + x_3 + ... + x_n = k \tag{4.2}$$

If a given set has n elements, then the number of such k-multisubsets can be written as

$$\begin{pmatrix} n+k-1 \\ k \end{pmatrix} = \frac{(n-1+k)!}{(n-1)!k!} \tag{4.3}$$

Note that, with respect to the problem discussed in this chapter, n represents the number of decision variables, i.e, the number of actuators ($n = 3$), whereas k is the number of divisions of a given parameter. Since the actuators model executes 10 times faster than the control cycle, then the control cycle is split in 10 parts ($k = 10$). Equation 4.3 has been used to solve the combinatorial problem addressed in the constraints of Equation 4.1: $p_1+p_2+p_3 = k$. In this sense, the set of candidate solutions has a finite amount of 66 elements. The number of solutions could be increased in order to have more points in the objective space, but this action would increase the computational effort of the simulation. Table 4.1 presents some of the 66 possible combinations which solve the combinatorial problem and compose the candidate solution of the decision space.

Table 4.1 - Combination table which solves the combinatorial problem.

Solution	p_1	p_2	p_3	k
1	0	0	10	10
2	0	1	9	10
3	0	2	8	10
4	0	3	7	10
5	0	4	6	10
⋮	⋮	⋮	⋮	⋮
62	8	1	1	10
63	8	2	0	10
64	9	0	1	10
65	9	1	0	10
66	10	0	0	10

The complete mathematical modeling of spacecraft actuators can be a cumbersome task due to its complexity and nonlinear dynamical behavior (KRISTIANSEN; HAGEN, 2009). Herein, AMCM-I needs to know a priori the error level of each actuator as a function of the candidate torque solution (x_1, x_2, x_3). Since is difficult to carry out laboratory testing, then a curve fitting analysis has been performed in order to determine the actuator's dynamic equations. Such equations, called *test torque theoretical functions*, consider the same nonlinearities parameters, like biases and random errors, of the actuators models. In Equation 4.1, $T_r^a(x_1)$, $T_w^a(x_2)$, and $T_m^a(x_3)$ are the test torque theoretical functions of the reaction thruster, reaction wheel, and magnetic torqrod, respectively. The resulting mathematical equations are given by

$$T_r^a(x_1) = \begin{cases} T_r^{max} + \bar{w} & \text{for} \quad x_1 \geqslant T_r^{max} \\ x_1 + \bar{w} & \text{for} \quad 0 < x_1 < T_r^{max} \\ 0 & \text{for} \quad x_1 = 0 \end{cases} \tag{4.4}$$

$$T_w^a(x_2) = \begin{cases} x_2 + w + b_s & \text{for} \quad x_2 \leqslant T_w^{max} \\ T_w^{max} + w + b_s & \text{for} \quad x_2 > T_w^{max} \end{cases} \tag{4.5}$$

$$T_m^a(x_3) = \begin{cases} (a_m x_3^2 + b_m x_3) + w + b_s & \text{for} \quad x_3 \leqslant T_m^{max} \\ T_m^{max} + w + b_s & \text{for} \quad x_3 > T_m^{max} \end{cases} \tag{4.6}$$

where the superscript ^{max} represents the theoretical maximum torque applied by the actuator; w is the white Gaussian noise whose statistics is given by $w = N(0, Q)$, i.e., zero mean and covariance Q; b_s is the bias error; and a_m and b_m are the coefficients of a second degree polynomial that best fit the torque curve of the magnetic torqrod. The torque error delivered by the thrusters is quite difficult to determine because it depends on the requested force, in other words, the error does not follow a Gaussian behavior. In this case, it is assumed the average torque error $\bar{w}$ of the last 100 step times applied by the RCS. Concisely, AMCM-I evaluates the objective functions at every control cycle and selects the best compromise solution based on a discrete multiobjective optimization methodology. This iterative functional concept of AMCM-I coupled to the GNC loop is illustrated in Figure 4.1.

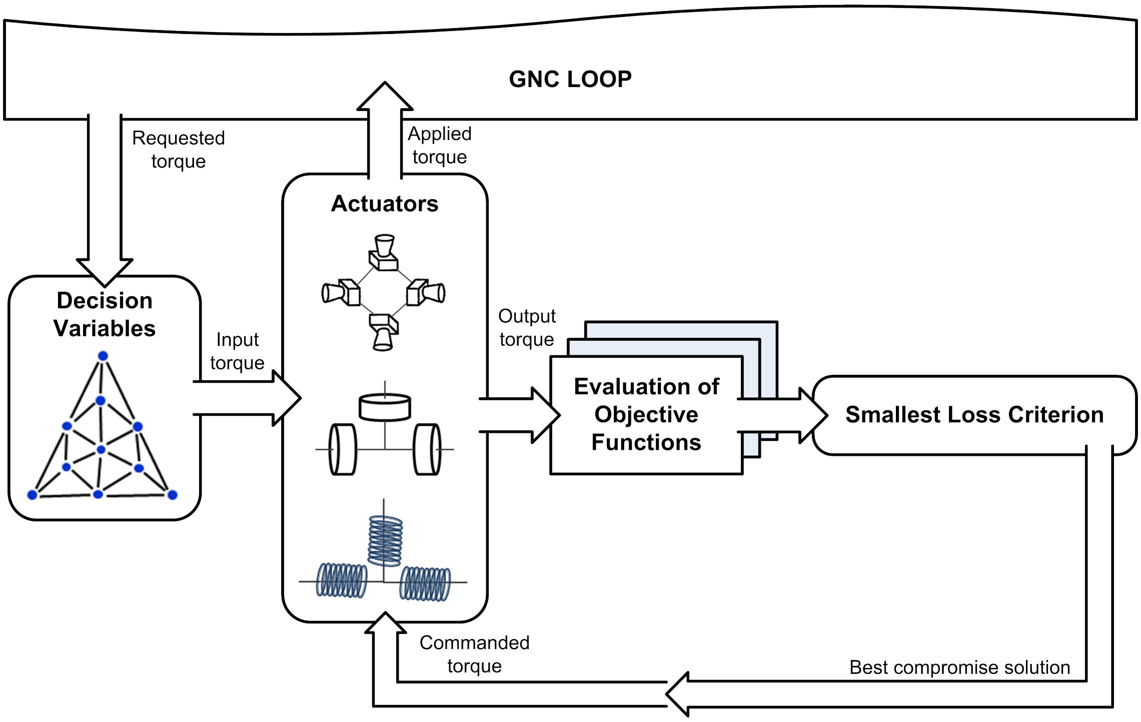
GNC LOOP
Requested torque
Applied torque
Actuators
Decision Variables
Input torque
Output torque
Evaluation of Objective Functions
Smallest Loss Criterion
Commanded torque
Best compromise solution

Figure 4.1 - Functional concept of the Actuator Multiobjective Command Method I.

Figure 4.2 exhibits the flowchart of the multiobjective optimization process of AMCM-I. The first step is loading the simulation parameters. Then the combinatorial variables are loaded in order to generate the decision space which is composed of all candidate commanded torque solutions. At this step, it is used the control torque provided by the PID controller. In the following step, all test torque theoretical functions are evaluated in order to determine the error level of each actuator for every candidate commanded torque. Hence the objective space is created. If the approach consider only the Pareto front, as assumed in this case, then the non-dominated solution must be properly sorted out. The step from the computation of the maximum values until the identification of the best compromise solution is exactly the same as described in Chapter 3. The last step is the command of the actuators.

4.2 RCS Configuration

In this case, the RCS is composed of 12 one-sided thrusters. Figure 4.3 illustrates the assumed set-up of thrusters. Based on the placement and orientation of each thruster, the configuration matrix is defined using Equations 2.33 and 2.34. It is expressed in terms of the maximum thrust level F_n and the maximum achievable torque, such as

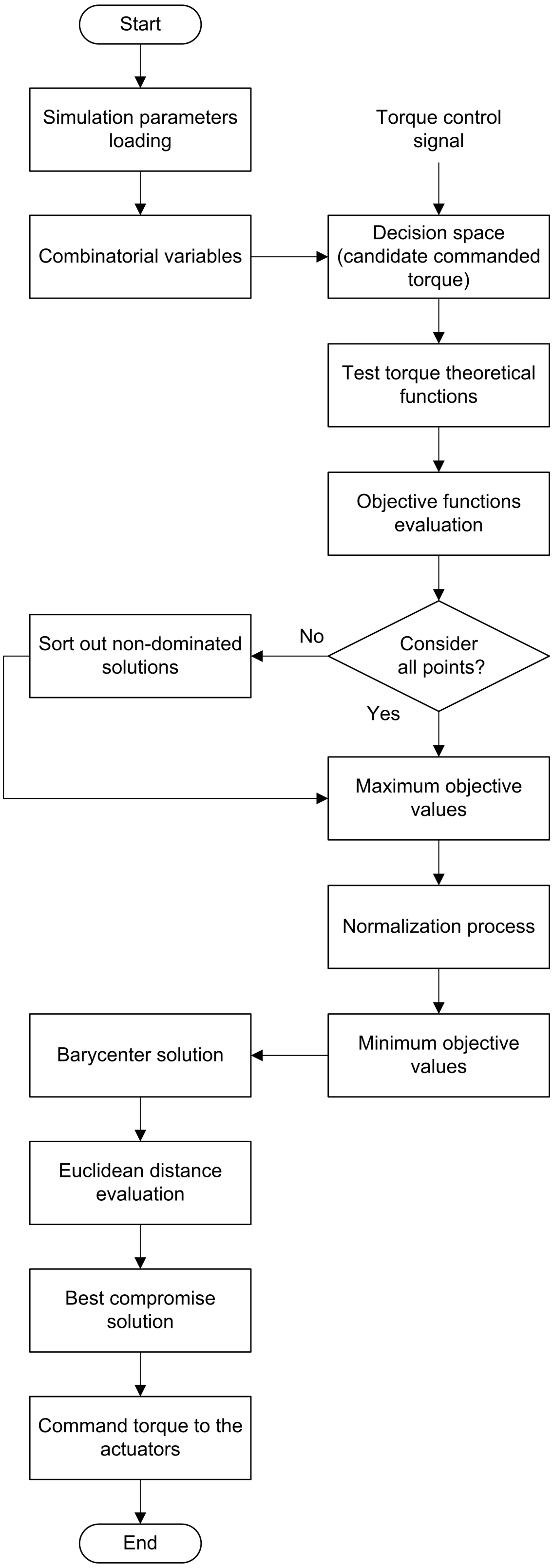
Start
Simulation parameters loading
Torque control signal
Combinatorial variables
Decision space (candidate commanded torque)
Test torque theoretical functions
Objective functions evaluation
Sort out non-dominated solutions
No
Consider all points?
Yes
Maximum objective values
Normalization process
Barycenter solution
Minimum objective values
Euclidean distance evaluation
Best compromise solution
Command torque to the actuators
End

Figure 4.2 - Flowchart of the multiobjective optimization process of AMCM-I.

$$\mathbf{A} = \begin{bmatrix} F_n & F_n & 0 & 0 & 0 & 0 & -F_n & -F_n & 0 & 0 & 0 & 0 \\ 0 & 0 & F_n & F_n & 0 & 0 & 0 & 0 & -F_n & -F_n & 0 & 0 \\ 0 & 0 & 0 & 0 & F_n & F_n & 0 & 0 & 0 & 0 & -F_n & -F_n \\ 0 & 0 & 0 & 0 & T_n & -T_n & 0 & 0 & 0 & 0 & -T_n & T_n \\ T_n & -T_n & 0 & 0 & 0 & 0 & -T_n & T_n & 0 & 0 & 0 & 0 \\ 0 & 0 & T_n & -T_n & 0 & 0 & 0 & 0 & -T_n & T_n & 0 & 0 \end{bmatrix} \tag{4.7}$$

where $T_n = F_n r_b$ is the applied nominal torque; and r_b represents the distance of the ith thruster from the CoM of the body vehicle.

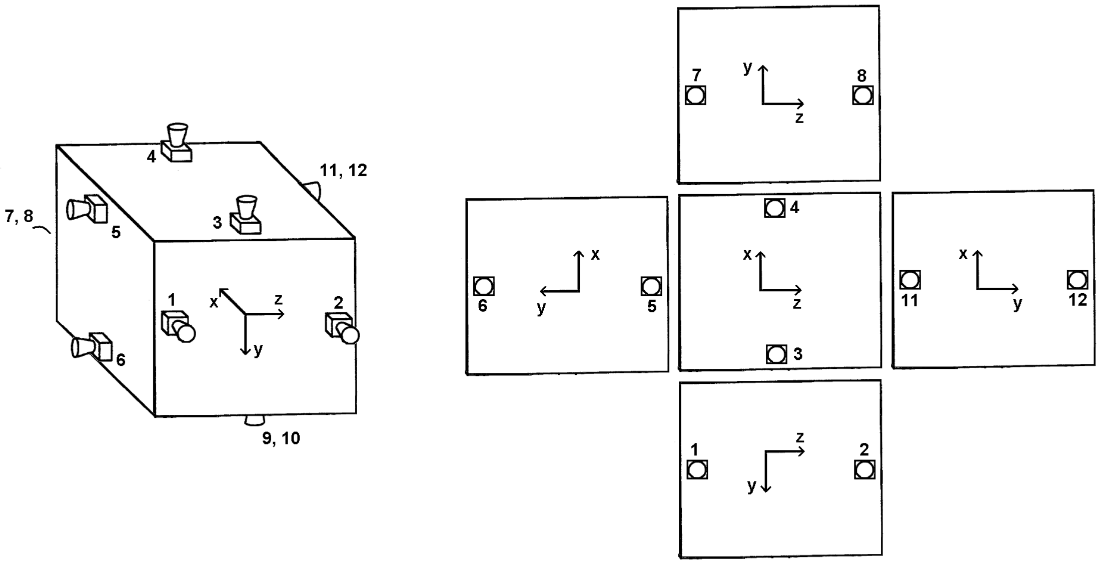

Figure 4.3 - Thrusters' location and orientation ($n = 12$).

4.3 Purely Numerical Simulations

Numerical simulations of AMCM-I applied to the coupled rendezvous and attitude control system are presented in this section. Table 4.2 introduces the main parameters of the simulations. The actuator and sensor parameters are based on data sheets provided by manufacturers.

The multiobjective coefficients, **c**, **i**, and **r**, establish the tradeoff among the objectives Z_2, Z_3, and Z_4. The coefficients **c** and **i** were defined based on simulations of the models of actuators whereas the coefficient **r** was defined arbitrarily. Figure 4.4

Table 4.2 - Simulation parameters.

Orbit parameters	**Value**
Altitude, km	450
Eccentricity	0
Inclination, degrees	45
Mean anomaly, degrees	90
Satellite parameters	
Moment of inertia, kg.m^2	[100, 120, 80]
Initial mass, kg	500
Arm length, m	0.5
Stellar attitude sensor	
Spatial random error, arcsecond	18.9, 3σ
Spatial bias error, arcsecond	10, 3σ
Camera CCD sensor	
Focal length, pixels	604
Resolution, pixels	640 × 480
Multiobjective coefficients	
Fuel and electrical charge consumption ($\mathbf{c}$)	[3, 2, 1]
Disturbance of coupling ($\mathbf{i}$)	[2, 1, 3]
Risk of utilization ($\mathbf{r}$)	[1, 3, 2]
RCS parameters	
Propellant	Cold gas
Thrust, N	0.5
MIB, Ns	0.05
Reaction wheel parameters	
Wheel moment of inertia, kg.m^2	0.0191
Maximum torque, Nm	0.054
Magnetic torqrod parameters	
Magnetic dipole moment, Am^2	170
Maximum torque[*], Nm	0.012

[*] Achieved with the Earth's magnetic field in the particular orbital position.

illustrates the tradeoff scenario presenting the performance level of each actuator. The lines show the objective functions Z_2, Z_3, and Z_4, whereas the columns show the three performance levels for each objective: (1) good, (2) regular, and (3) bad. For instance, the magnetic torqrod presents the lowest cost of Z_2, the worst behavior of Z_3, and a regular level of Z_4. Concerning the reaction wheel, it presents the best cost of Z_3, the worst level of Z_4, and a regular behavior of Z_3; and so on.

Performance Objectives	(1) GOOD	(2) REGULAR	(3) BAD
Fuel and electric charge consumption (Z_2)	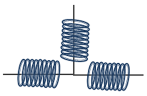	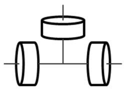	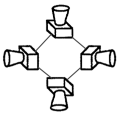
Disturbance of coupling (Z_3)	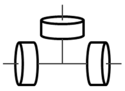	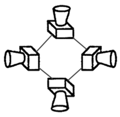	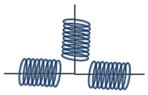
Risk of utilization (Z_4)	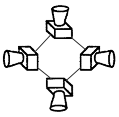	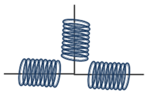	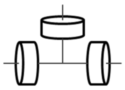

Figure 4.4 - Tradeoff scenario for the mixed actuators problem.

4.3.1 Control Cycle Analysis

The combinatorial variables play an important role in this process by the quantization of the control signal. They change the decision variables, expressed by the torque commanded to the actuators, proportionally. The combinatorial space, composed of 66 elements, is illustrated in Figure 4.5. The dimensionless combinatorial variable 1, 2, and 3, are related to the decision variables: reaction thruster, reaction wheel, and magnetic torqrod, respectively. Each point in the plot provides the contribution of the actuators for meeting the requested torque. For example, the extreme points mean that the requested torque is satisfied with just one type of actuator whereas the intermediate points represent that the requested torque is provided by a combination of actuators.

The presentation of results is fundamental for the success of any project. However, this step is usually difficult in multiobjective analysis, where the amount of relevant information increases with the objectives. Even with few points, the three-objective graphical display may be considered awkward to understand. For more than three objectives, graphical displays on orthogonal axes must be dropped. An alternative to the typical graphical displays, adaptable to any number of objectives, was proposed by Schilling et al. (1983): the value path plot. The display consists of a set of parallel scales (one representing each objective) on which is drawn a line (a value path) that connects the objective values between the scales. This representation allows considering simultaneously a large number of objectives. Figure 4.6, Figure 4.7, and

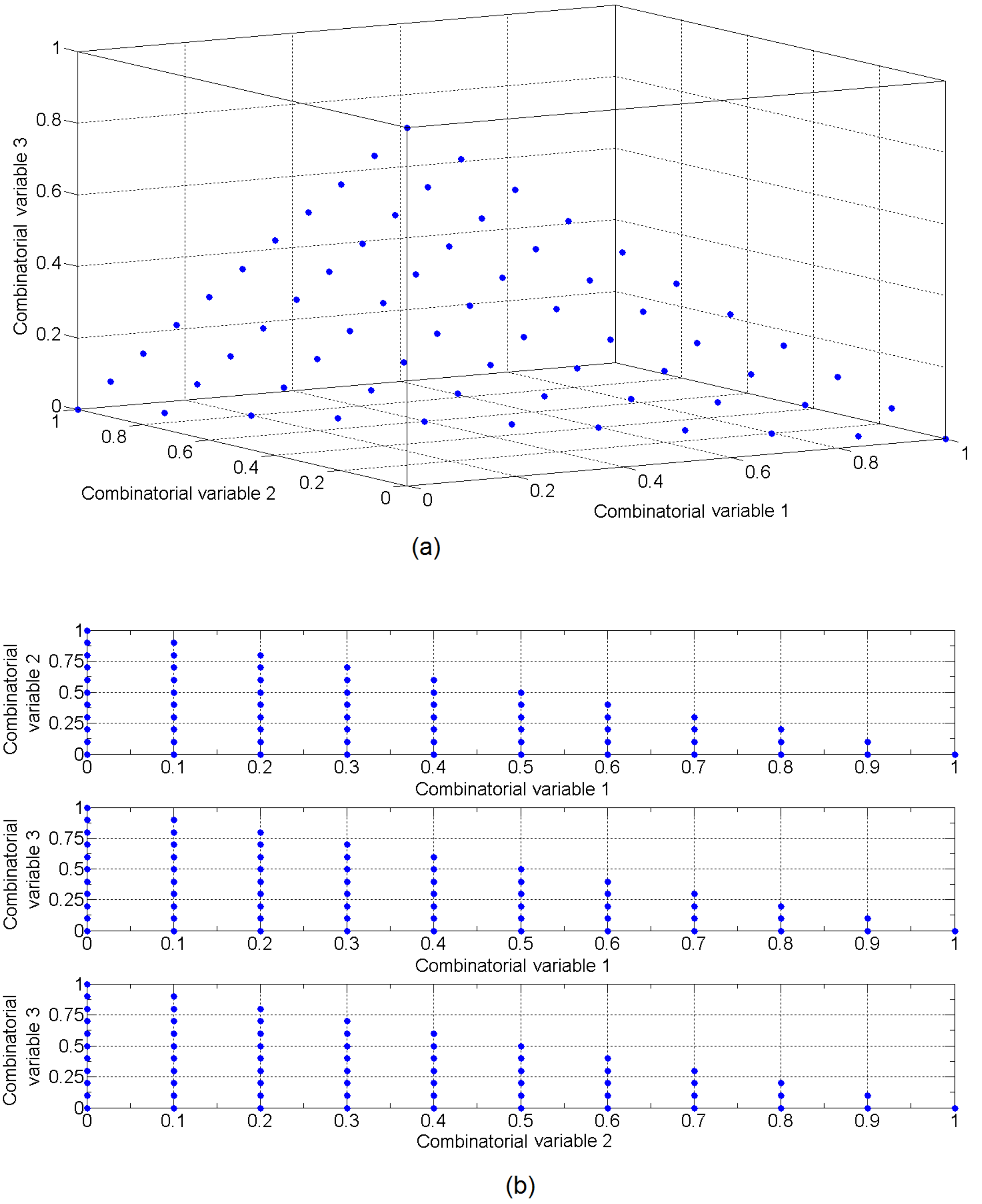

Figure 4.5 - Combinatorial space of the discrete multiobjective problem: (a) 3D representation; (b) 2D representation.

Figure 4.8 show the value path plot of AMCM-I for three different requested torque levels: 0.015 Nm, 0.050 Nm and 0.085 Nm, respectively.

The vertical axes represent the normalized scale of the objective functions, whose labels are shown in the horizontal axis. Every line represents a candidate solution.

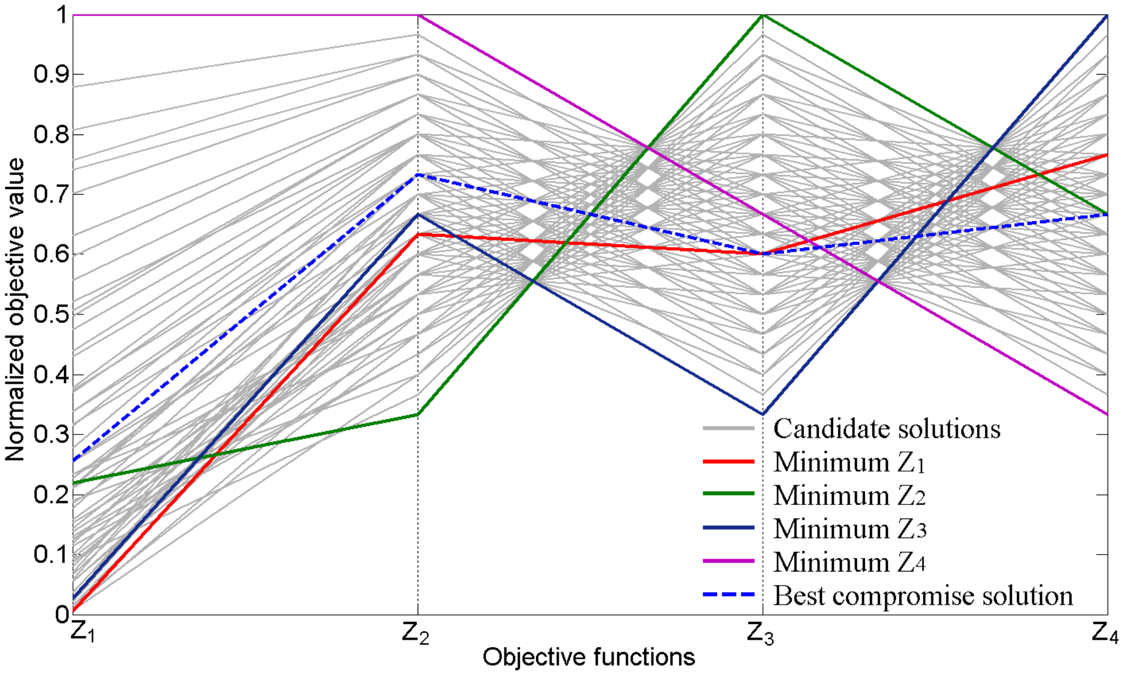

Figure 4.6 - Value path plot of AMCM-I for requested torque level of 0.015 Nm.

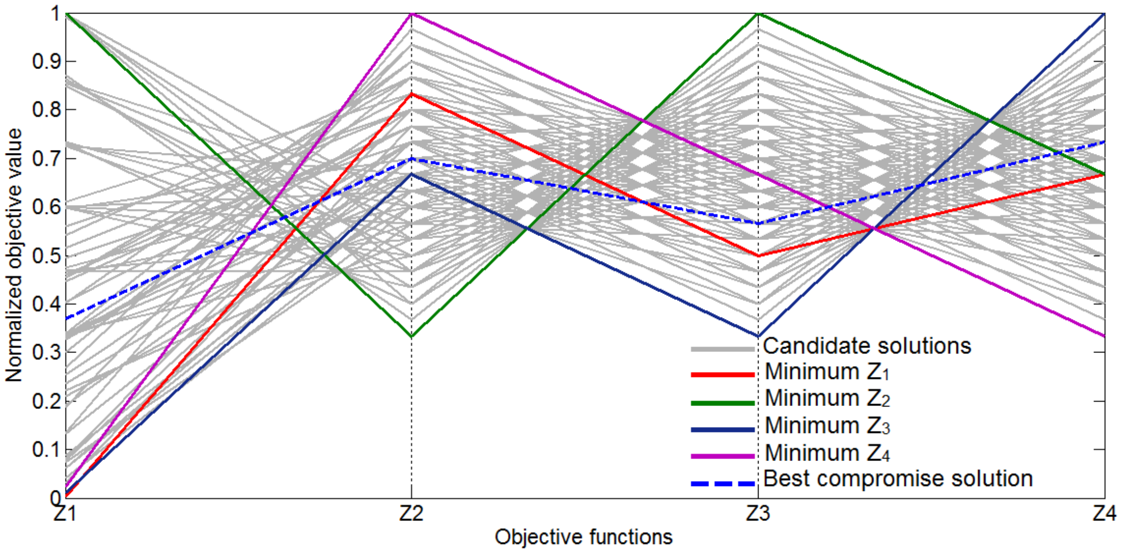

Figure 4.7 - Value path plot of AMCM-I for requested torque level of 0.050 Nm.

The optimal solution of each objective, also called primary paths, is represented by a thick line: the red line optimizes Z_1, the green line optimizes Z_2, the dark blue line optimizes Z_3, and the purple line optimizes Z_4. The best compromise solution, obtained with the decision making method SLC, is represented by the blue dashed line. The necessary condition for noninferiority in this kind of plot is the value path

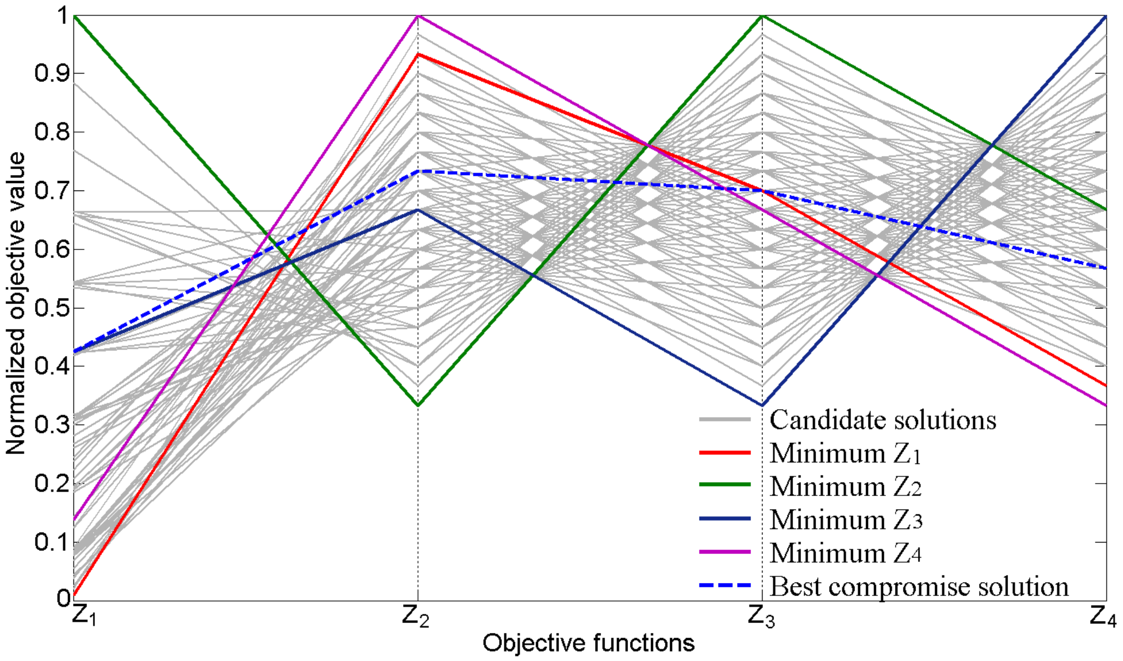

Figure 4.8 - Value path plot of AMCM-I for requested torque level of 0.085 Nm.

must intersect all primary paths (SCHILLING et al., 1983). Therefore, we can conclude that all candidate solutions belong to the noninferior set. Note also that sometimes a particular solution optimizes one objective, but provides the highest values for others, e.g., the primary path of Z_4 (purple thick line) in Figure 4.6.

It is worth pointing out that the best compromise solution is clearly an equilibrium solution among the primary paths, as defined by the SLC. At every control cycle, new shapes of value path plots are generated. Thereupon, the torque is split according to the requested torque level, i.e., the commanded torque for each actuator changes constantly. The pie charts presented in Figure 4.9 show the decision values of the best compromise solution exhibited from Figures 4.6 to 4.8. These values represent the contribution percentage of each actuator. As can be seen, in Figure 4.9(a) the major contributions are given by the reaction thruster and the reaction wheel with identical values, whereas in Figure 4.9(b), the major contribution is given by the reaction wheel, and in Figure 4.9(c), since the requested torque level has increased, AMCM-I commanded 50% of the torque to the reaction thruster because its higher capacity.

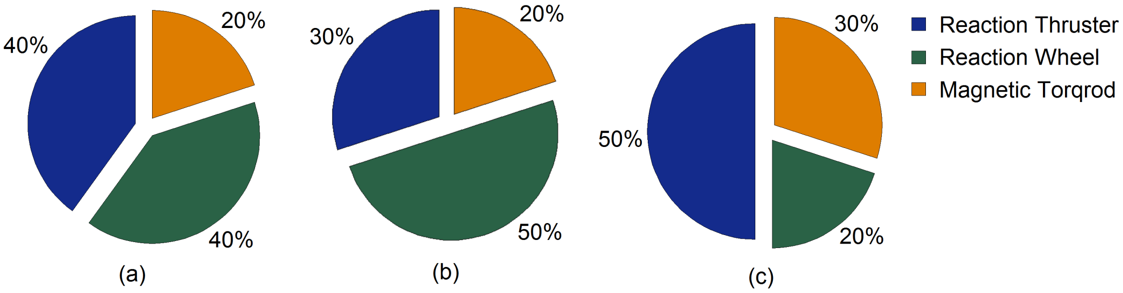

Figure 4.9 - AMCM-I commanded torque: (a) requested torque of 0.015 Nm; (b) requested torque of 0.050 Nm; (c) requested torque of 0.085 Nm.

4.3.2 Comparative Analysis of AMCM-I

So far, AMCM-I has been analyzed from a viewpoint of a particular control cycle. However, it makes necessary to examine also the AMCM-I's performance throughout the whole maneuver. Hence a final approach rendezvous simulation has been executed from 20 m to 10 m. An initial angular error - difference between the actual attitude and the guidance values - of 10 degrees in the Y_B axis and null errors for the other axes, have been assumed in this simulation. The time angular response, which represents the time spent by each actuator to mitigate the angular error, is presented in Figure 4.10. Four operations mode are compared: all-reaction thruster, all-reaction wheel, all-magnetic torqrod, and AMCM-I. The horizontal axis represents the time necessary to execute the attitude maneuver whereas the vertical axis represents the angular motion. We can observe that although the magnetic torqrod provided the slowest response with the second highest overshoot, the steady state was still achieved. The reaction thruster's response was a little faster but also shown a overshoot and a disturbing behavior in the other axes due to its coupling to the rendezvous control system. Analyzing only the angular motion of the Y_B axis, we can see that the response from AMCM-I and reaction wheel are very similar. Even though a short period of disturbance in X_B and Z_B axes, AMCM-I has properly worked in the closed-loop control system.

In order to measure the efficiency of the proposed method over the GNC loop, some performance parameters have been analyzed, as shown in Figure 4.11, such as: angular error integrated over time, fuel consumption, electric charge consumption, and settling time of the angular response. In fact, they are correlated with the objectives functions and represent another way to look through the performance. In addition, the normalized objective values of the disturbance of coupling (Z_3) and risk of utilization (Z_4) have also been analyzed. Here, each bar represents a

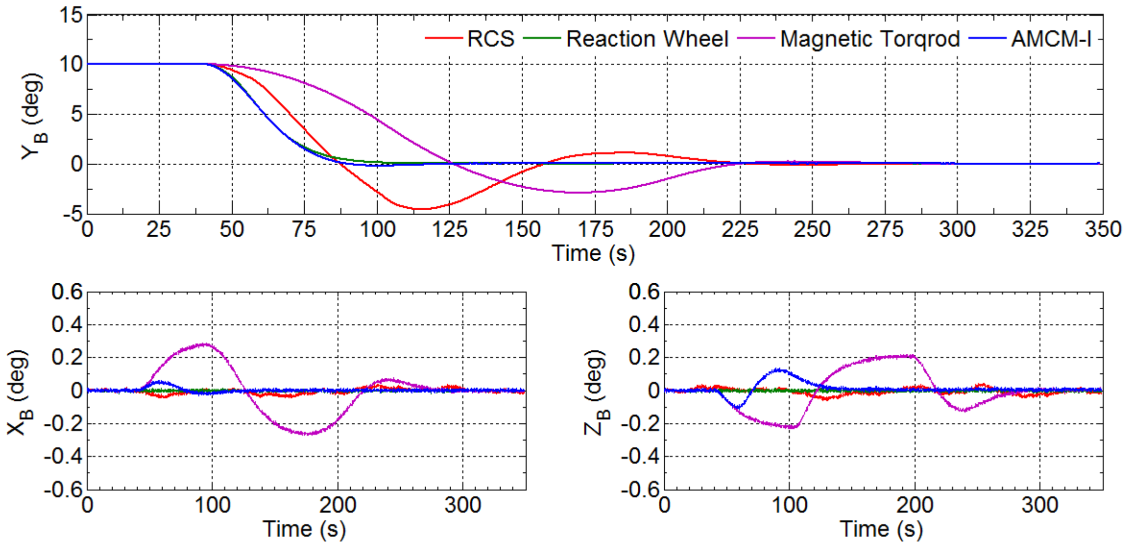

Figure 4.10 - Time angular response of different operation modes.

different configuration of actuators, i.e., only RCS, RCS with reaction wheels, RCS with magnetic torqrods, and AMCM-I. The first configuration uses RCS to control both translational and rotational motions. The second and third configurations use thrusters only for controlling the translational motion. Reaction wheels on the second configuration and magnetic torqrods on the third configuration are used to control the rotational motion.

Figure 4.11(a) presents the angular error of all axes integrated throughout the simulation for each actuator mode. As expected, the magnetic torqrod had the highest value. The results provided by AMCM-I and reaction wheel were quite similar: 4.28 and 4.18 respectively. Concerning the propellant consumption shown in Figure 4.11(b), the consumed amount of propellant between the RCS configuration and the other alternatives was very close. The unique difference between both configurations is the application of thrust to control the rotational motion (in AMCM-I case, thrusters are used sporadically), since RCS has been used in all cases to control the translational motion. If we consider that a thrust of 0.5 N is applied constantly throughout the control cycle, then the propellant mass rate would be of 0.0001 kg/s. This fact explains why the difference between the first case and the others is just 0.01 kg.

For obvious reasons, the electric charge consumption, shown in Figure 4.11(c), is null for the reaction thrusters alternative and should not be taking into account in the comparison. The electric signal to command the valve of the thruster has not

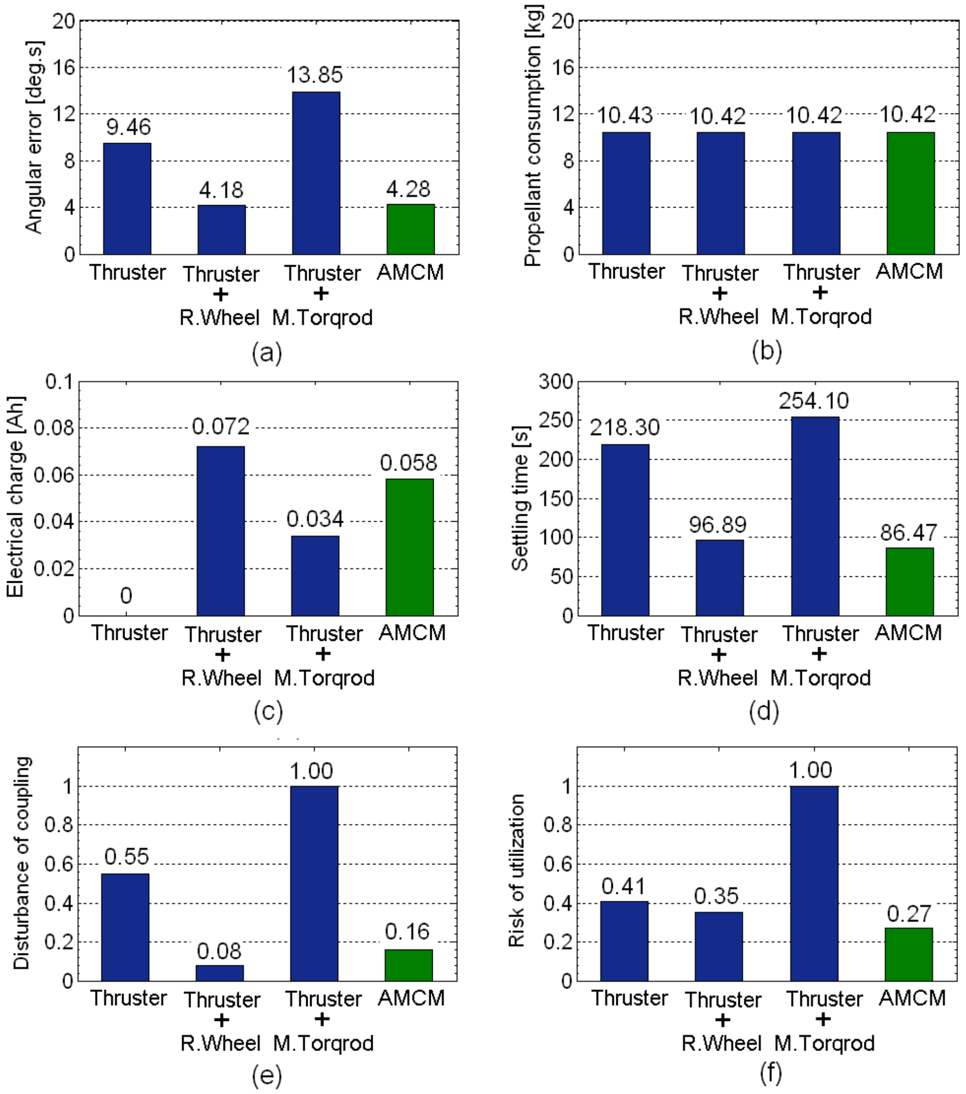

Figure 4.11 - Performance parameters of the GNC loop: (a) angular error integrated over time; (b) fuel consumption; (c) electric charge consumption; (d) settling time of the angular response; (e) disturbance of coupling (normalized Z_3); and (f) risk of utilization (normalized Z_4).

been considered. The reaction wheel had a higher consumption than the magnetic torqrod whereas AMCM-I presented an intermediate result. The settling time of the time angular response is analyzed in Figure 4.11(d). In fact, Figure 4.11(a) and Figure 4.11(d) just quantify what was previously shown in Figure 4.10. The fastest response was achieved with AMCM-I (86.47 s) followed by the reaction wheel's response (96.89 s). As expected, in Figure 4.11(e), the configuration using reaction wheels had the lowest value of normalized Z_3 (disturbance of coupling) followed by the response of AMCM-I. Finally, concerning the Figure 4.11(f), the proposed method presented the lowest rate of failure of the simulation.

For an alternative comparison purpose, the performance overall mean, defined in Equation 3.8, of the mixed actuators problem is presented in Table 4.3.

Table 4.3 - Performance overall mean analysis of the mixed actuators problem.

Performance parameter	RCS	RCS + RW	RCS + MT	AMCM-I
Angular error	0.68	0.30	1.00	0.31
Propellant consumption	1.00	0.999	0.999	0.999
Electric charge consumption	0	1.00	0.47	0.81
Settling time	0.86	0.38	1.00	0.34
Normalized Z_3	0.55	0.08	1.00	0.16
Normalized Z_4	0.41	0.35	1.00	0.27
$\bar{\eta}$	0.58	0.52	0.91	**0.48**

Note that the proposed method presented the lowest performance overall mean adducing the efficiency of such approach. In few words, the approach AMCM-I achieved a satisfactory angular error, an accepted amount of fuel and electrical charge consumptions, low levels of disturbance of coupling and risk of utilization, with the fastest settling time when compared to the others configurations.

4.3.3 Complete Rendezvous and Attitude Simulation using AMCM-I

As the propose method has presented satisfactory results with respect to the multiobjective analysis so far, it would be convenient to analyze also all main variables of a complete rendezvous and attitude maneuver. In this sense, the time translational response of the final approach rendezvous is shown in Figure 4.12. On the left side is presented the approach motion along V-bar (X axis) whereas the motion under the remaining axes (Y and Z) are brought out on the right side of the figure. Three states are disclosed in this plot: the real state provided by the dynamics, the state measured by the sensors, and the state smoothed by the filter. It is important to point out the reduction of the measurement noise insofar as the chaser vehicle approaches the target vehicle. Likewise, the time translational velocity plot, shown in Figure 4.13, evidences the translation guidance profile used in this thesis. It is possible to note the acceleration and deceleration phases as well as the period of constant velocity: 0.05 m/s in this case.

In rendezvous literature, it is common to plot the chaser's trajectory evolution in a R-bar-V-bar plane, as shown in Figure 4.14. This motion represents the real translational motion of the chaser vehicle. In such figure, the point [10,0] corresponds to

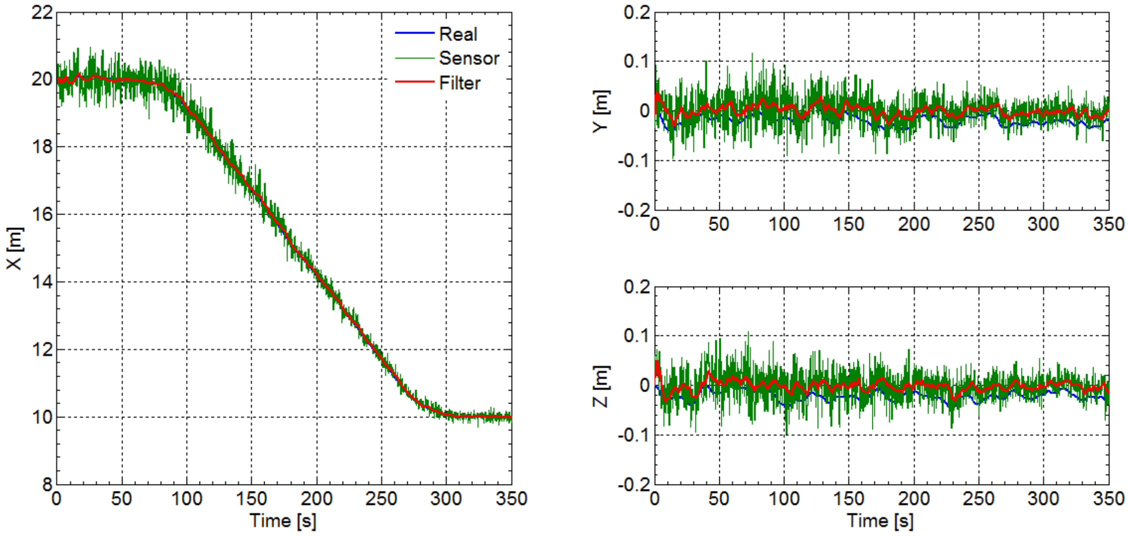

Figure 4.12 - Time translational position response of a spacecraft composed of actuators commanded by AMCM-I.

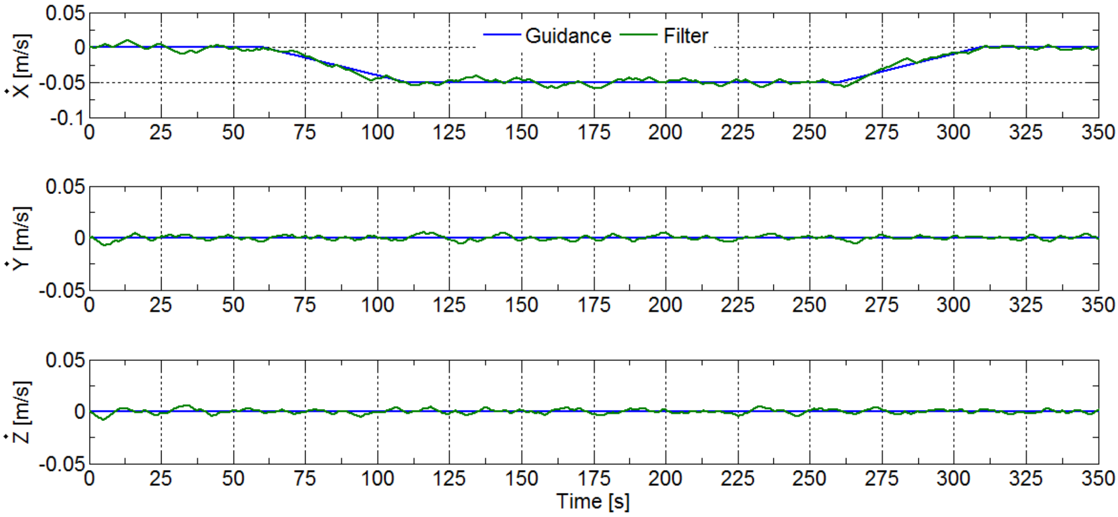

Figure 4.13 - Time translational velocity response of a spacecraft composed of actuators commanded by AMCM-I.

the final hold point whereas the point [20,0] is the initial hold point. The chaser vehicle departs from the latter point toward the former one. Note that the approach motion is a quasi-straight line trajectory performed by a multitude of small hops, as described by Fehse (2003).

An outstanding way of analyzing the performance of a control system is through the visualization of the loop errors. Figure 4.15 shows four different types of translational

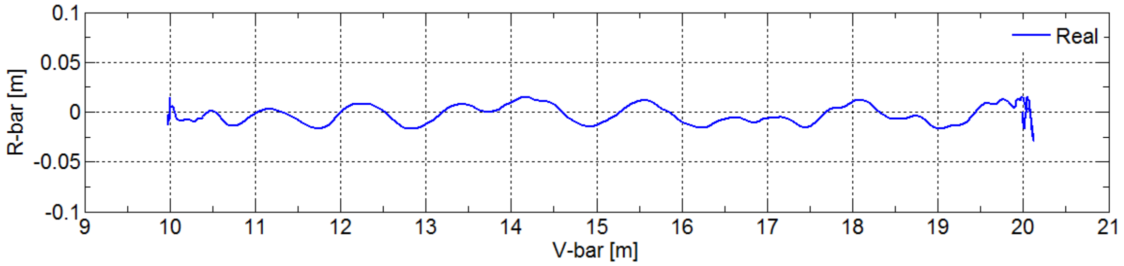

Figure 4.14 - Approach motion in target centered frame.

position error: sensor minus real state and filter minus real state on the left side; and guidance minus real and guidance minus filter on the right side. The efficiency of the filter has been proved through the plots on the left side. Regarding the results including the guidance (on the right side), it is worth mentioning that the guidance minus real error takes into account the bias error of the sensor whereas the guidance minus filter error does not.

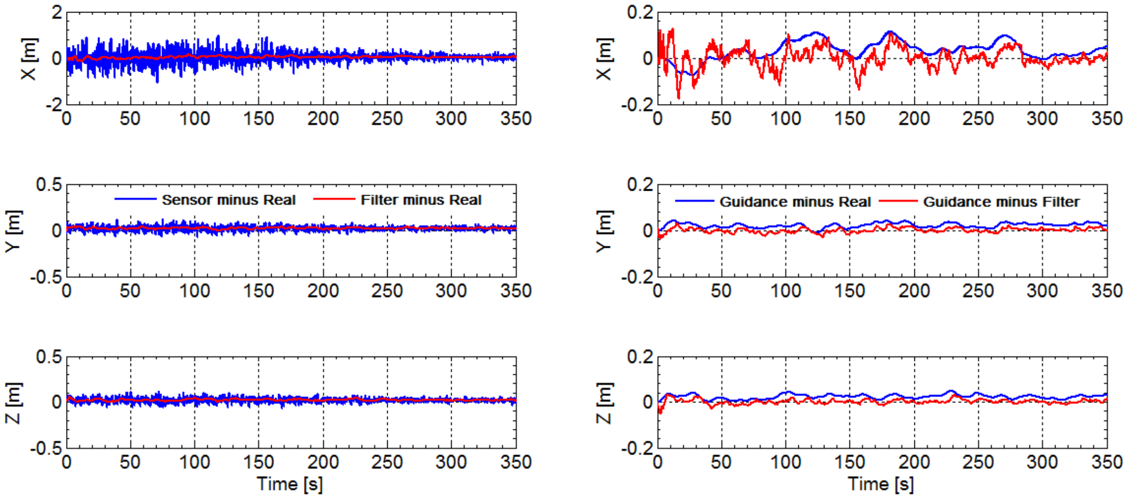

Figure 4.15 - AMCM-I: GNC loop errors including the real position (left) and the guidance position (right).

The time angular response using AMCM-I to command the actuators is exhibited in Figure 4.16. Such plot shows the attitude guidance profile and the response provided by the attitude sensor. Initially, the vehicle keeps its current angular position at the initial hold point of 20 m in V-bar axis. At the time of 60 s, the attitude motion starts in order to correct an initial angular error of 10 degrees in Y_B axis. As discussed earlier in Chapter 2, the attitude guidance profile acts in order to keep the chaser body frame aligned to the target docking axis. However, the guidance behavior is very close to zero because of the short proximity between chaser and target vehicles.

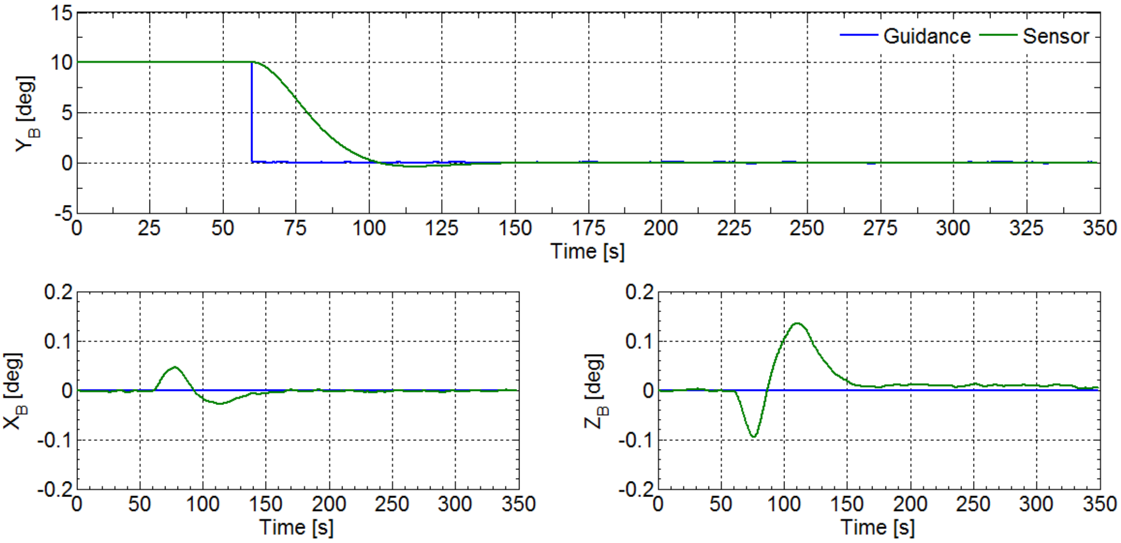

Figure 4.16 - Time angular response of a spacecraft composed of actuators commanded by AMCM-I.

Figure 4.17 presents the frequency of activation of each actuator throughout the simulation. The bars represent the frequency, in number of simulation steps, that a given commanded torque, in percentage, was sent to the actuator. Note that the most commanded torque vector was 30 %, 50 %, and 20 % for the reaction thruster, reaction wheel, and magnetic torqrod, respectively. It is worth remembering that these values represent the commanded torque which can be different from the applied one due to limitations and characteristics of the actuators. AMCM-I takes into account this constraint and selects the best solution even if the commanded torque is not applied.

Figure 4.18 shows the thrust pulses applied by the RCS (left) and the combination of torque (right) applied by all actuators: reaction wheels, magnetic torqrods, and RCS. As can be observed mainly on Y_B axis of the right side, AMCM-I has managed the actuators for providing the torque command only when requested by the multiobjective method. Note that the RCS had a more active participation when the attitude maneuver started about the time 60 s. After this period, the application of torque pulses became sporadic. On the other hand, torque applied by the reaction wheels and magnetic torqrods worked for keeping the fine pointing throughout the maneuver. Analyzing the torque magnitude delivered by each actuator we can see

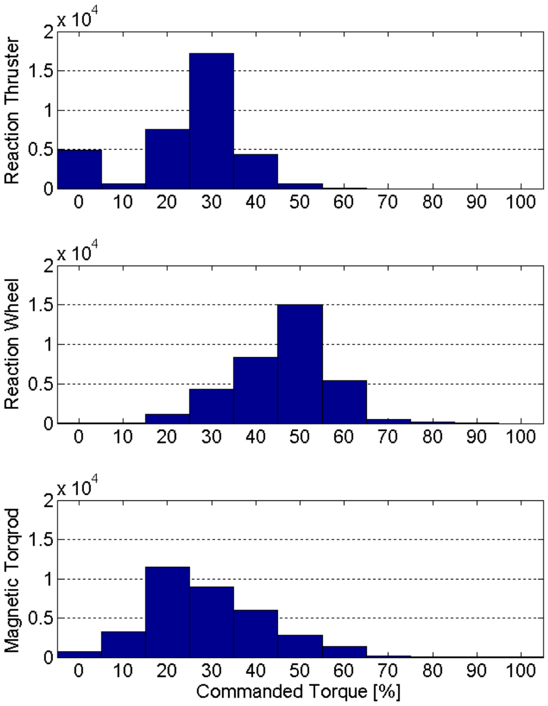

Figure 4.17 - Frequency of activation of each actuator.

that the RCS applied torque pulses of 0.25 Nm while the reaction wheel applied a maximum torque of 50 mNm at the beginning of the maneuver (see Figure 4.19), and the magnetic torqrod had a maximum torque level of 7 mNm (see Figure 4.20). Concerning to the latter actuator, note that there were some periods of saturation torque due to the limitation of the magnetic dipole moment and the magnitude and direction of the Earth's magnetic field. The noisy behavior is inherent from the actuator' nonlinearities.

Another important issue to be explored is the input commands of the actuators. As displayed in Figure 4.21, it is interesting to note the behavior of the input voltage (left) as well as the angular velocity of the reaction wheels (right). When the rotational motion is initialized, it occurs a brief period of saturation of the input voltage commanded to the reaction wheel which operate in Y_B axis. As a result of this input signal, the flywheel achieves the highest speed of almost 250 rpm in Y_B axis whereas lower velocities are achieved in the remaining axes. Likewise, a saturation period occurs with the electromagnetic dipole moments of the torqrods in axes X_B and Z_B, as shown in Figure 4.22. This data explains, due to the vector interaction among the geomagnetic field and the dipole moments (see Section 2.6.3), the highest torque level applied in Y_B axis.

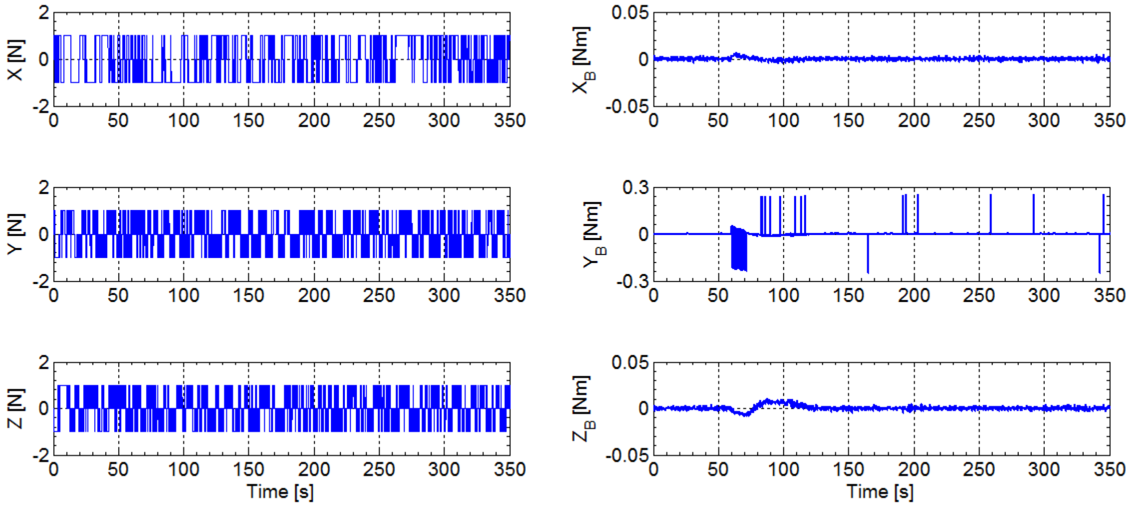

Figure 4.18 - Force pulses applied by the RCS (left) and total torque applied by reaction wheels, magnetic torqrods, and RCS (right).

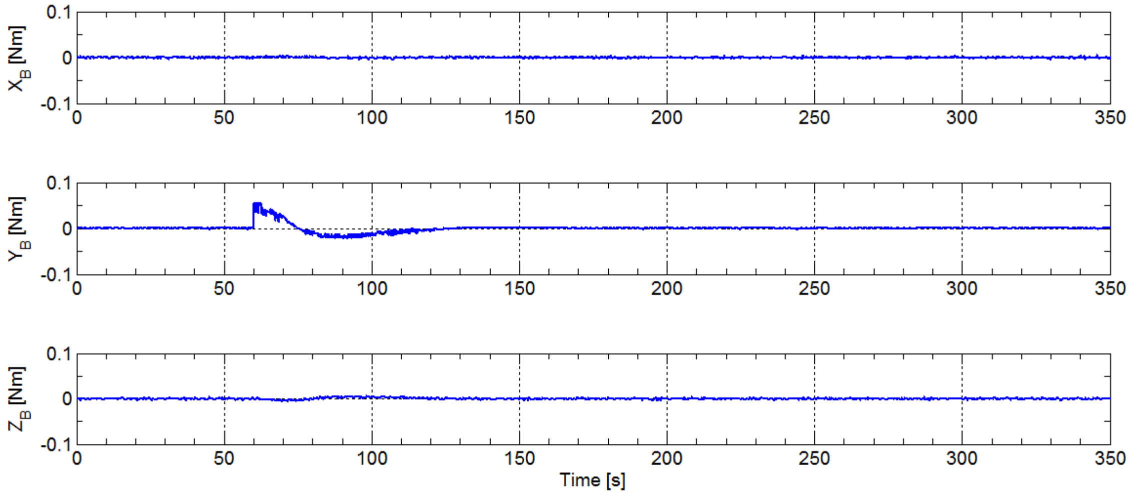

Figure 4.19 - Torque applied by the reaction wheels as a function of time.

It is worth also looking into the Figure 4.23 which shows the response curve presented by the propellant mass (left) and electric charge (right) consumptions. The propellant consumption curve has a quasi-linear behavior mainly because, although the application of torque pulses are sporadic, the application of thrust pulses to correct the translational motion is practically continuous. On the other hand, the electric charge consumption curve is quite different. Its behavior begins linear until starting the attitude maneuver where, from this point, occurs a meaningful increasing mainly due to the most active contribution of the reaction wheel. Then after achieving the steady state, the rate of consumption decreases again.

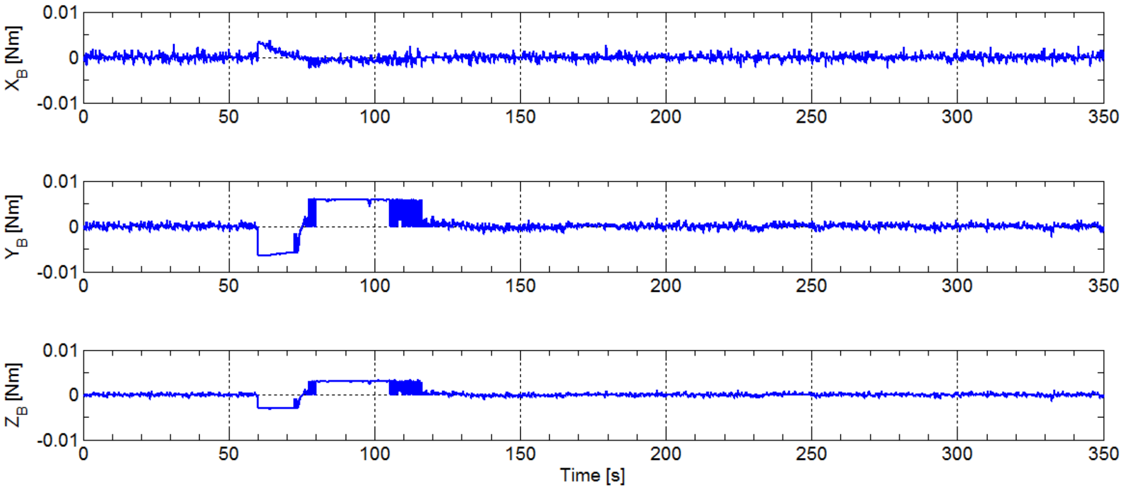

Figure 4.20 - Torque applied by the magnetic torqrods as a function of time.

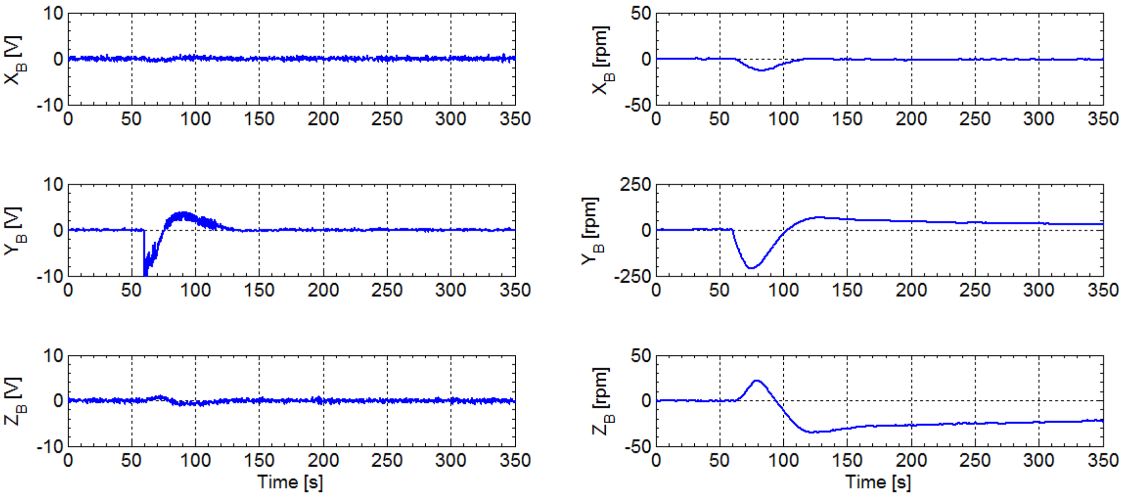

Figure 4.21 - Input voltage commands (left) and angular velocity (right) of the reaction wheels as a function of time.

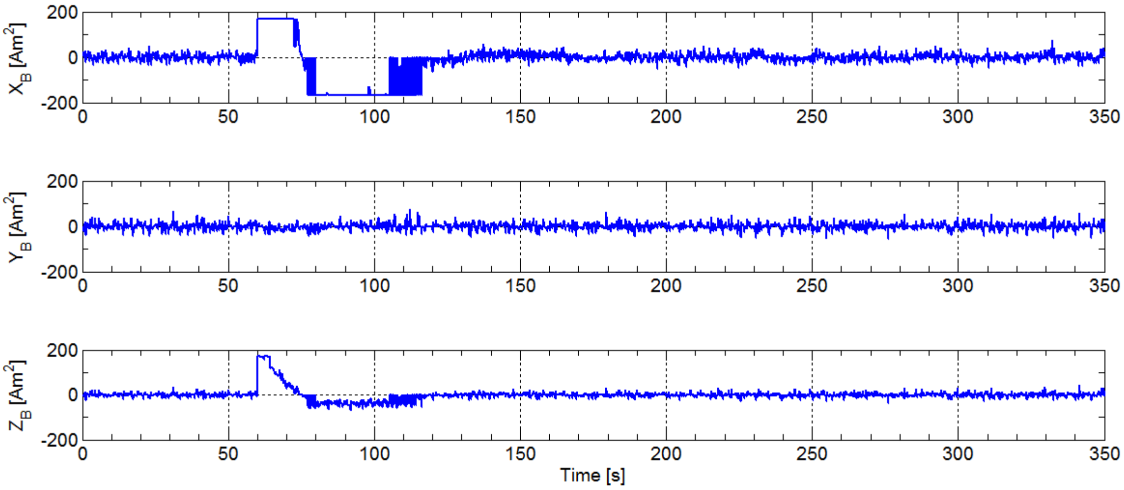

Figure 4.22 - Electromagnetic dipole moment commands of the magnetic torqrods as a function of time.

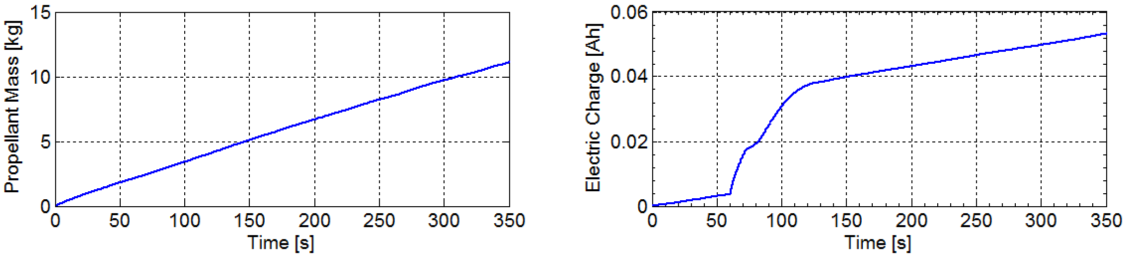

Figure 4.23 - Propellant mass (left) and electric charge (right) consumptions as a function of time.

5 AMCM-II: A SOLUTION TO THE REAL-TIME OPERATION PROBLEM OF SPACECRAFT THRUSTERS

A novel approach to solve the real-time operation problem of spacecraft thrusters, called **Actuator Multiobjective Command Method II** (AMCM-II), has been proposed in this chapter. The method, based on a discrete multiobjective optimization technique, selects at every control cycle the best combination of thrusters and their firing time duration which optimizes simultaneously a group of four conflicting objectives. AMCM-II has also been included in a coupled translational and attitude control system applied to the final approach rendezvous.

5.1 Actuator Multiobjective Command Method II

In this case, the discrete multiobjective optimization problem is formulated with four objectives functions: force error (Z_1), torque error (Z_2), propellant consumption (Z_3), and total number of pulses (Z_4). Such functions shall be minimized simultaneously and they compose the objective function vector, $\mathbf{Z}(\mathbf{x})$. The mathematical formulation of AMCM-II is expressed by

$$\begin{array}{lrcl} \text{Minimize} & \mathbf{Z}(\mathbf{x}) & = & [Z_1(\mathbf{x}), Z_2(\mathbf{x}), Z_3(\mathbf{x}), Z_4(\mathbf{x})]^T \\ & Z_1(\mathbf{x}) & = & \left\{\sum_{i=1}^{3} [F_i^a(\mathbf{x}) - F_i(\mathbf{x})]^2\right\}^{1/2} \\ & Z_2(\mathbf{x}) & = & \left\{\sum_{i=4}^{6} [T_i^a(\mathbf{x}) - T_i(\mathbf{x})]^2\right\}^{1/2} \\ & Z_3(\mathbf{x}) & = & \sum_{i=1}^{n} \frac{P_i(\mathbf{x})}{I_{fi}(\mathbf{x})\mu} \\ & Z_4(\mathbf{x}) & = & \sum_{i=1}^{n} t_i(\mathbf{x}) \\ \text{subject to} & \mathbf{x} & \in & \mathbf{X} \\ & \mathbf{x} & \geqslant & 0 \end{array} \tag{5.1}$$

where $\mathbf{x} \in \mathbb{R}^n$ represents the decision variable vector which physically corresponds to the feasible firing pulses duration of each thruster; $\mathbf{X} \in R^k$ (for $k \geq 1$) represents the discrete feasible set of decision variables provided by the TMF; and $\mathbf{F}^a = [F_1^a, F_2^a, F_3^a, T_4^a, T_5^a, T_6^a]^T \in R^6$ is the applied force and torque vector composed of three components of force and torque, respectively, achieved by evaluating

Equation 2.32 for the specific firing duration vector.

The first and second objective functions (Z_1 and Z_2) represent the difference between the requested and the applied force and torque commands, respectively. As discussed in Chapter 2, these errors are inherent from the random quantization and MIB evaluation processes. The third objective function (Z_3) represents the total amount of propellant mass consumed by all thrusters. The last objective function (Z_4) is a measure of the life cycle of the RCS. Since thrusters have a limited number of pulses defined by the manufacturer, then the RCS loses its full capability if at least one thruster achieves the end of the life cycle.

The third objective function (Z_3) defines the basic equation of propellant mass consumption (SUTTON; BIBLARZ, 2001) which varies according to the average force vector ($\mathbf{P} \in R^n$), the final specific impulse vector ($\mathbf{I}_f \in R^n$), and the Earth's gravitational constant (μ). Within a control cycle, the average force applied by each thruster is a linear function of the pulse length, such that

$$\mathbf{P} = F_n \frac{\mathbf{x}}{\Delta h_c} \tag{5.2}$$

where F_n is the nominal thrust and Δh_c is the interval of the control cycle. The specific impulse depends on the pulse length. As discussed previously, the specific impulse is significantly reduced when very short pulses are activated (SIDI, 1997). This behavior plays an important role during attitude control tasks. Therefore the final specific impulse parameter (I_f) can be defined as

$$I_f = \begin{cases} I_{sp} & \text{for} \quad x > \text{MIB} \\ I_{sp}/2 & \text{for} \quad x = \text{MIB} \end{cases} \tag{5.3}$$

The last objective function (Z_4) takes into account the maximum number of activations which the thruster can withstand. Although this technical specification can affect the satellite's serviceable life, it is typically quite large (hundreds of thousands) depending on the type and manufacturer of the thrusters. Hence the thruster activation (t) is given by

$$t = \begin{cases} 1 & \text{for} \quad x > 0 \\ 0 & \text{for} \quad x = 0 \end{cases} \tag{5.4}$$

Similarly AMCM-I, the proposed method AMCM-II evaluates the objective functions for all candidate solutions and selects the best compromise solution using the decision making method Smallest Loss Criterion (SLC), as defined in Chapter 2. The selected solution represents the best combination of thrusters and firing pulse duration to be commanded to the thrusters. The aforementioned process is illustrated in Figure 5.1.

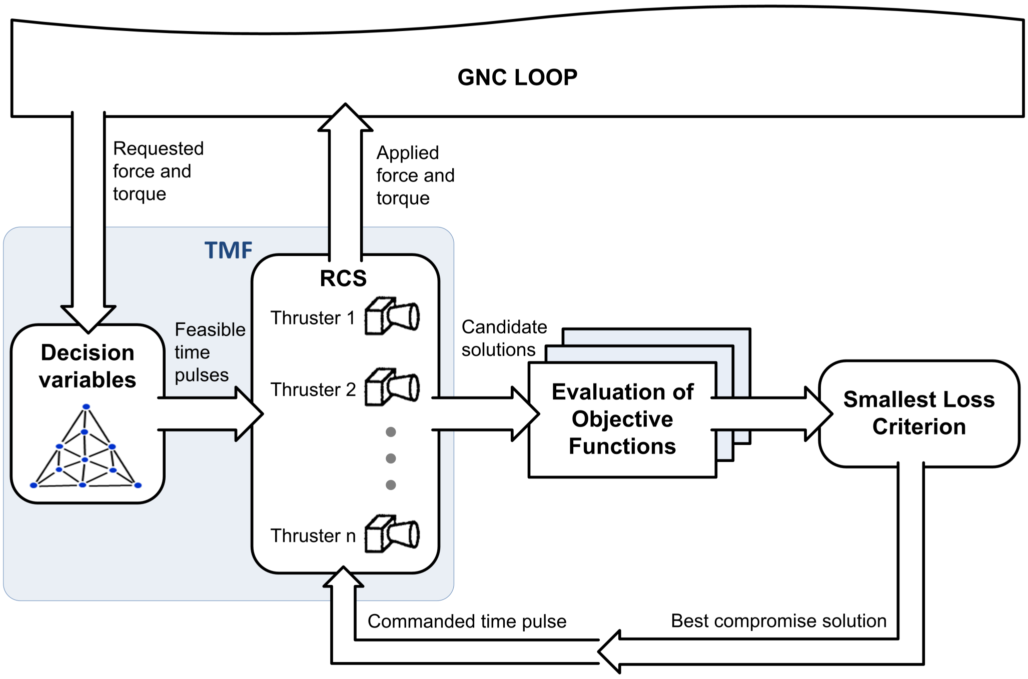
GNC LOOP
Requested force and torque
Applied force and torque
TMF
RCS
Thruster 1
Thruster 2
Thruster n
Decision variables
Feasible time pulses
Candidate solutions
Evaluation of Objective Functions
Smallest Loss Criterion
Commanded time pulse
Best compromise solution

Figure 5.1 - Functional concept of the Actuator Multiobjective Command Method II (AMCM-II).

Figure 5.2 presents the flowchart of the multiobjective optimization process of AMCM-II. As shown before, the first step is the loading of simulation parameters. Then, based on the force and torque signal requested by the PID controller, the thruster management function (TMF) computes all feasible time pulses which will compose the decision space, as explained in Chapter 2. However, if the RCS is not able to meet the requested force and torque vector (that is, the solution is a null vector), then the thrusters are kept off. But if so, then the objective functions are evaluated. If the decision space is composed of just one candidate solution, then surely there is no multiobjective optimization process and this solution is commanded to the thrusters. In case of more than one candidate solution, then the Pareto front can be generated through the sorting out of the non-dominated solutions; or all candidate solutions can be used. The step from the calculation of the maximum values until the identification of the best compromise solution were described earlier in the last chapters. Once defined such solution, then the thrusters are properly commanded.

5.2 RCS Configuration

In this case, the RCS is designed in order to provide a great number of candidate solutions. In addition, the thrusters configuration should be as similar as possible to that one used by rendezvous vehicles (like ATV). Therefore, a cubic body vehicle with a RCS composed of four groups of four one-sided thrusters ($n = 16$) is used. The locations and orientations of the thrusters are shown in Figure 5.3. It is assumed that the nozzles are inclined by an angle δ, in order to avoid thruster plume disturbances (FEHSE, 2003). In addition, it is assumed that all thrusters have the same distance from the CoM of the spacecraft. The computation of the force and torque components of the configuration matrix changes according to the nozzles inclination. It is worth mentioning that the objective here is not define an optimal design of thrusters, but for a given fixed set-up of thrusters, there shall be found out the best way to operate them. The elevation and azimuth angles, α and β, as well as the components of the vector distance of every thruster is presented in Table 5.1. These parameters, replaced in Equations 2.33 and 2.34, provide the configuration matrix of the RCS.

5.3 Purely Numerical Simulations

In order to test the proposed methodology, AMCM-II has been included in a coupled rendezvous and attitude control system and numerical simulations have been carried out. The orbit, satellite, sensors, and RCS parameters described in Table 4.2 are also used in this chapter. In addition, it is assumed a nozzle inclination of 15 degrees.

5.3.1 Control Cycle Analysis

Firstly, AMCM-II is analyzed for a single control cycle in order to evaluate the tradeoff among the objectives. Afterward, the multiobjective method is appraised in a complete rendezvous simulation. Value path representation (see explanation in

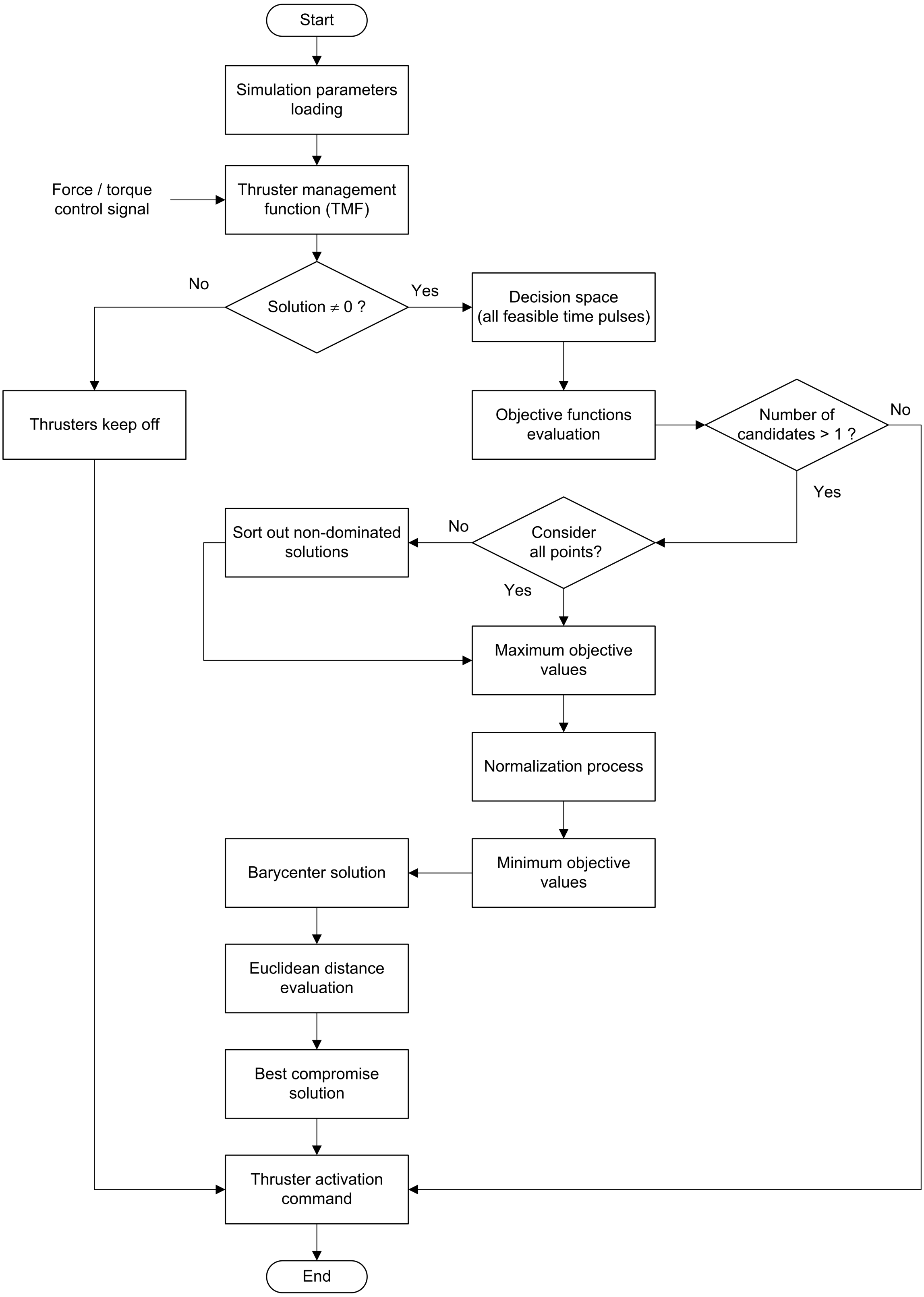
Start
Simulation parameters loading
Force / torque control signal
Thruster management function (TMF)
No
Solution ≠ 0 ?
Yes
Decision space (all feasible time pulses)
Thrusters keep off
Objective functions evaluation
Number of candidates > 1 ?
No
Yes
Sort out non-dominated solutions
No
Consider all points?
Yes
Maximum objective values
Normalization process
Barycenter solution
Minimum objective values
Euclidean distance evaluation
Best compromise solution
Thruster activation command
End

Figure 5.2 - Flowchart of the multiobjective optimization process of AMCM-II.

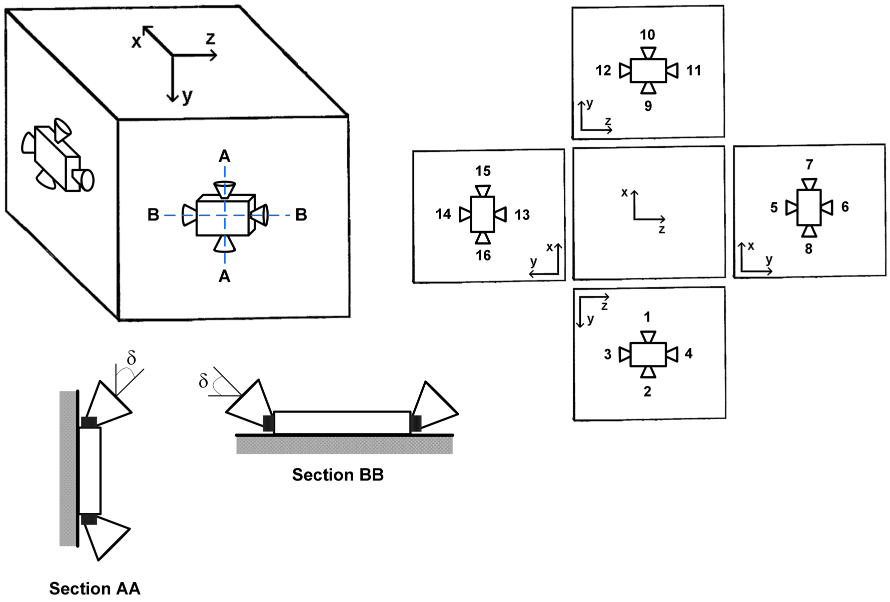

Figure 5.3 - Thrusters' location and orientation (n = 16).

Table 5.1 - RCS parameters for configuration with 16 thrusters.

Thruster	α	β	r_{bx}	r_{by}	r_{bz}
1	$90-\delta$	180	1	0	0
2	$\delta-90$	180	1	0	0
3	0	$90+\delta$	1	0	0
4	0	$-90-\delta$	1	0	0
5	$90-\delta$	-90	0	0	1
6	$\delta-90$	-90	0	0	1
7	0	$\delta-180$	0	0	1
8	0	$-\delta$	0	0	1
9	$90-\delta$	0	-1	0	0
10	$\delta-90$	0	-1	0	0
11	0	$90-\delta$	-1	0	0
12	0	$\delta-90$	-1	0	0
13	$90-\delta$	90	0	0	-1
14	$\delta-90$	90	0	0	-1
15	0	$180-\delta$	0	0	-1
16	0	δ	0	0	-1

Chapter 4) has been used to plot the objective space. Figure 5.4 shows the value path plot of AMCM-II for a particular requested force and torque vector: $\mathbf{F}$ = [-0.22 -0.83 0.06 0.14 -0.53 0.60]^T. In this case, all candidate solutions have been used to define the best compromise solution.

Unlike AMCM-I where all candidate solutions belonged to the Pareto front, here we have a different scenario. As can be confirmed in Figure 5.4, the necessary condition for the noninferiority, stated in Chapter 2, is not complied. For this specific control cycle, the method found 88 candidate solutions but only 12 are non-dominated solutions. One solution from the set of dominated solutions is highlighted in Figure 5.4 by a green dotted line. From 88 possible alternatives, AMCM-II selects the candidate number 33 as the best compromise solution. Considering only the 12 non-dominated solutions in the selecting process, as shown in Figure 5.5, then the candidate number 78 is selected.

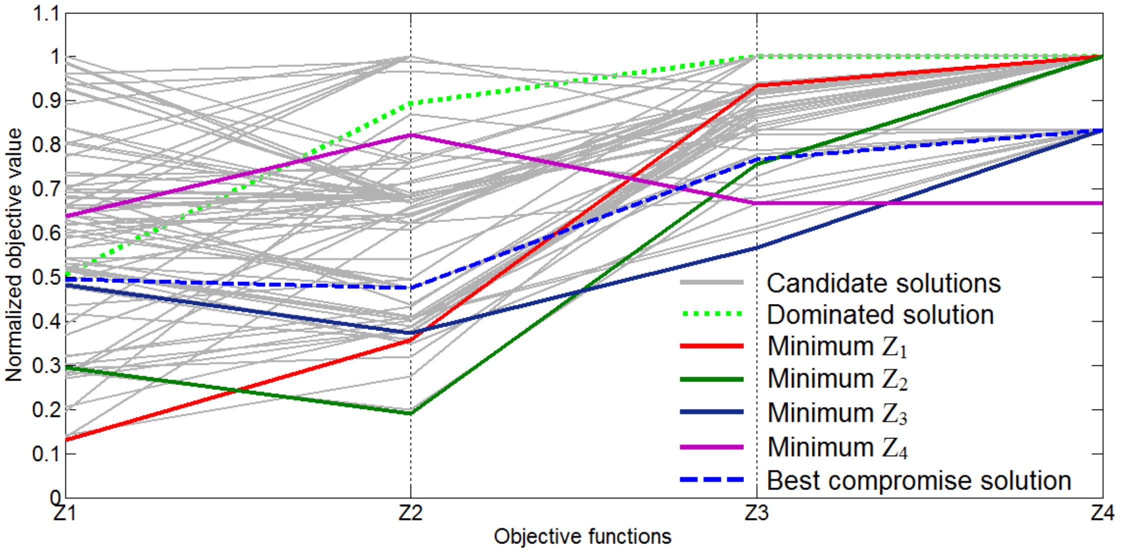

Figure 5.4 - Value path plot of AMCM-II using all candidate solutions.

The decision variable represents the firing pulse duration commanded to the thrusters. As addressed in Chapter 2, only a maximum combination of 6 thrusters per control cycle is activated in order to avoid the computational effort. Figure 5.6 shows the selected thrusters and the respective duration of the pulse activation of the best compromise solutions exhibited in Figures 5.4 and 5.5. The vertical axes describe the activation signal whereas the horizontal axes express the activation time. The time of 0.1 represents the length of the control cycle. Note that from 16 available thrusters, the method selected five thrusters in both approaches, but not the same ones, to meet the objective functions simultaneously.

Due to this difference, it makes sense to compare also the objective values of each approach: using all candidate solutions (SLC-A) and using only non-dominated so-

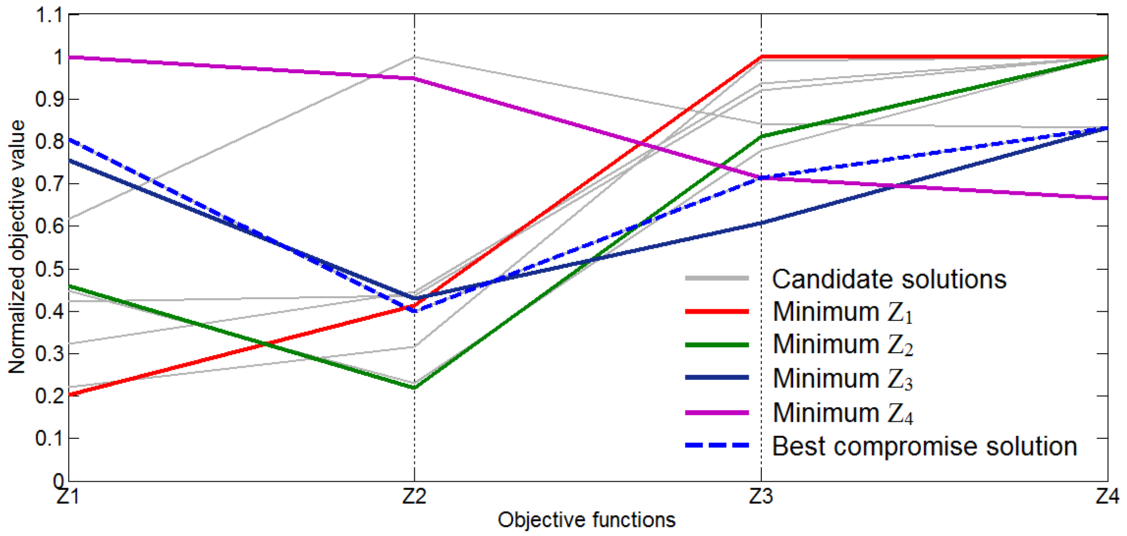

Figure 5.5 - Value path plot of AMCM-II using only non-dominated solutions.

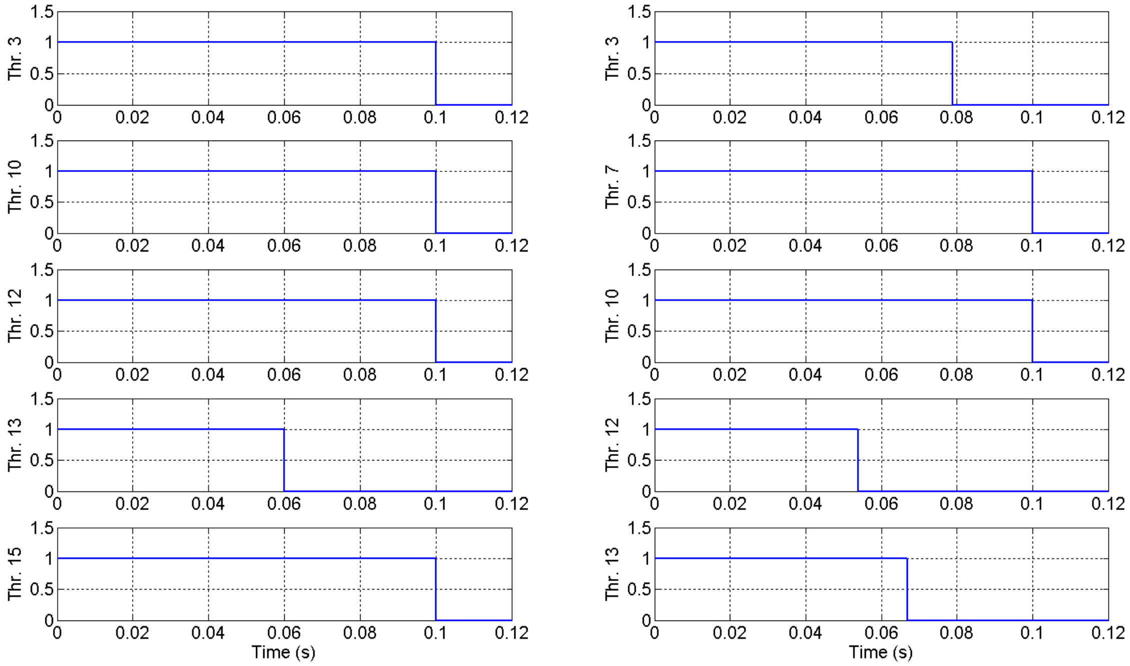

(a)

(b)

Figure 5.6 - Time pulse activation: (a) solution 33, approach using all candidate solutions; (b) solution 78, approach using only non-dominated solutions.

lutions (SLC-D). As can be seen in Figure 5.7, the approach SLC-D had lower values than SLC-A in two objectives: torque error (Z_2), Figure 5.7(b), and propellant consumption (Z_3), Figure 5.7(c). The force error (Z_1), Figure 5.7(a), presented by the first approach, SLC-A, was slightly lower than SLC-D. As already discussed, both approaches presented the same number of pulses (Z_4) in this case, Figure 5.7(d).

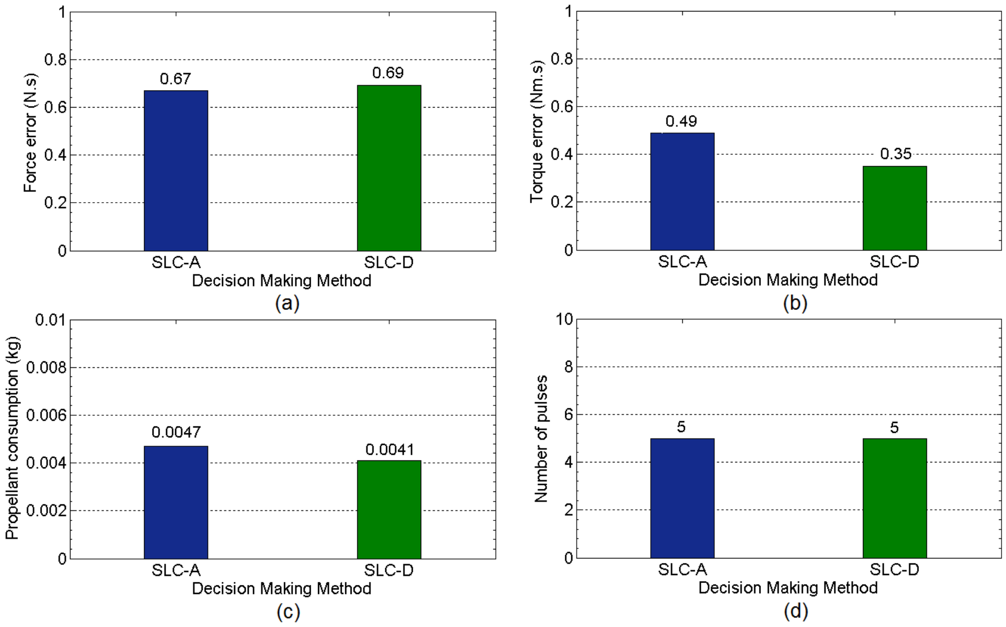

Figure 5.7 - Objective values for a single control cycle: (a) force error; (b) torque error; (c) propellant consumption; and (d) number of pulses.

5.3.2 Complete Rendezvous and Attitude Simulation using AMCM-II

Hereafter results from a complete final approach rendezvous are presented. Thereupon the number of candidate solutions as well as the number of non-dominated solutions change at every control cycle generating different shapes of value path plot. The number of solutions as a function of time for the initial period of simulation is shown in Figure 5.8. The set of non-dominated solutions represent approximately 25% of the complete set of solutions.

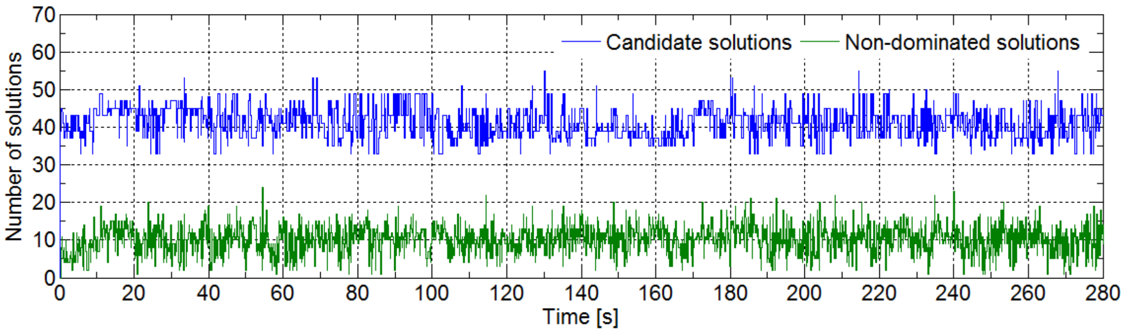

Figure 5.8 - Number of candidates and non-dominated solutions as a function of time.

The approach maneuver is carried out from 20 m to 15 m along the V-bar axis and an initial angular error - difference between the actual attitude and the guidance value - of 10 degrees in the Y_B axis is corrected. Here the method SLC-D has been used. The time translational and angular response of the final approach rendezvous simulation is depicted in Figure 5.9. The time approach response is shown on the left side whereas on the right side is presented the angular response plot. Three types of output are presented for the approach motion: the dynamics (real), the measured by the sensor, and the estimated by the filter. Concerning the angular response, although there is a small oscillation along the set point, the GNC loop, composed of AMCM-II, was able to mitigate the state error and to achieve stability conditions.

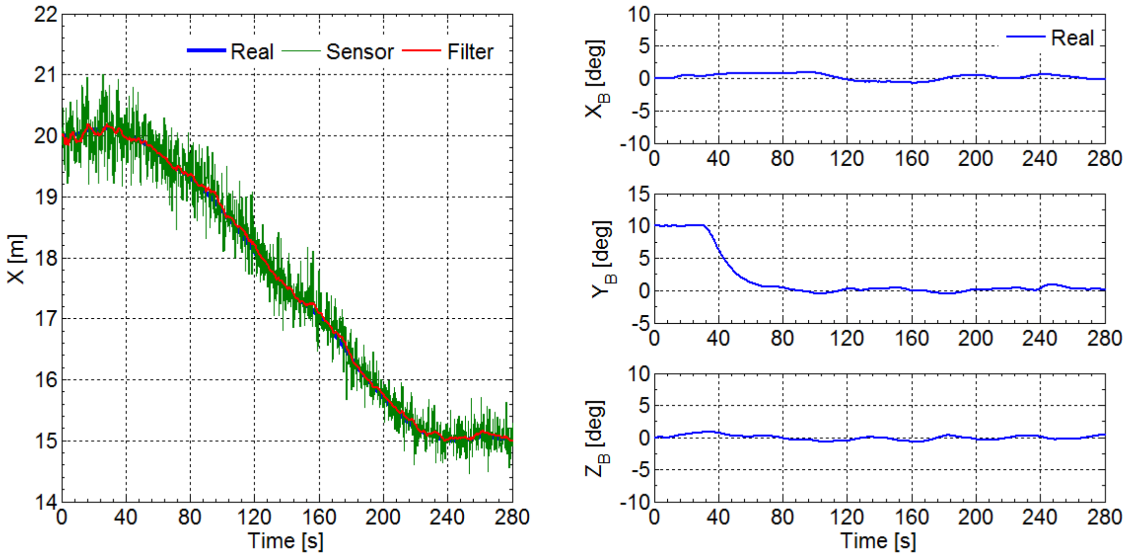

Figure 5.9 - Time translational (left) and angular response (right) of the final approach rendezvous.

Figure 5.10 depicts the GNC loop error which is a measure of the performance of the control system. Four types of translation errors have been presented: sensor minus real state and filter minus real state on the left side, and guidance minus real state and guidance minus filter on the right side. As can be noted, the entire GNC loop using a RCS of 16 thrusters commanded by AMCM-II was able to keep the loop errors within a acceptable range.

The force and torque pulses applied by the RCS are presented in Figure 5.11. The amplitude of the force level (left side) is modulated until about 1.5 N whereas the torque level (right side) can achieve a maximum of approximately 0.5 Nm. In order to have a better visualization of the thrust pulses behavior, the same plot is exhibited

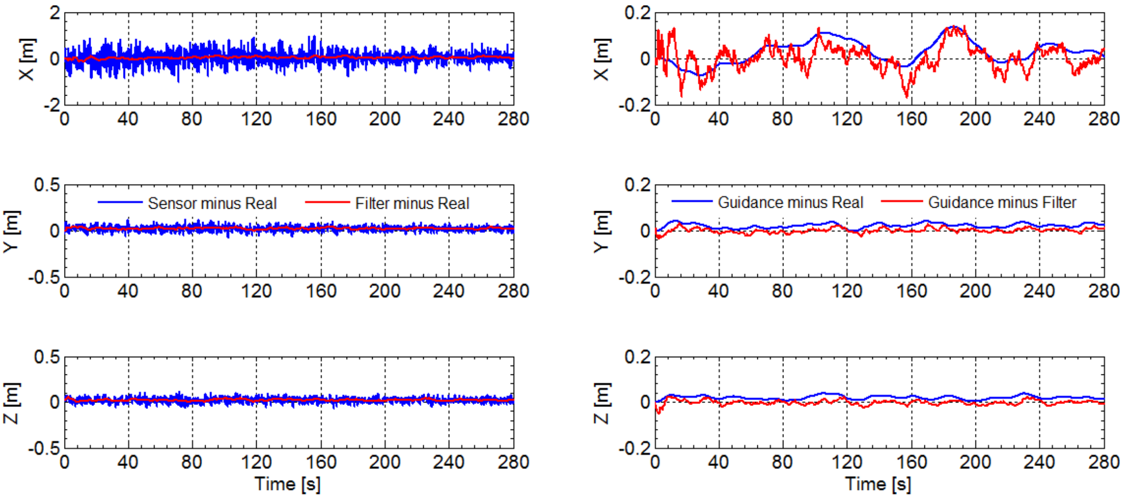

Figure 5.10 - AMCM-II: GNC loop errors including the real position (left) and the guidance position (right).

for a brief period from 35 s to 38 s (Figure 5.12). This period represents the beginning of the attitude maneuver. Note that there is a modulation of the pulse width as well as the pulse frequency.

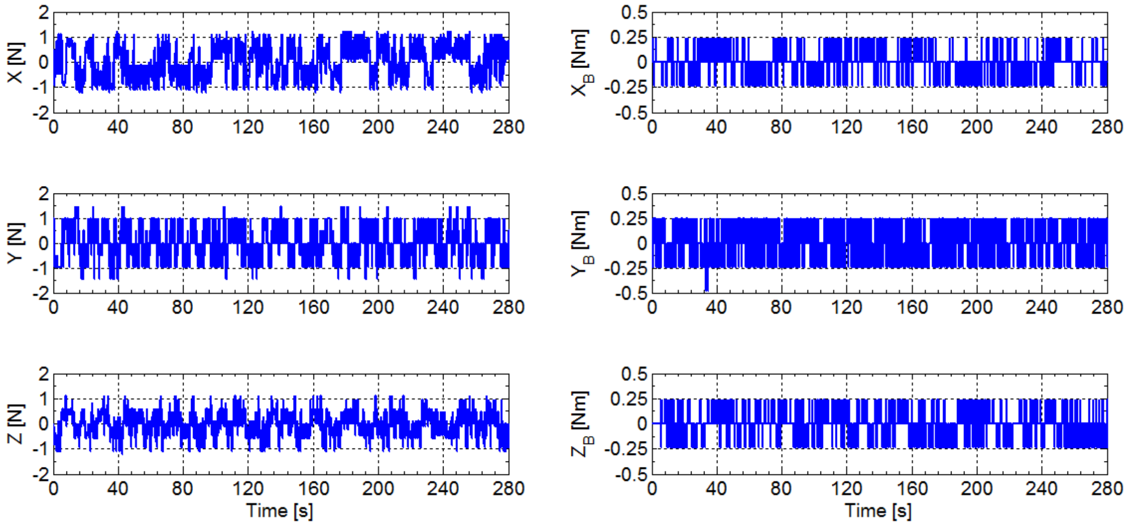

Figure 5.11 - Force (left) and torque (right) pulses applied by the RCS of 16 thrusters.

The SLC has been compared to a different decision making method: the Weighted Sum Method (WSM), as defined in Chapter 2. Figure 5.13 shows the objective values accumulated throughout the simulation. As before, the SLC is evaluated in two cases for selecting the best compromise solution: using all candidate solutions

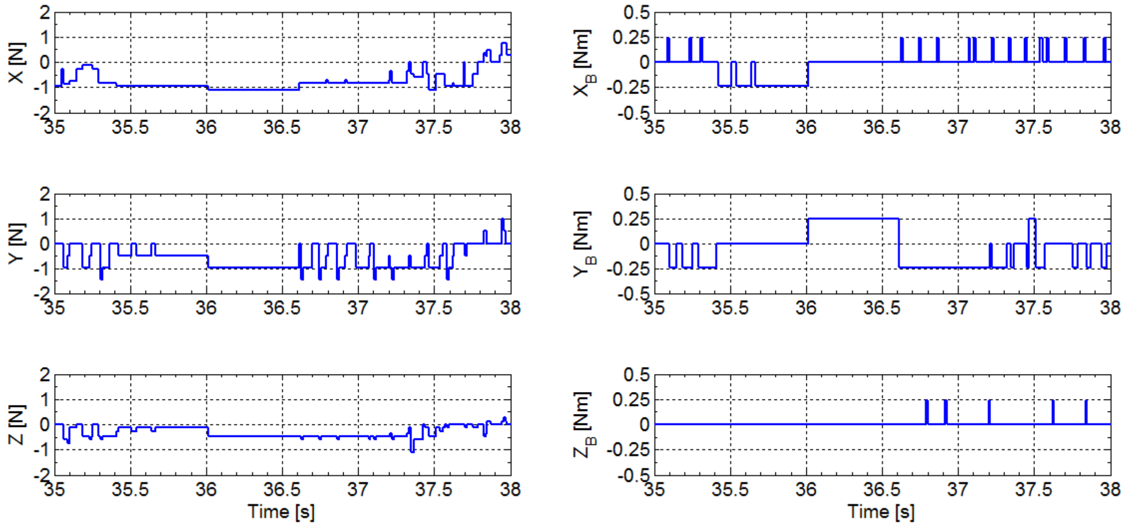

Figure 5.12 - Force (left) and torque (right) pulses, applied by the RCS of 16 thrusters, of a brief period of simulation.

(SLC-A) and using only non-dominated solutions (SLC-D). The WSM is evaluated in four different approaches: WSM-1 optimizes only the first objective (Z_1); WSM-2 optimizes only the second objective (Z_2); and so on. Concerning the SLC methods, the results provided by the method SLC-D presented, as expected, a better result: an average reduction of 7% compared to the method SLC-A. The most used optimization criterion of the thruster operation problem is the optimization of the propellant consumption (Z_3). Then comparing the WSM-3 with the SLC-D, we can note that the former presented results 37% and 46% higher, for the first and second objectives respectively (Figures 5.13(a) and (b)), than the latter method. However, for the third and fourth objectives (Figures 5.13(c) and (d)) , WSM-3 had values of just 9% and 5%, respectively, lower than SLC-D. It is worth mentioning that the decision making method SLC-D did not have the lowest nor the highest value in any objective, as stated by the concept of the method, but equilibrium solutions. This behavior can also be seen through the performance overall mean presented in Table 5.2.

In this case, the multiobjective approach SLC-D presented a result ($\bar{\eta} = 0.72$) quite close to the lowest alternative WSM-1 ($\bar{\eta} = 0.70$). If we analyze these numbers strictly, we can see that WSM-1 achieved a force error 41% lower than SLC-D, because this is the goal of WSM-1, but generated a torque error 32% higher than the same method. While in the other objectives, they kept the same average. This fact explains the slight advantage over the multiobjective method. Of course, it is

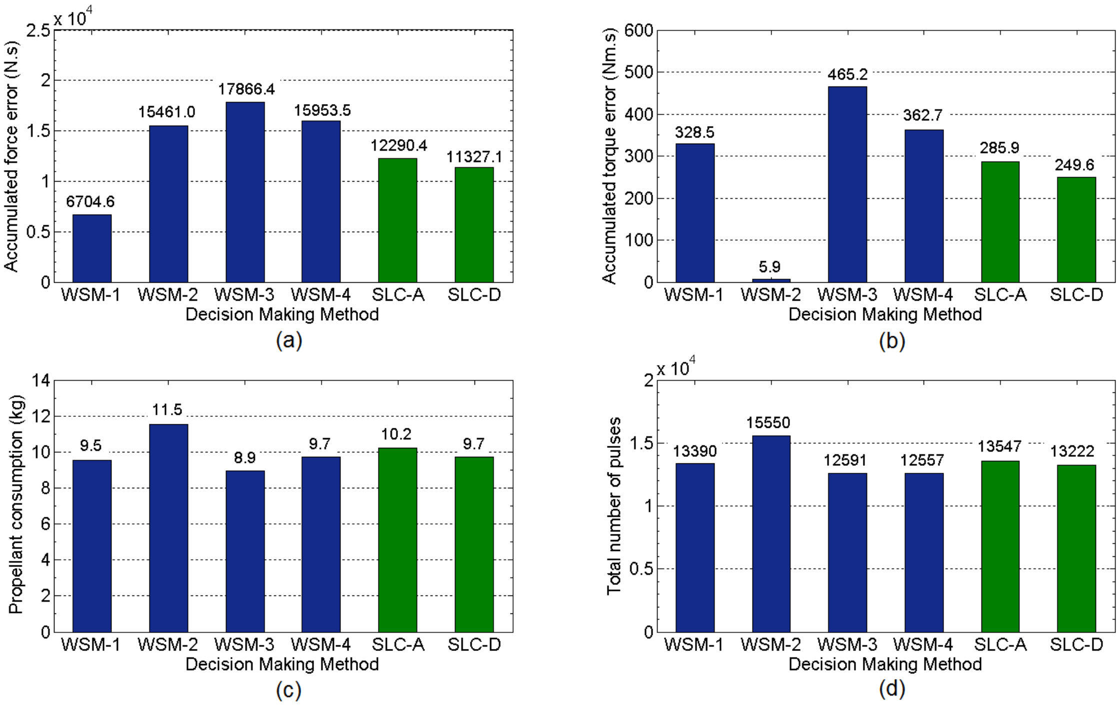

Figure 5.13 - Accumulated objective values throughout the simulation: (a) force error; (b) torque error; (c) propellant consumption; and (d) number of pulses.

Table 5.2 - Performance overall mean analysis of the thrusters operation problem.

Decision making	z_1	z_2	z_3	z_4	$\bar{\eta}$
WSM-1	0.38	0.71	0.83	0.86	**0.70**
WSM-2	0.87	0.01	1.00	1.00	0.72
WSM-3	1.00	1.00	0.77	0.81	0.90
WSM-4	0.89	0.78	0.84	0.81	0.83
SLC-A	0.69	0.61	0.89	0.87	0.77
SLC-D	0.63	0.54	0.84	0.85	**0.72**

not possible to overcome the results provided by a single optimization method. But, if we rule out the optimal result of each objective. Then SLC-D becomes a potential winner of the game.

5.3.3 Thruster Design Analysis

As mentioned earlier, the purpose of this thesis is not to find an optimal configuration of RCS. The set-up of thrusters used in this thesis (see Figure 5.3) has been defined in order to control the translational and rotational motions and to provide several alternatives of time pulse durations. However, during the tests, we realized that the thrust level and the nozzle inclination parameters have affected the performance of the control system. Then an analysis of the objective values as a function of these parameters has been performed, as shown in Figure 5.14.

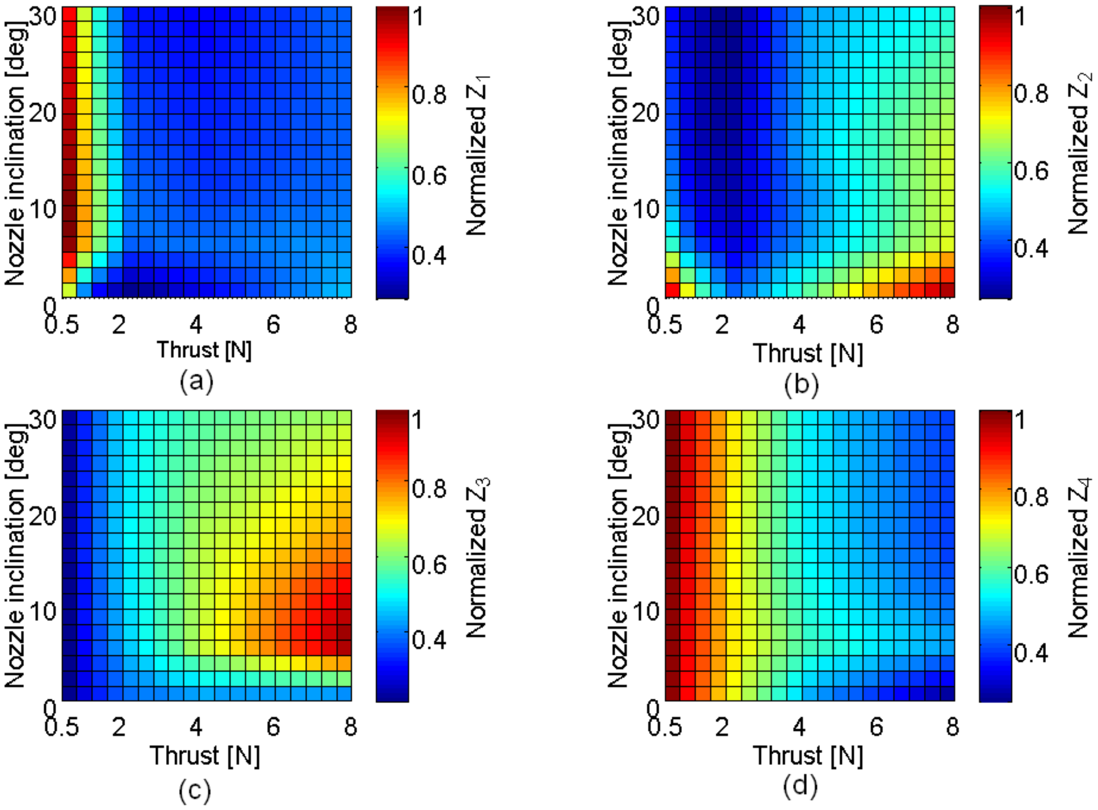

Figure 5.14 - Objective values as a function of thrust level and nozzle inclination parameters: (a) force error (Z_1); (b) torque error (Z_2); (c) propellant consumption (Z_3); and (d) number of pulses (Z_4).

The contour plots, presented in Figure 5.14, project a three-dimensional surface onto a two-dimensional plane. The vertical axes express the nozzle inclination (in degrees) whereas the thrust level (in N) is represented in the horizontal axes. The normalized scale of objective values lies on the right side of the plot. The objective functions have been considered the same as earlier: force error (Figure 5.14(a)), torque error (Figure 5.14(b)), propellant consumption (Figure 5.14(c)), and number of pulses (Figure 5.14(d)).

Each square point on the plots represents a complete rendezvous and attitude simulation using AMCM-II to command the thrusters, as presented in Section 5.3.2, assuming a given combination of nozzle inclination and thrust level. As can be noted, the properly selection of such parameters is a multiobjective optimization problem by itself. Small values of thrust level decrease the torque error but provide a higher level of force error. Likewise, fewer number of pulses can be achieved with a small nozzle inclination and a high thrust level, however this design would increase the propellant consumption. Although out of the scope of this thesis, this brief analysis evidences that the design of the RCS plays an important role in the performance of the spacecraft control system. Such optimization problem can be addressed as a future work.

5.3.4 A Thruster Failure Case

Here, the proposed method AMCM-II has been analyzed in a thruster failure scenario. Four different cases have been compared in this section. Three parameters are assumed: frequency of failure, duration of failure, and range of faulty thrusters. Such scenario is established as follows: during the period of failure, one thruster fails randomly at every control cycle. Table 5.3 describes the failure cases as well as the assumed parameters.

Table 5.3 - Thrusters failure case's parameters.

Case	Failure frequency	Failure duration (s)	Range of faulty thrusters
Case f1	20	5	1-16
Case f2	20	10	1-16
Case f3	20	15	1-16
Case f4	20	10	1-8

For instance, the Case f1 assumes that a fail will occur in a given thruster - selected randomly from the range of 1-16 (see Figure 5.3) - at every control cycle for a period of 5 s. This period of failure happens at every 20 s. Cases f2 and f3 consider different duration of failures whereas Case f4 assumes that only thrusters from the range 1-8 can fail. Figure 5.15 illustrates graphically the failure scenario of the Case f1. The failure signal, shown in Figure 5.15(a), means that one thruster has failed, every time the signal has reached the level one, with the frequency and duration specified in Table 5.3. Figure 5.15(b) shows the faulty thrusters for each control cycle. Such thrusters fail randomly during the failure period.

A complete rendezvous and attitude simulation has been executed and AMCM-II has commanded the RCS as before. However, in this case, AMCM-II shall take into

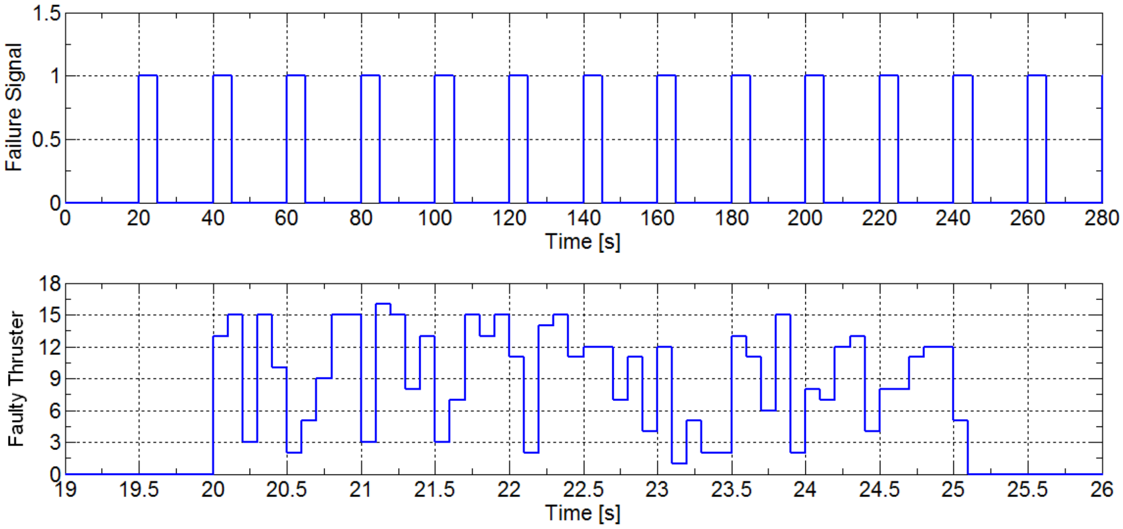

Figure 5.15 - Failure scenario of the Case f1: (a) failure signal; (b) faulty thrusters.

account the faulty thruster selecting the best compromise solution from all available candidate solutions. It is assumed that exists an identification system of failures which informs the faulty thruster to the AMCM-II. The approach motion and time angular response have been evaluated for each case in Figure 5.16. The guidance profile has also been plotted for assisting the comparison. As can be seen, AMCM-II was able to command the RCS during the maneuver. The approach and rotational motions were properly carried out in all situations. Moreover, all cases presented very close responses.

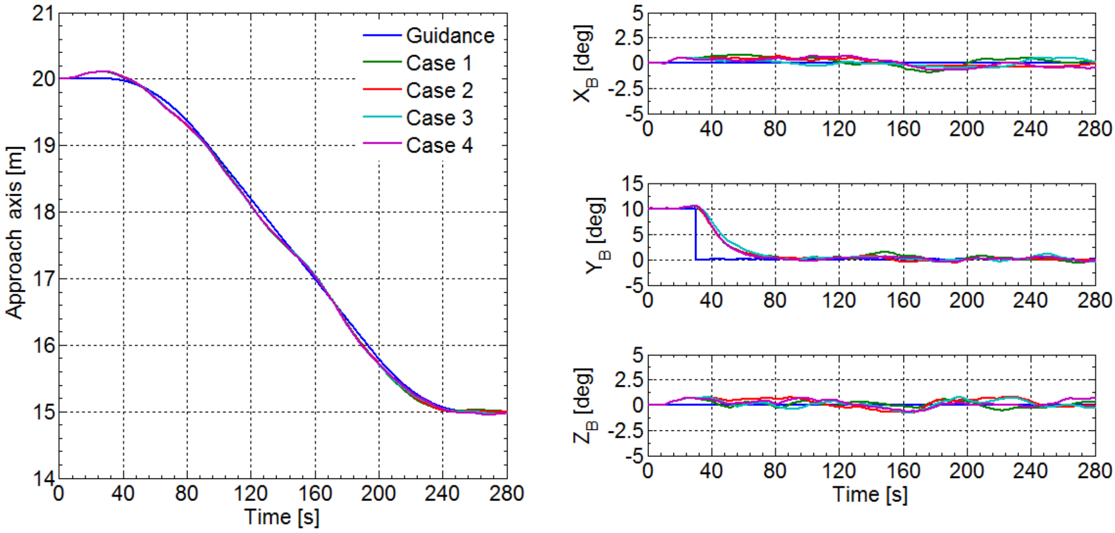

Figure 5.16 - Approach motion (left) and time angular response (right) for every failure cases.

The objective values, as defined at the beginning of this chapter, have been compared to the case without failures (SLC-D) in Figure 5.17. In general, AMCM-II kept the same level of the SLC-D. Even a small reduction can be noted in some objectives with exception of the torque error, presented in Figure 5.17(b), where occurred a small increase. In summary, this analysis evidences that AMCM-II is capable of working even in a failure scenario as considered here.

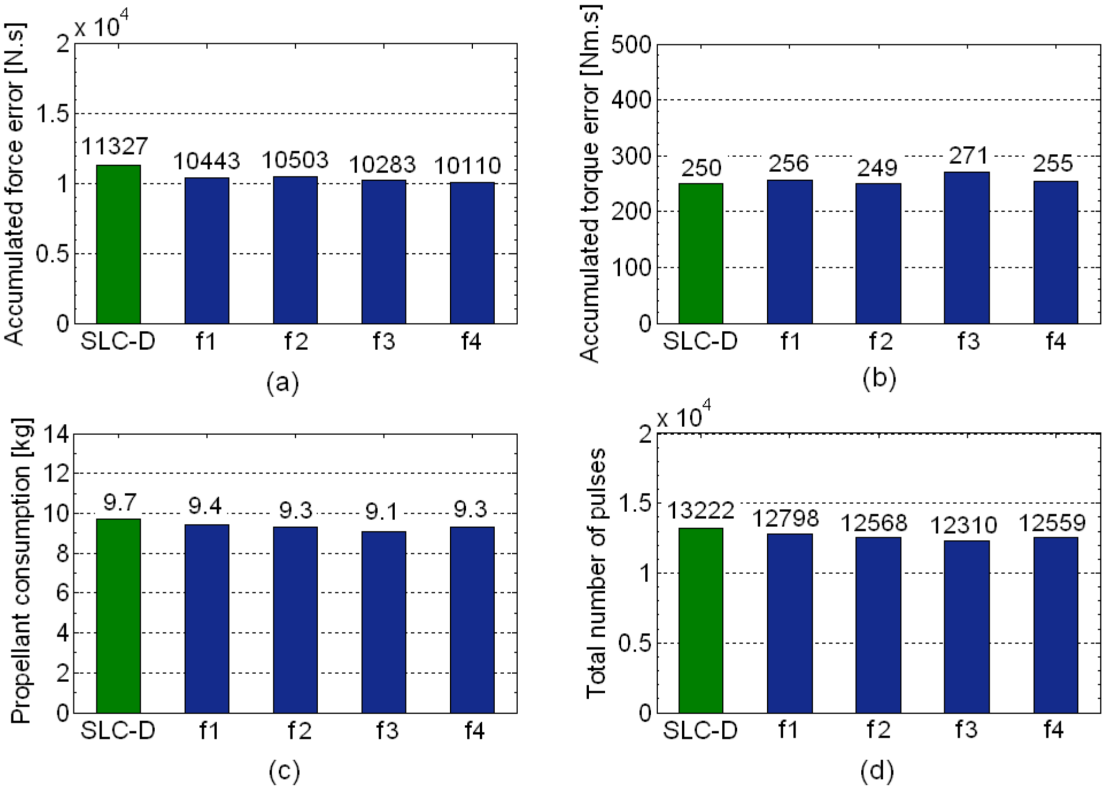

Figure 5.17 - Objective values of the failure scenario: (a) accumulated force error; (b) accumulated torque error; (c) propellant consumption; and (d) total number of pulses.

6 VALIDATION TESTS AT EPOS FACILITY

Chapter 4 and 5 have validated the multiobjective optimization approach through the comparison to different optimization criteria based on purely numerical simulations. The simulations carried out here are very similar to that ones presented at the last two chapters. The main difference is the utilization of a real visual camera sensor in a closed-loop control system instead of the pinhole camera model used before. Due to the similarity of results, plots concerning the multiobjective optimization are not presented again. This chapter focuses on the results of the approach and attitude maneuver which have been executed in a real-time environment. Integration, test and verification of the proposed methods have been made at the hardware-in-the-loop (HIL) rendezvous simulator, called European Proximity Operations Simulator (EPOS), located at the German Aerospace Center (*Deutsches Zentrum für Luft- und Raumfahrt* - DLR) in Oberpfaffenhofen/Germany.

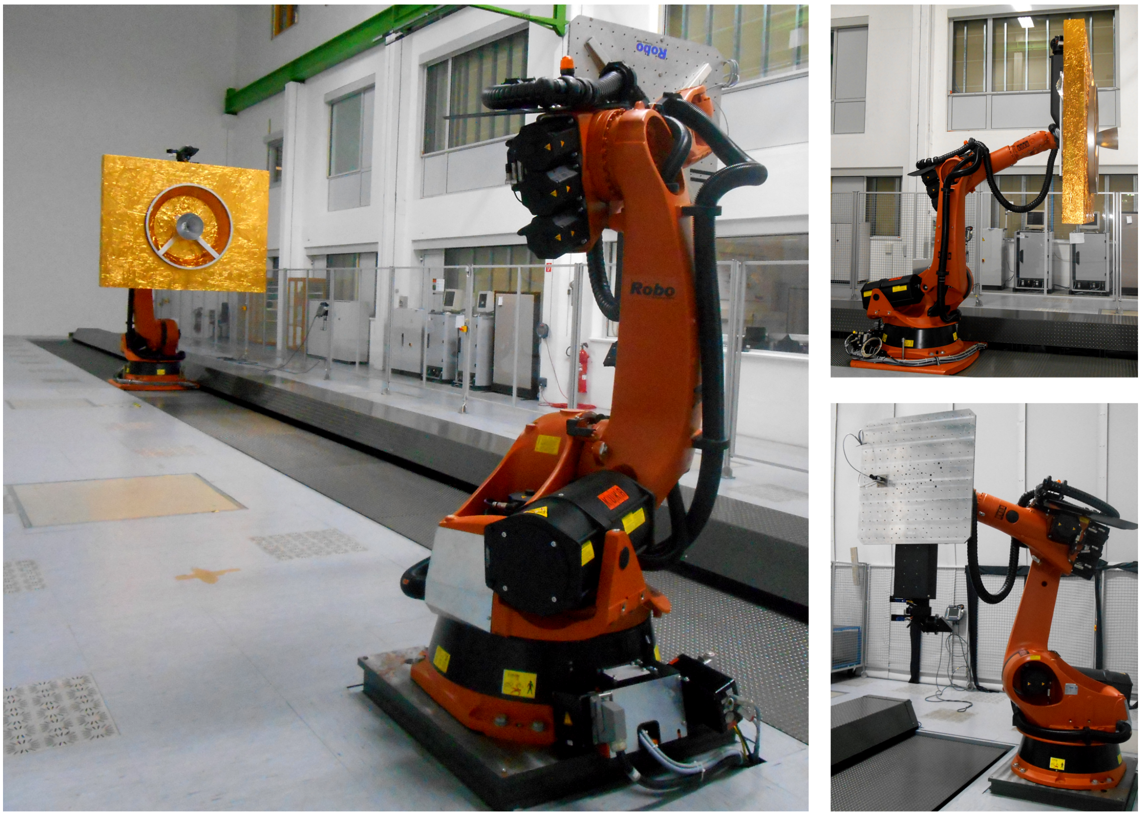

Figure 6.1 - The robots of the European Proximity Operations Simulator (EPOS).

6.1 About EPOS 2.0

The first version of EPOS was intensively used for testing the ATV RvD sensors and systems and also used for testing the sensors of the Japanese H-II Transfer Vehicle (HTV). In order to improve the test and simulation capabilities, a new EPOS system, called EPOS 2.0, was build in 2009. The new EPOS facility provides test and verification capabilities for the complete translational and rotational motions of two docking satellites, specially tests for on-orbit servicing missions [1]. EPOS includes two industrial robots (separation ranging from 25 m to 0 m) which are used for utmost realistic simulation of the real rendezvous and docking process (see Figure 6.1). Simulations of sunlight illumination conditions can also be used in this assembly. This test bed is able to simulate the last critical phase of the approach process including the contact dynamics simulation of the docking process.

As shown in Figure 6.2, the new facility includes the following components:

- A rail system mounted on the floor to move an industrial robot up to a distance of 25 m;
- A KUKA KR100HA robot (called Robot 1) mounted on the rail system for simulating the 6 degree of freedom of one spacecraft;
- A KUKA KR240 robot (called Robot 2) mounted at the end of the rail system for simulating the 6 degree of freedom of the second spacecraft;
- A PC-based monitoring and control system to monitor and control the RvD simulation on the facility.

6.1.1 Control concept

The entire EPOS control system can be divided into three levels (see Figure 6.3):

a) **Local Robot Control** (LRC) where each robot is independently controlled in real-time by its own LRC unit. Both standard industrial robot control cabinet in EPOS facility are equipped to be externally commanded with 250 Hz command rate.

---

[1] In an on-orbit servicing (OOS) mission, a service spacecraft approaches a target object. Then it performs various service tasks like the takeover of its orbit and attitude control, refueling or removing an inoperative satellite at the end of its lifetime.

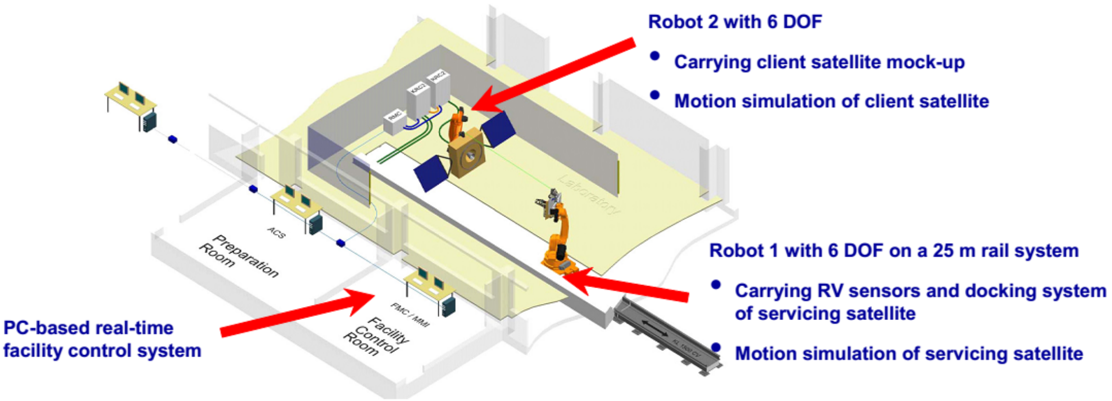
Robot 2 with 6 DOF
Carrying client satellite mock-up
Motion simulation of client satellite
Laboratory
Robot 1 with 6 DOF on a 25 m rail system
Carrying RV sensors and docking system of servicing satellite
Motion simulation of servicing satellite
ACS
Preparation Room
FMC / MMI
Facility Control Room
PC-based real-time facility control system

Figure 6.2 - Components of EPOS system.
Source: Adapted from Boge et al. (2011).

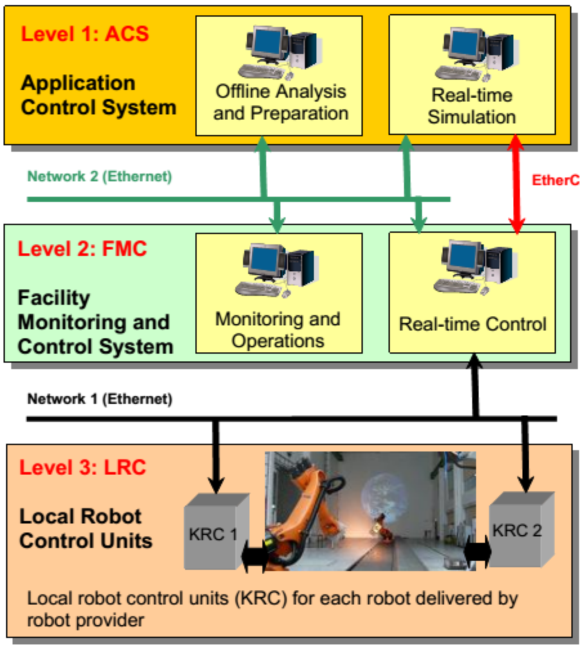
Level 1: ACS
Application Control System
Offline Analysis and Preparation
Real-time Simulation
Network 2 (Ethernet)
EtherCAT
Level 2: FMC
Facility Monitoring and Control System
Monitoring and Operations
Real-time Control
Network 1 (Ethernet)
Level 3: LRC
Local Robot Control Units
KRC 1
KRC 2
Local robot control units (KRC) for each robot delivered by robot provider

Figure 6.3 - Concept of the EPOS control system.
Source: Boge et al. (2011).

b) **Facility Monitoring and Control** system (FMC) where the entire facility is controlled and monitored in real-time. The FMC level allows the following tasks: operator's monitoring action over all the parameters and states of the facility; logging of all parameters and states of the facility, including external synchronization signals; real-time control of the entire facility including synchronization of all motion devices and kinematical conversions of the external commands; and choice among different interfaces.

c) **Application Control System** (ACS) where the actual RvD simulation is running. In particular, the models of the satellites dynamics and the case-specific scenarios can be implemented in a MATLAB/Simulink® environment. This means that the whole software related part of the simulation can exploit a model-based design approach. According to it, MATLAB/Real-Time Workshop® can be used to accomplish the automatic code generation. Subsequently the real-time executable is downloaded to a target platform running under the VxWorks® operating system. Via EtherCAT this real-time PC can communicate with the FMC system. The desired motion commands must be sent every 4 ms to the facility, as requested by the LRC units.

The EPOS control room (Figure 6.4), comprised by the FMC and ACS computers, is the place where the complete HIL RvD simulation is prepared, monitored, and its results can be logged.

Figure 6.4 - EPOS control room.

6.1.2 Capabilities and performances

The EPOS motion capabilities and performances (maximum values) are summarized in Table 6.1 (BOGE, 2011).

Table 6.1 - EPOS motion capabilities.

Parameter	Robot 1		Robot 2	
X axis, m	-2.6	24.5	-2.6	2.6
Y axis, m	-2.5	2.5	-1.2	4.0
Z axis, m	-0.6	1.2	-0.5	1.5
Roll angle, deg	-300	300	-300	300
Pitch angle, deg	-90	90	-90	90
Yaw angle, deg	-90	90	-90	90
Translational velocity, m/s	2		2	
Rotational velocity, deg/s	180		180	
Translational acceleration, m/s^2	2.3		2.3	
Rotational acceleration, deg/s^2	100		100	
Translational position accuracy (3σ), mm	<2		<2	
Rotational position accuracy (3σ), deg	<0.2		<0.2	
Payload, kg	60		200	
Command rate, Hz	250		250	

6.1.3 Facility simulation methods

This facility allows a hybrid simulation method where one part of the motion simulation is performed by numerical computations while the other part is executed by robots. These robots generate a physical representation of the numerical calculated trajectory. There are four methods to use EPOS facility:

1. Open-loop rendezvous simulation: this is the simplest way to use the test bed. In this option, the robots follow a predefined trajectory which is uploaded and executed by EPOS FMC system.

2. Closed-loop rendezvous simulation: inputs and outputs of an embedded system are connected to EPOS that simulates the real environment of the system. The rendezvous sensors are mounted on one robot and a typical satellite mock-up of the client satellite is mounted on the other robot. These navigation sensors measure the relative position and attitude of the target satellite with respect to the chaser satellite. Based on this measurement the computed positions and attitudes are commanded to the facility, as shown in Figure 6.5.

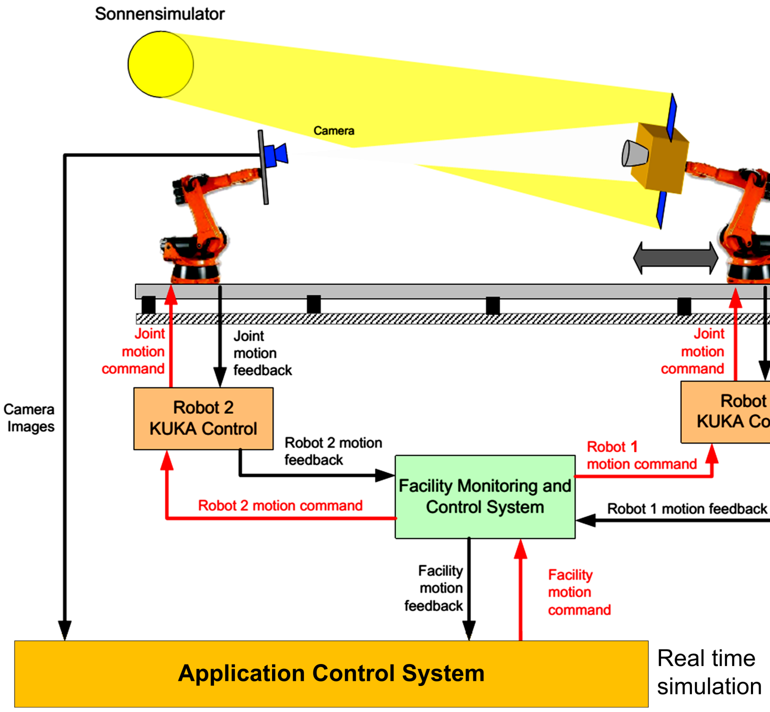
Sonnensimulator
Camera
Camera Images
Joint motion command
Joint motion feedback
Joint motion command
Joint motion feedback
Robot 2 KUKA Control
Robot 1 KUKA Control
Robot 2 motion feedback
Robot 1 motion command
Facility Monitoring and Control System
Robot 2 motion command
Robot 1 motion feedback
Facility motion feedback
Facility motion command
Application Control System
Real time simulation

Figure 6.5 - Set-up of EPOS in closed-loop control system.
Source: Adapted from Boge et al. (2011).

3. Contact dynamic simulation: the goal of this simulation system is to emulate the dynamic motion of two satellites while using the real docking hardware or its mock-ups to generate the contact force-moment and use these values as the input to the satellite simulation system in order to simulate the satellites' docking behavior (see Figure 6.6).

4. Sensor tests for lander applications: to use the test bed for lander applications was not a primary requirement for the EPOS design but such scenario can be simulated on EPOS, as illustrated in Figure 6.7. The sensor system is mounted on the Robot 1 whereas a representative surface model of the planet, moon or asteroid is mounted at the wall. The lander tests can be performed in open-loop as well in closed-loop.

6.1.4 EPOS coordinate systems

The EPOS simulator can be commanded using several reference coordinate systems. A brief description about each reference frame is given below (BOGE, 2011).

Ideal Robot Joint Coordinate (IJT): each robot has six independent servo con-

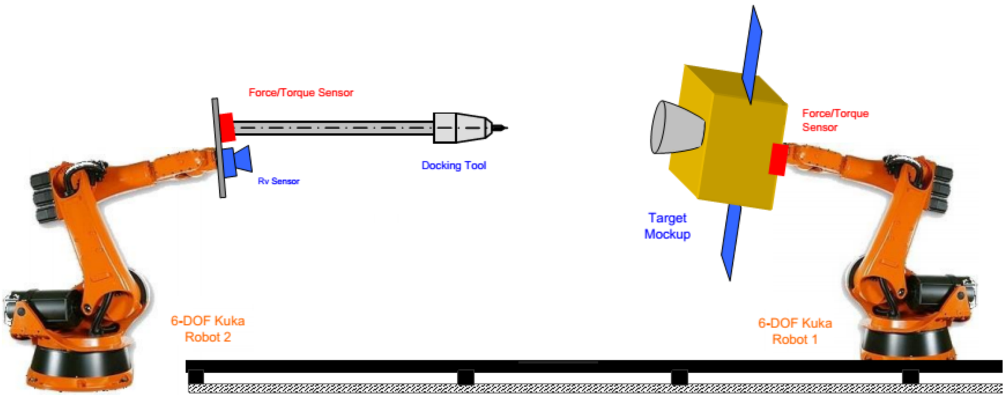
Force/Torque Sensor
Rv Sensor
Docking Tool
6-DOF Kuka Robot 2
Target Mockup
Force/Torque Sensor
6-DOF Kuka Robot 1

Figure 6.6 - EPOS architecture for contact dynamic simulation.
Source: Boge et al. (2011).

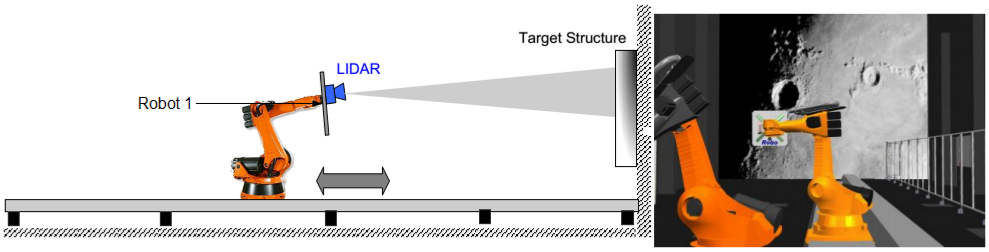
Target Structure
LIDAR
Robot 1

Figure 6.7 - Set-up for lander application simulation.
Source: Boge et al. (2011).

trolled axes which allow to move the tool adapter relative to the robots base. The easiest way to command any motion is to directly define an angle or an angular speed of movement for each robot's axis. Direct commanding of the axes is useful to move the robot manually, i.e., to check for axis limit. Figure 6.8 illustrates the orientation of each robot's axis in the IJT system.

Ideal Robot Device Coordinate Systems (IDC): each robot can be commanded by describing the position and orientation of a coordinate frame fixed at the robot adapter plate - called Tool Coordinate System (TCS) - with respect to the robot base (Base Coordinate System). The TCS has its origin in the middle of the robots tool flange where the Z axis is oriented perpendicular outwards of the breadboards mounting face whereas the X axis is oriented towards the electrical interface block on the backside of the breadboard. The Base Coordinate System has its origin in the middle of the robots mounting face. The Z axis is oriented towards the laboratory

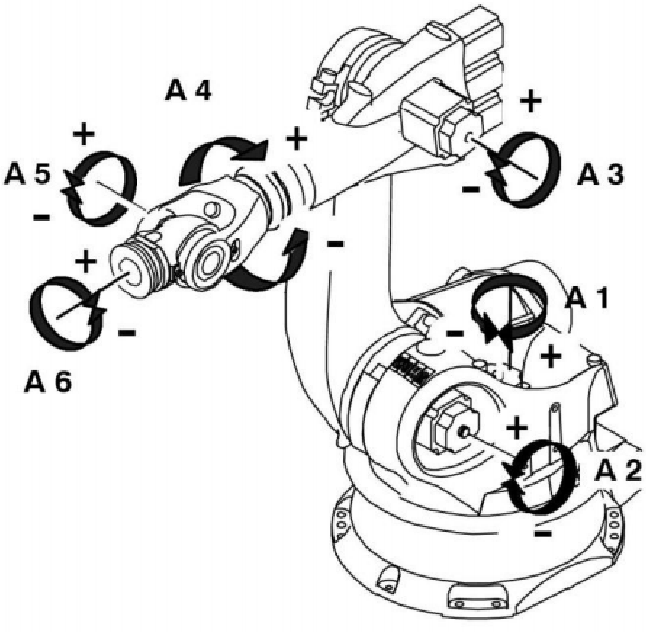

Figure 6.8 - Ideal Robot Joint Coordinate (IJT).
Source: Boge et al. (2011).

ceiling and the X axis is oriented to the opposite of the cable plugs at the back of the robot. Both reference frames are Cartesian coordinate systems, as shown in Figure 6.9, whose orientation is described by Euler angles with a 3-2-1 rotation sequence, i.e., first (A) rotation around Z axis, second (B) rotation around Y axis, and third (C) rotation around X axis.

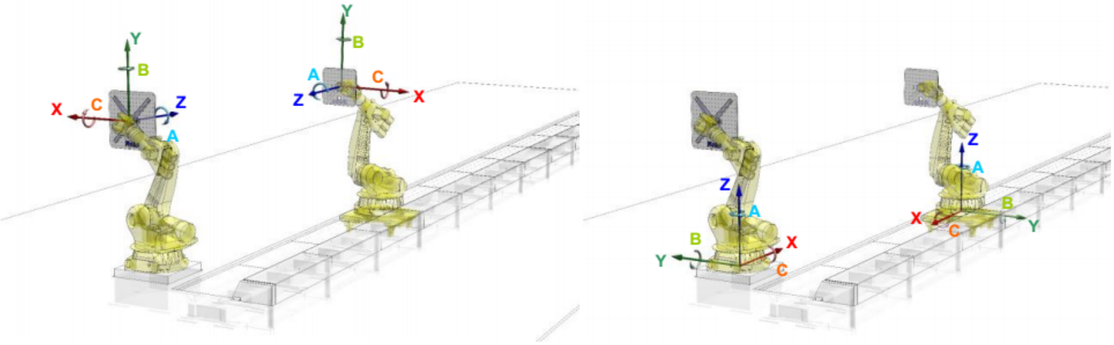

Figure 6.9 - Tool Coordinate System (left) and Base Coordinate System (right).
Source: Boge et al. (2011).

Global Laboratory Coordinate System (GLB): each robot can be commanded by describing the position and orientation of a frame fixed at the robot adapter plate with respect to a fixed Global Laboratory Coordinate System. The Z axis is defined as the intersection of the XZ-plane of the Robot 1 Base Coordinate System on the slide and the YZ-plane of the fixed Robot 2 Base Coordinate System; the X axis is located parallel but in opposite direction of X axis of the Robot 1 Base Coordinate System; and the Y axis completes the right-handed system (see Figure 6.10). The origin of such system is located at 1.5 m above the XY-plane of the Robot 2 Base Coordinate System. The rotation sequence follows the same process described for the IDC coordinate system.

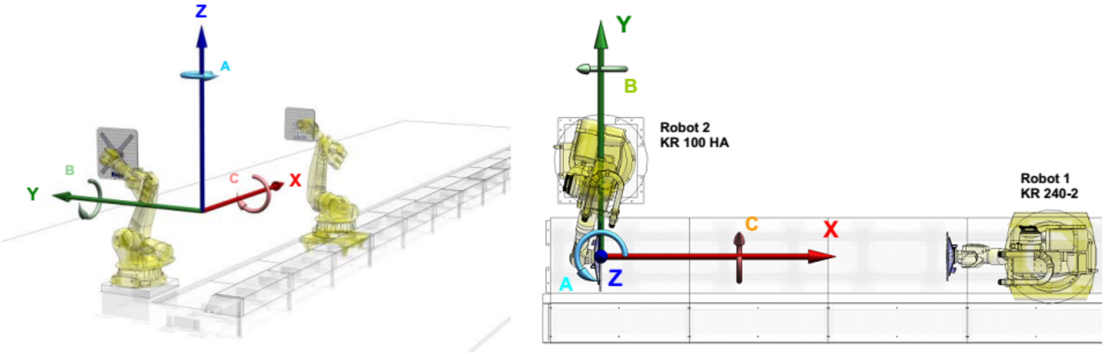

Figure 6.10 - Global Laboratory Coordinate System (GLB).
Source: Boge et al. (2011).

Clohessy Wiltshire Coordinate System (CLW): the facility can also be commanded by the well acquainted Clohessy Wiltshire Coordinate (CLW). EPOS is able to represent a defined reference frame fixed to Robot 1 or Robot 2. It also allows representing a reference frame, within the laboratory hall, for the formation of two spacecraft.

6.2 EPOS test campaign

This section aims to present the design concept of the HIL tests developed at EPOS facility. During a closed-loop simulation the output of the spacecrafts' dynamics is sent to the FMC computers and LRC units at every 4 ms. In other words, the approach trajectory is computed in real-time instead of having it pre-defined. Then the realistic movement of two satellites, based on physical equations of motion, is represented by the motion of the robots. A visual camera sensor measures the robot position with respect to the camera and send this information to the image processing unit included in a ACS computer with a update rate of 5 Hz. After processing it, the data are smoothed by a navigation filter, compared to a reference trajectory, and, based on this error, a control signal is handed over by the Controller to the AMCMs functions. Thus actuators models, commanded by the AMCMs, apply force and toque commands to the spacecrafts' dynamics closing the loop. A general diagram about the aforementioned process is presented in Figure 6.11.

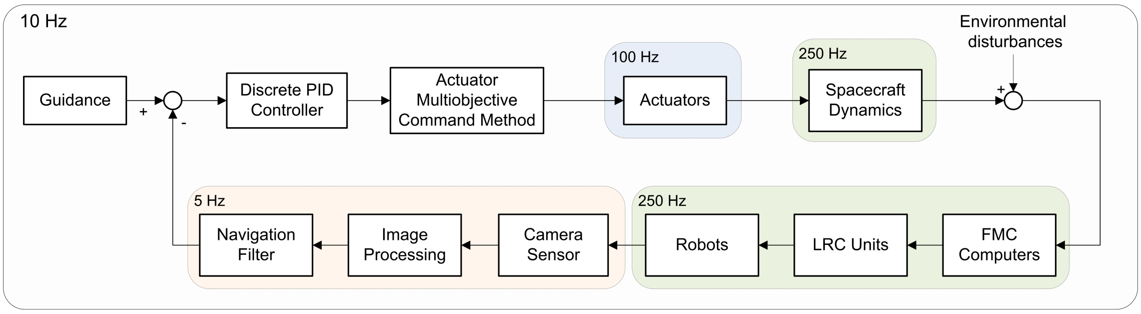
10 Hz
Guidance
+
-
Discrete PID Controller
Actuator Multiobjective Command Method
100 Hz
Actuators
250 Hz
Spacecraft Dynamics
Environmental disturbances
+
5 Hz
Navigation Filter
Image Processing
Camera Sensor
250 Hz
Robots
LRC Units
FMC Computers

Figure 6.11 - Closed-loop simulation concept including AMCM.

A Prosilica Gigabit Ethernet Vision camera (GC-655) has been used for capturing images (see Figure 6.12). It is a monochromatic charge coupled device (CCD) sensor with very high sensitivity delivering up to 90 frames per second at VGA resolution (640 × 480 pixels). The camera has also a high capacity of synchronization. In addition, trigger inputs can be used to trigger the acquisition.

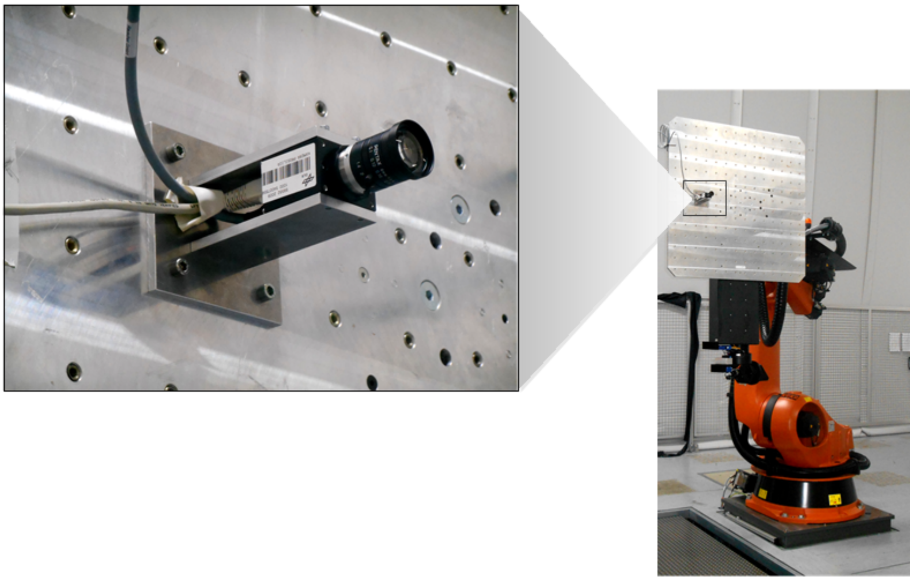

Figure 6.12 - Visual camera sensor coupled to Robot 2.

Image processing algorithms determine the pose of the target satellite in real-time. Since only a single camera is used, then additional information about the target is necessary to acquire full 6 degrees of freedom pose estimation. It means that the algorithm tracks a previously identified object. For the rendezvous simulations presented in this thesis a target body with known edge lengths is assumed. The close range method is based on a hybrid edge tracker which relies on contrast and texture of the image. The appropriate method is selected autonomously depending on the local surface properties. The fast Sobel filter (SOBEL; FELDMAN, 1968) which uses changes in the brightness has been usually applied. However, if the image is very noisy or if the local contrast is weak, then the texture segmentation method (SHAHROKNI et al., 2004) - which evaluates changes in the surface texture to detect edges - is preferable. For additional information about the image processing algorithm used in EPOS control system the reader is referred to Boge et al. (2011). Figure 6.13 shows a image of the target mock-up and the set of detected intersection points (yellow cross) at two different hold points: 10 m (left) and 20 m (right). Those images were caught during the test campaign presented in this thesis.

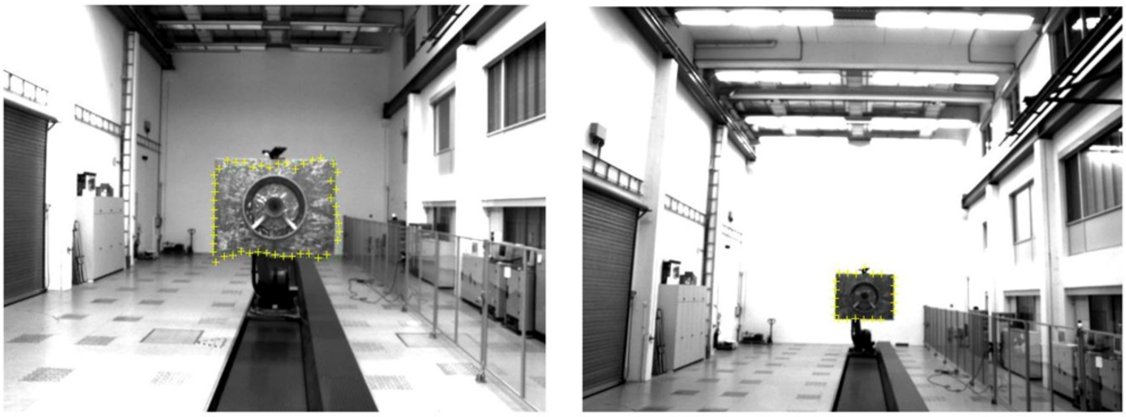

Figure 6.13 - Tracking edges of the target mock-up at 10 m (left) and 20 m (right).

The entire test campaign has covered several phases until achieving the final tests. After each phase, the logged data is analyzed and the proceeding to the next phase is performed only if stability conditions are achieved. The test plan is summarized in Table 6.2.

The first phase of this project is the integration of the Spacecraft Rendezvous and Attitude Simulator (SRAS) - developed to test the AMCM and the actuators models as explained in Chapter 2 - to the camera visual sensor model and image processing

Table 6.2 - EPOS test plan.

Phase	Description
1.	Integration of SRAS with the camera/image processing models of EPOS.
2.	Feasibility tests in simulation mode with 3D animation.
3.	Tests in open-loop mode using just the pinhole camera model.
4.	Tests in open-loop mode using a real sensor hardware in static position.
5.	Tests in open-loop mode using a real sensor hardware in static position followed by continuous approach.
6.	Tests in closed-loop mode using a real sensor hardware in static position.
7.	Tests in closed-loop mode using a real sensor hardware in static position followed by continuous approach.

algorithm provided by the EPOS group. Afterward, feasibility tests are carried out in simulation mode whose option, available in EPOS control system, allows to visualize the complete rendezvous simulation based on a 3D animation video (see Figure 6.14) before executing it with the real robots. This option works as a safety procedure because allows to check a priori any evidence of collision.

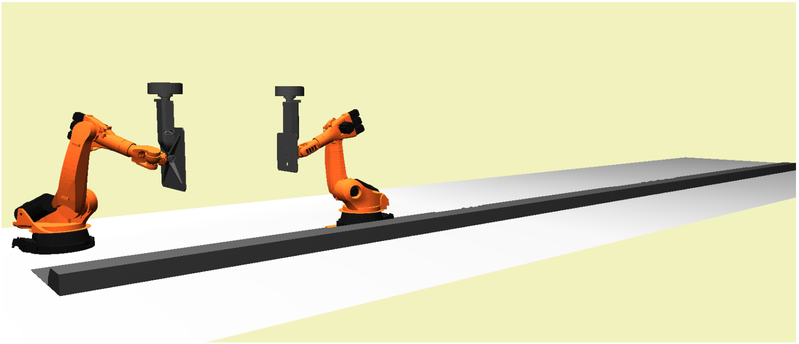

Figure 6.14 - EPOS simulation mode.

The next phase is the simulation in open-loop mode using the pinhole model of the visual camera sensor. Here the robots motion is just a reproduction of the numerical simulation, i.e., any data is not fed back to the simulator. Then the following phases are the simulations in open-loop mode using the real sensor hardware in static position and next a static position followed by continuous approach. Although the data is not fed back in open-loop mode, the utilization of a real sensor is important to check the continuous tracking conditions of the target mock-up. The final tests are performed in closed-loop mode using the real camera. Firstly, stability conditions in a static position is evaluated and then a continuous approach simulation is carried out. In this mode, the motion of the satellite mock-up is measured by the camera, processed by the image processing algorithms, and handed over to the GNC loop.

6.3 Results based on HIL Rendezvous Simulations

This section aims to show the results from phase 7 where HIL rendezvous simulations in closed-loop mode have been performed on EPOS during an approach from 20 m to 10 m. As in the numerical simulations, it is assumed an initial angular error of 10 degrees in Y_B axis to be corrected. Instead of offline tests, as presented before, in this phase the translational and rotational motions are controlled online and in a real-time environment based on measurements of a real visual camera sensor. The objective of these tests is to analyze the stability conditions of the proposed methods included in a HIL simulation. Three test cases have been performed: ideal actuators (IA), AMCM-I, and AMCM-II. The ideal case (IA) assumes a linear actuator, i.e., the applied force and torque commands are exactly equal to the controller's output. The main simulation parameters are the same presented in Table 4.2. Here AMCM-I case uses thrusters with nominal thrust of 1 N whereas thrusters with nominal thrust of 4 N has been used in the AMCM-II case. The ideal and AMCM-I cases use a constant velocity of approach of 0.05 m/s whereas the case AMCM-II has a constant velocity of 0.03 m/s. The first set of plots, Figures 6.15, 6.16, and 6.17, show the commanded translational (left) and rotational position (right) for the IA, AMCM-I, and AMCM-II cases, respectively. These data, commanded to the robots, represent the real state (dynamics output).

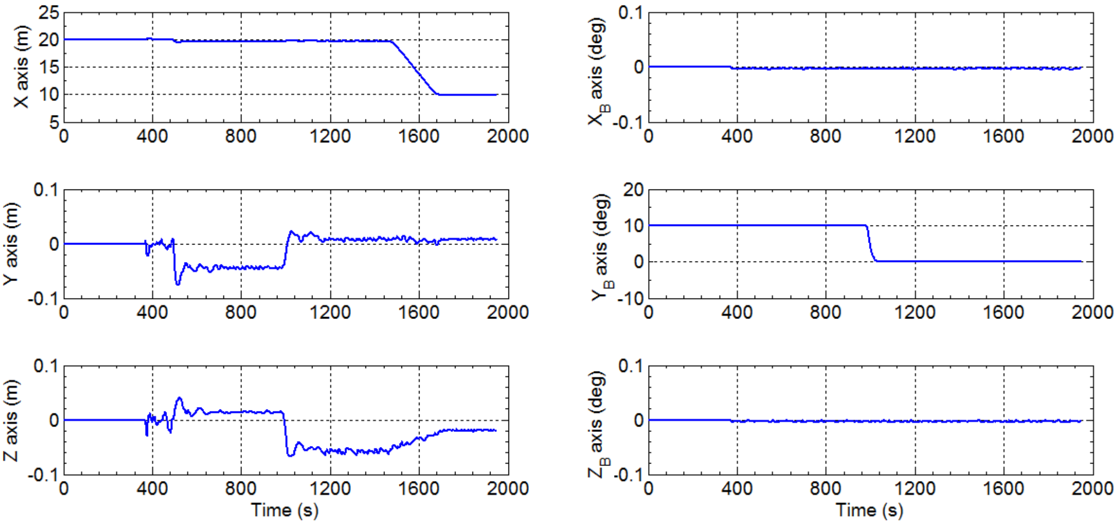

Figure 6.15 - Commanded translational (left) and rotational (right) position as a function of time: ideal actuator case.

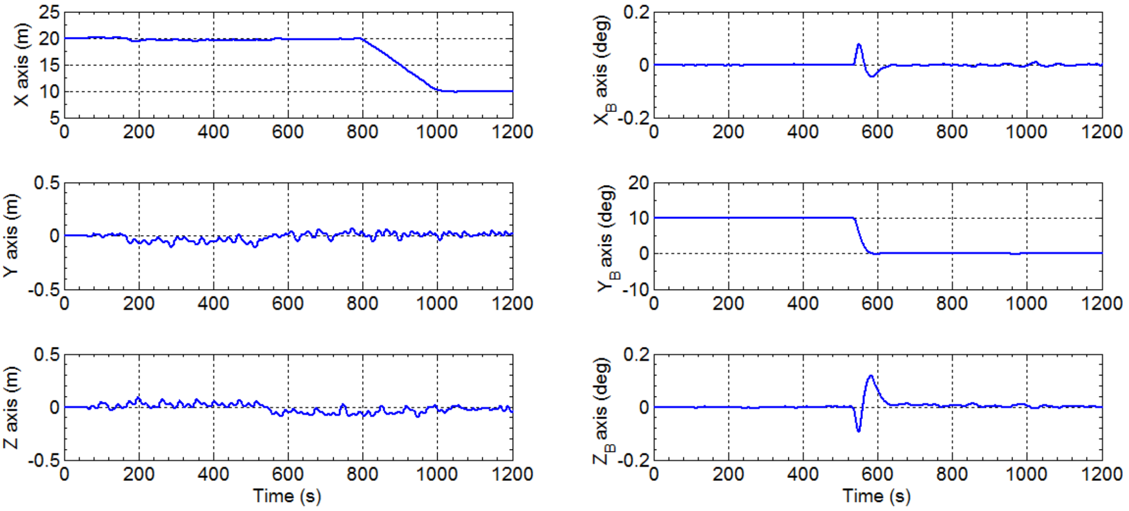

Figure 6.16 - Commanded translational (left) and rotational (right) position as a function of time: AMCM-I case.

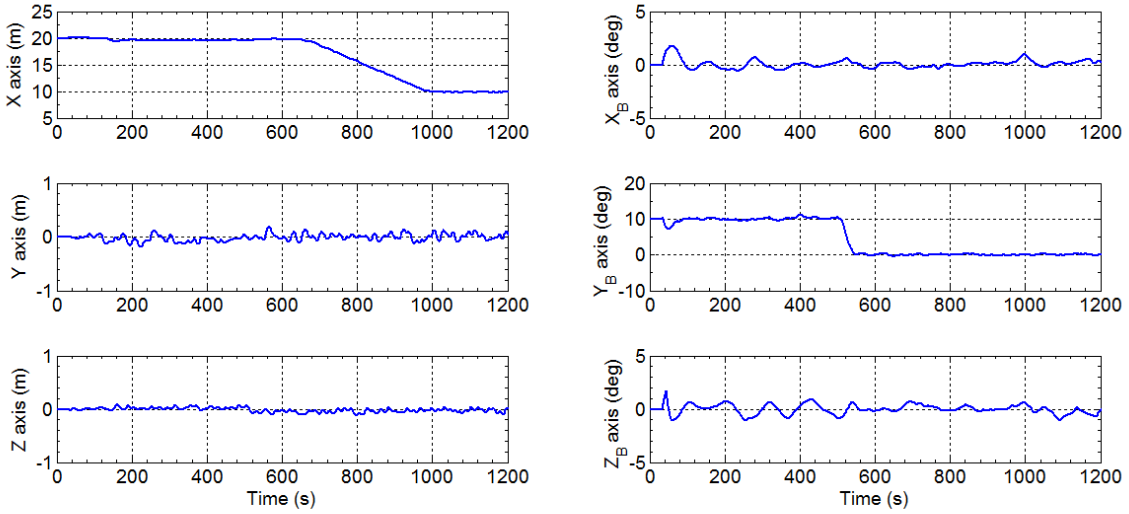

Figure 6.17 - Commanded translational (left) and rotational (right) position as a function of time: AMCM-II case.

For safety reasons, every HIL test begins with null measurement errors (an ideal sensor is assumed). This fact explains the non-oscillatory behavior of Figure 6.15 until the instant of 350 s. Afterward, the pinhole camera model is activated. Then about the instant of 500 s the real camera starts to be used to measure the approach position. It is possible to see, mainly in Figure 6.15, a transient behavior due to the higher bias error inherent from the real camera. Around the instant of 960 s starts the rotational motion. This maneuver turns out in a reduction of the error in Y axis but, on the other hand, an increasing of the error in Z axis. This error is reduced again as long as the approach motion is carried out. As can be seen in Figure 6.15, very low magnitude errors are achieved using ideal actuators for providing force and torque commands. Figure 6.16 shows the time response of a combination of actuators (RCS, reaction wheels, and magnetic torqrods) and although the oscillation level is higher than the ideal case, as expected, the stability conditions are quite satisfactory. When the attitude motion begins, a transient behavior in X_B and Z_B axes occur due to the RCS coupling effects. Figure 6.17 shows the time translational (left) and angular response (right) of a GNC loop using only RCS as actuators. Since thrusters cannot apply very low levels of torque as reaction wheels and magnetic torqrods, then we can see a higher level of oscillation in X_B an Z_B axes with respect to the angular motion. However, even with this characteristics, the AMCM-II case worked properly integrated to the EPOS control system and achieved the steady state.

The relative position error between the state measured by the real camera and the state commanded to the facility, for the IA, AMCM-I, and AMCM-II cases, is presented in Figure 6.18, 6.19, and 6.20, respectively. Greater errors can be seen at the initial steps due to the image processing time and the convergence time of the filter. The deviation is reduced to acceptable levels throughout the simulation. Those plots show that all simulation cases achieved the stability condition and worked properly in a real-time environment.

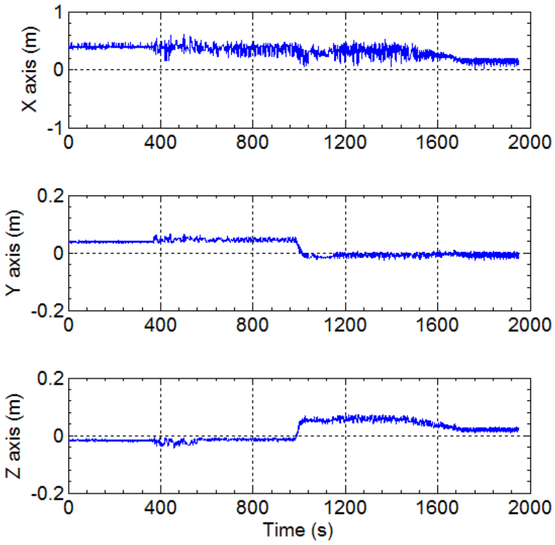

Figure 6.18 - Relative position error of the real camera sensor: ideal actuator case.

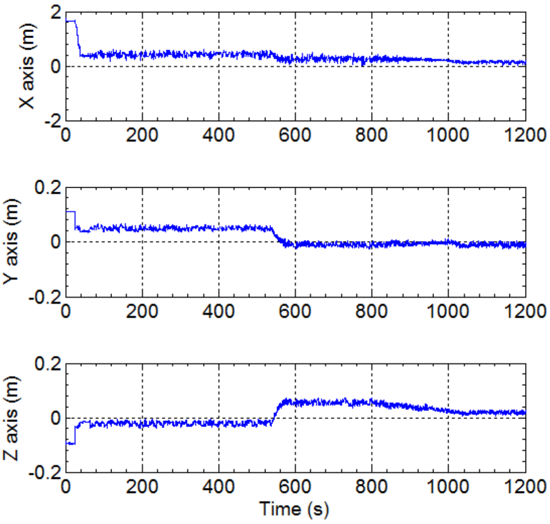

Figure 6.19 - Relative position error of the real camera sensor: AMCM-I case.

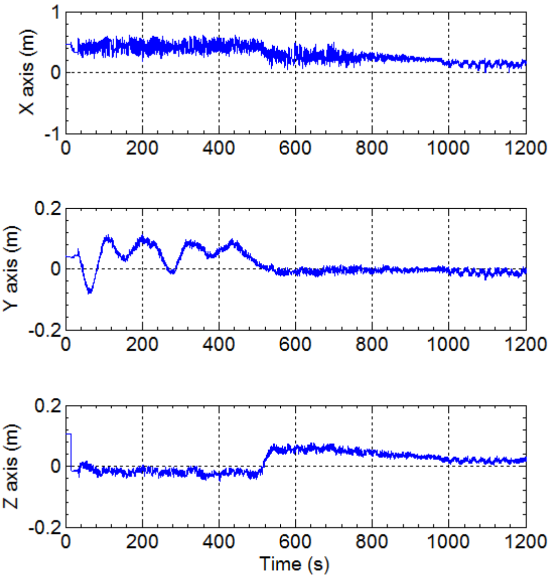

Figure 6.20 - Relative position error of the real camera sensor: AMCM-II case.

Since the focus of this thesis is the command of actuators, then it makes sense to look into the force and torque applied by these devices. Figure 6.21, 6.22, and 6.23 show the force (left) and torque (right) applied to the spacecraft dynamics for the ideal, AMCM-I, and AMCM-II cases, respectively. The ideal actuator response, shown in Figure 6.21, presented very high peaks of force when the real camera is included in the loop (time $\cong$ 350 s) but returning to low levels subsequently even during the approach maneuver. A high peak of torque (about 0.2 Nm) is applied when the rotational motion is started. The combination of force and torque applied by the set of actuators of AMCM-I case, for a given period of simulation (from 500 s to 700 s), is shown in Figure 6.22. This period corresponds to the time where the attitude maneuver is carried out. On the left side of this plot is shown the force pulses applied by the RCS to correct the translational deviation whereas on the right side is presented the combination of torque commands applied by the RCS, reaction wheels, and magnetic torqrods. Concerning the rotational motion, the force pulses provided by RCS have been applied sporadically along the Y_B axis due to a higher error level while the torque provide by the other attitude actuators works as a fine control for lower error levels. The force and torque pulses, applied by the RCS of the AMCM-II case, for a brief period of simulation (from 400 s to 600 s) is presented in Figure 6.23.

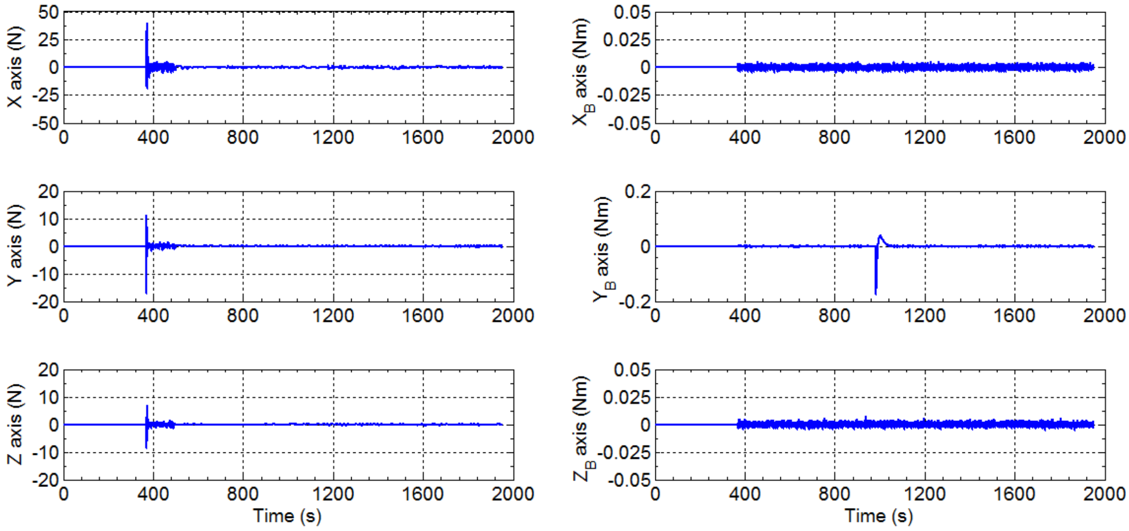

Figure 6.21 - Applied force (left) and torque (right) as a function of time: ideal actuator case.

The position and velocity estimated by the navigation filter for the cases IA, AMCM-I, and AMCM-II, are presented in Figure 6.24, 6.25, and 6.26, respectively. In all plots we can see that the estimated position magnitude (on the left side) is lower than the real state presented in the commanded position plots. An interesting behavior that deserves to be pointed out is the velocity profile in X axis. As commented in Chapter 2, the reference trajectory profile is composed by an acceleration phase, a constant velocity phase, and a deceleration phase, as shown in the estimated velocity plots.

For understanding the behavior of the six independent servo controlled axes of the

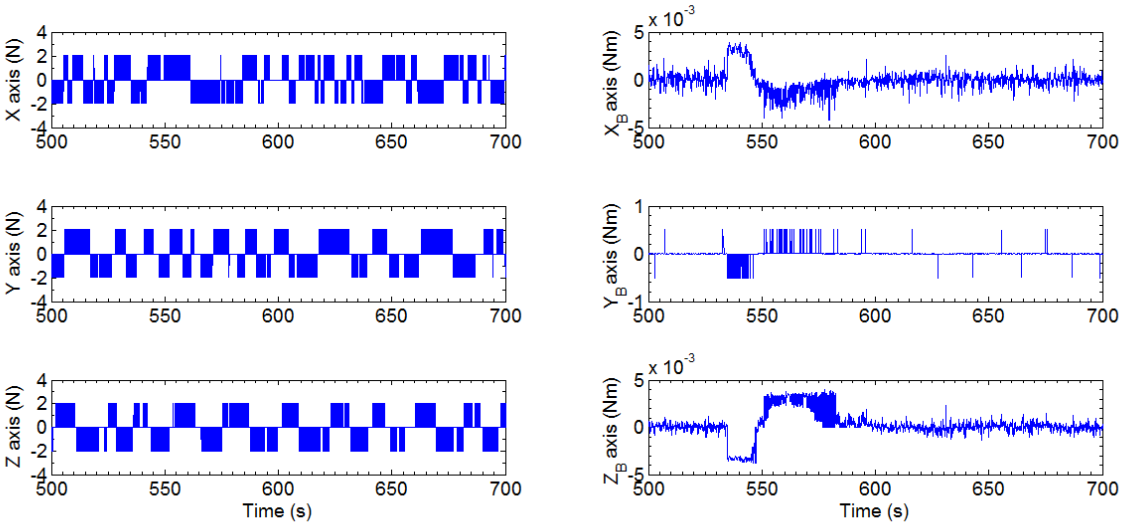

Figure 6.22 - Applied force (left) and torque (right) as a function of time: AMCM-I case.

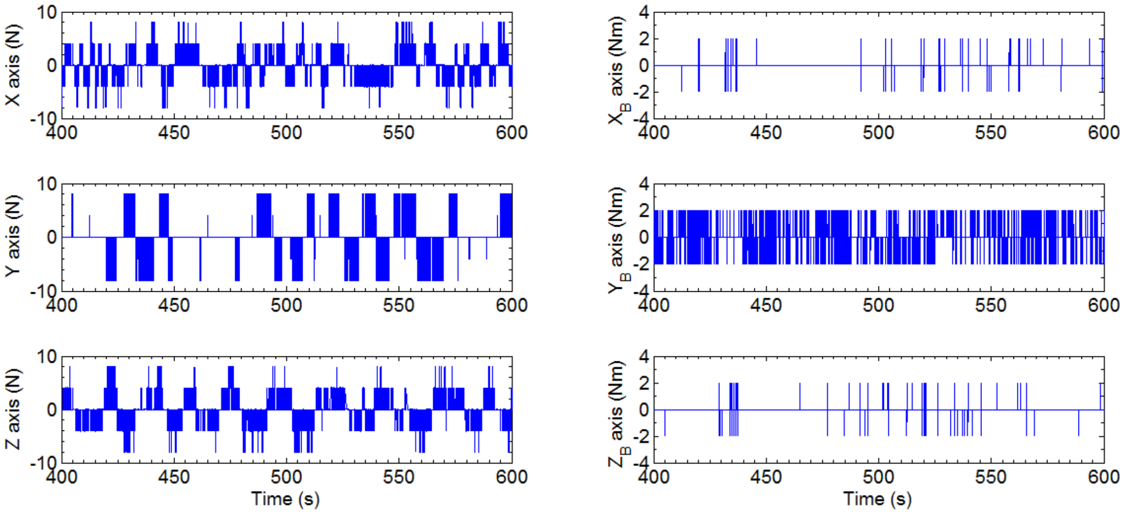

Figure 6.23 - Applied force (left) and torque (right) as a function of time: AMCM-II case.

robots, Figures 6.27 and 6.28 present the robots' joints motion of Robot 1 and Robot 2, respectively. These data, expressed in the IJT system (as described in Section 6.1.4), are based on the maneuver performed on AMCM-I case. The six robot joints are labeled from A1 to A6 (see Figure 6.8). In addition, it is also shown, in Figure 6.27, the displacement of Robot 1 on the linear slide. As can be seen, there is an offset among the origin of the coordinate frame and the base of the robot. Since the representation in space of the translational and rotation motion are relatives, Robot 2 represented the most part of the rotational motion among the vehicles whereas the approach motion was executed by the Robot 1.

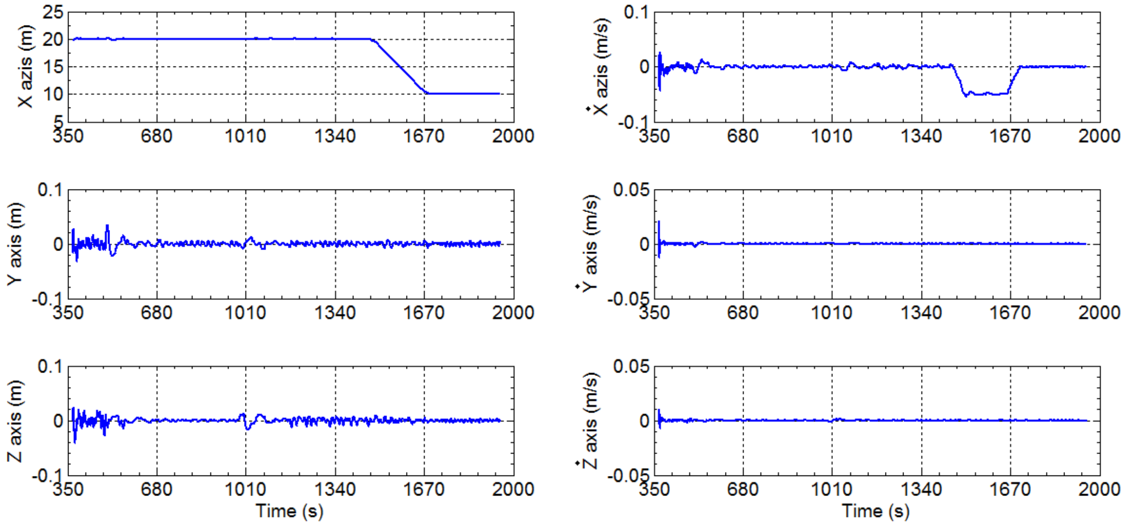

Figure 6.24 - Estimated position (left) and velocity (right) as a function of time: ideal case.

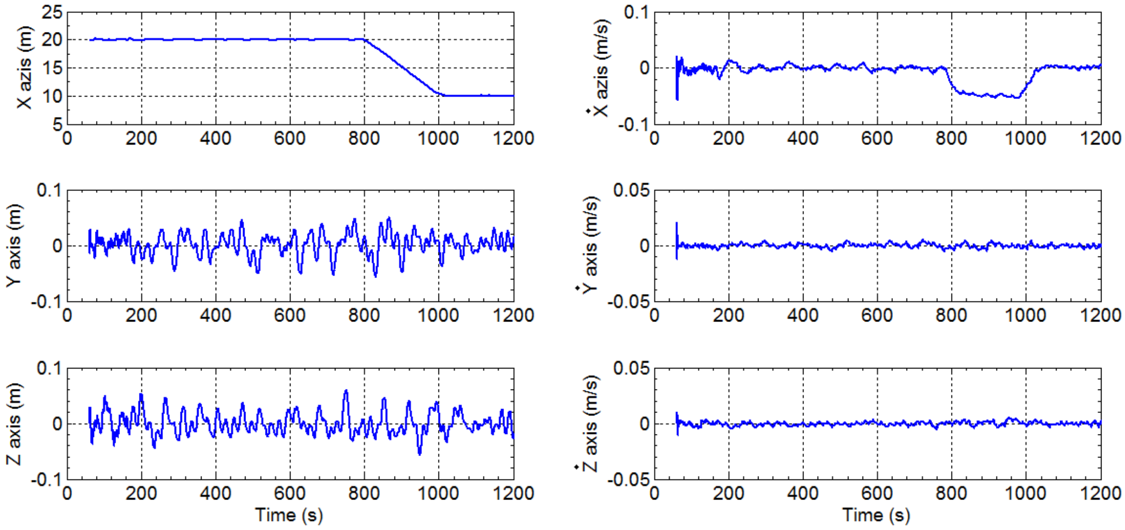

Figure 6.25 - Estimated position (left) and velocity (right) as a function of time: AMCM-I case.

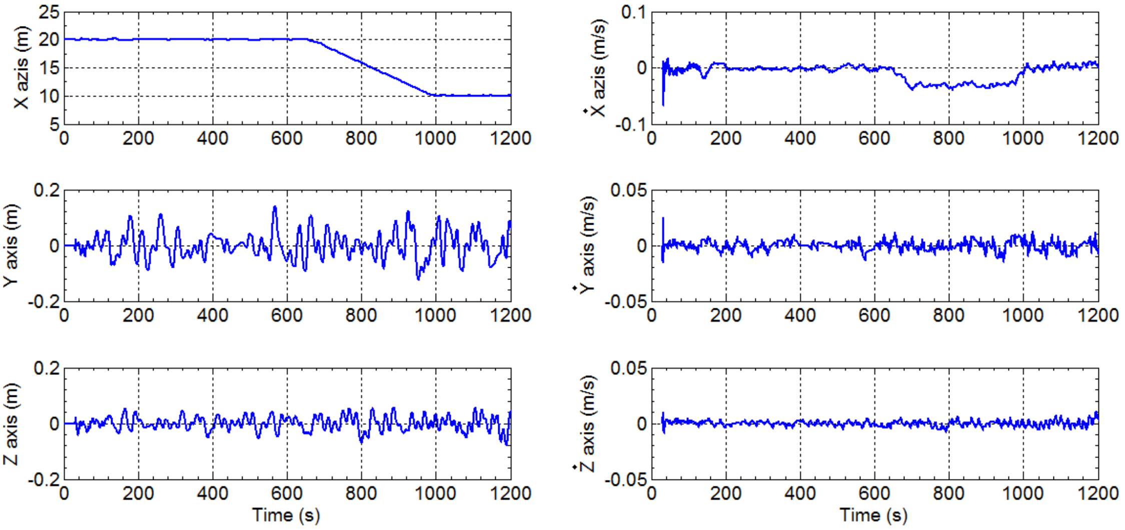

Figure 6.26 - Estimated position (left) and velocity (right) as a function of time: AMCM-II case.

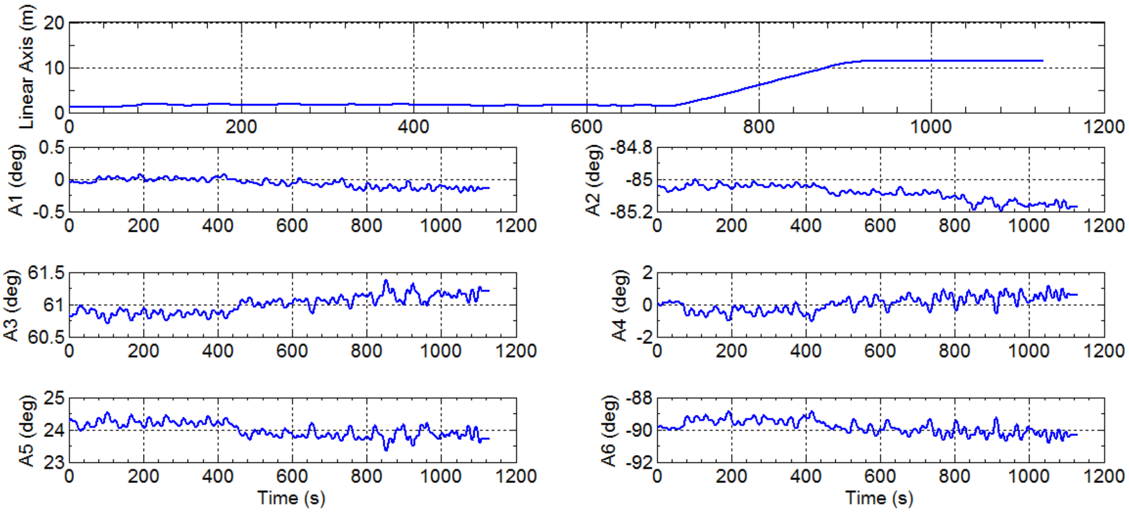

Figure 6.27 - Motion of the Robot 1 in the IJT coordinate frame for the AMCM-I case.

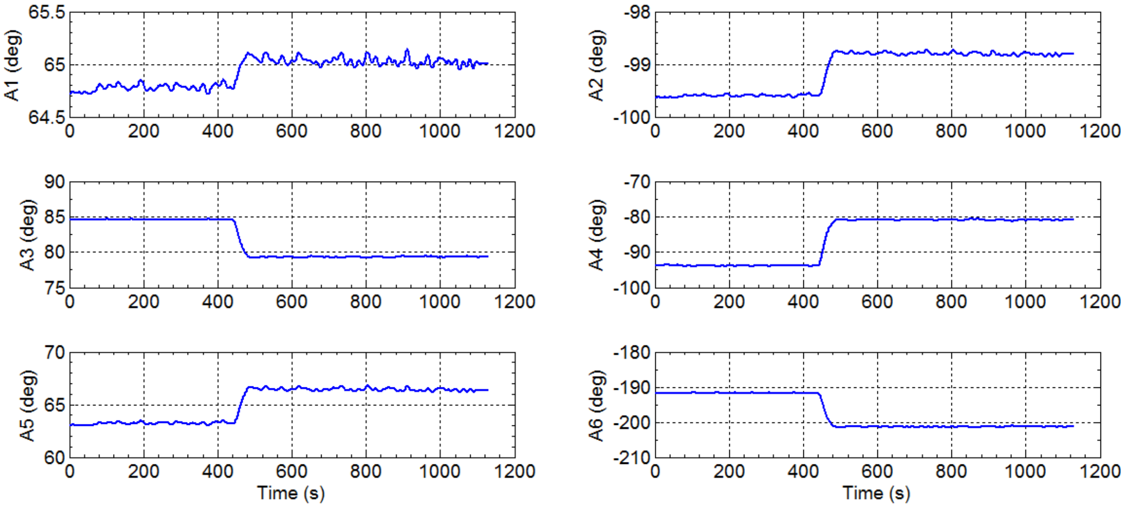

Figure 6.28 - Motion of the Robot 2 in the IJT coordinate frame for the AMCM-I case.

7 CONCLUSIONS AND COMMENTS

The mankind, guided by space agencies, has always pursued to overcome the space frontier developing new spacecraft and technologies for exploring the universe or just for improving the Earth's orbiting services provided by satellites and space stations. The challenge of using as efficiently as possible the spacecraft technologies has motivated the investigation of new optimization methods in order to extend the spacecraft's life and to insure all requirements of the mission. In addition, unexpected failures of spacecraft actuators faced during the space mission has led to the exploration of alternative autonomous techniques of spacecraft control.

A review of available optimization methods applied to the spacecraft control have shown some points that could be improved or better explored. In advance, several missing points from the actuators command problem have been selected to be investigated in this thesis. Based on this issue, four design requirements have been taken into account: flexible software architecture; optimal control; autonomous decision making; and computational efficiency. Then a novel autonomous command method based on a discrete multiobjective optimization approach has been proposed herein. This methodology, called Actuator Multiobjective Command Method (AMCM), generates a set of feasible solutions and selects the best compromise solution optimizing a group of objective functions simultaneously and completely online. Given a group of actuators with conflicting behavior, AMCM determines the best way to operate them according to predefined specifications and online acquired inputs. The decision making method has considered two approaches in this thesis: all candidates are taken into account in the selecting process; and only the set of non-dominated solutions. In order to test the proposed method in a more realistic scenario, models for all components of the complete GNC loop have been developed and accurately implemented in a simulation framework. The final product of this thesis turns out in a software package able to be integrated to any rendezvous and attitude simulator.

An introduction to the actuator command problem was given in Chapter 3. The proposed approach is employed for optimally designing a linear time-invariant control system composed of three conflicting parallel linear first-order actuators. An analysis about the location of the closed-loop poles and zeros has evidenced that the system's performance might be significantly changed through the actuators' gains. However, investigation on the objective space of two performance parameters (settling time and overshoot) has shown that a non-systematic method for defining the actuators' gains could even increase the objective functions. Therefore, the use of a multiobjective optimization approach merged with a decision making method has achieved a better step time response when compared to the case where only a single actuator is used.

Motivated by this findings, the multiobjective optimization approach is used for commanding different types of spacecraft actuators included in a nonlinear complex control system, generating then the AMCM-I, as described in Chapter 4. Unlike the design problem, AMCM-I works autonomously and online operating a group of nonlinear actuators. Herein the multiobjective approach optimizes simultaneously the main actuators' characteristics: the torque error, the fuel and electrical charge consumptions, the disturbance of coupling, and the risk of utilization of each actuator. This new strategy has shown being capable of achieving excellent results, in terms of performance parameters, based on a combination of torque commands. In summary, AMCM-I achieved a satisfactory angular error, kept acceptable levels of fuel and electrical charge consumptions, low levels of disturbance of coupling and risk of utilization, and presented the fastest settling time of angular response with respect to the others configurations.

Another application of this novel approach, called AMCM-II and presented in Chapter 5, represent an improvement over the operation of spacecraft thrusters applied to a RCS configuration. Unlike to many works which assume just a single parameter to be optimized - usually the fuel propellant consumption -, the proposed method optimizes simultaneously a group of four objectives for selecting the best combination of thrusters and their firing pulse duration. These objectives functions - force error, torque error, propellant consumption, and total number of pulses - represent important issues for the success and longevity of the mission. The comparison among two decision making methods: the well known Weighted Sum Method and the alternative method Smallest Loss Criterion, has evidenced the importance and advantage of considering all objectives equally. Additional tests proved the capacity of this method of performing successfully a couple translational and rotational maneuver, even in a thrusters failure scenario.

Validation tests carried out at the European Proximity Operations Simulator (EPOS) have proved the computational efficiency of the proposed methods. As described in detail in Chapter 6, HIL rendezvous simulations allowed to test and validate the models under a realistic real-time environment condition. Closed-loop tests evaluated the models' stability conditions based on measurements provided by a real visual camera sensor. Beyond insuring the stability conditions during the approach continuous phases as well as at the hold points, the state errors have been kept within acceptable ranges. In summary, the implemented software demonstrated effectiveness and robustness and proved to be able to generate reliable results in both non-real-time and real-time simulations. The work presented here does not only solve an multiobjective optimization problem but it is also efficient in terms of a computational point of view.

7.1 Contributions

The main contribution of this thesis is providing a powerful and innovative method, named AMCM, for autonomously commanding a group of conflicting spacecraft actuators based on the environmental acquired information and the actuators' predefined data. Several new points have been explored in this thesis turning out in original scientific contributions. The utilization of a intelligent system capable of optimize, decide, and command the spacecraft actuators autonomously - assuming the approach described in this thesis - is a point not explored before in the literature. Moreover, the developed methodology has proven to be successfully applicable to three different scenarios: the design of a control system, the command of three different types of actuators, and the operation of a coupled group of thrusters (the RCS set-up).

One of the outstanding contributions of this novel algorithm is the possibility of application to any scenario where there are conflicting actuators and a group of objectives to be optimized. Another contribution is the improvement of the EPOS control system. The original GNC loop of EPOS is composed of ideal and linear actuators comprised of linear saturation functions. Once tested and validated the models presented herein, a software package called ActMod, composed of the nonlinear actuators models and the AMCM models, was handed over to the EPOS team to be integrated to the EPOS control system in order to improve the performance of this fascinating HIL rendezvous simulator. A complete description of the features of this software package is reported in Gomes dos Santos (2014). In addition, some results from this thesis were presented and published at the AIAA Guidance, Navigation, and Control Conference 2015 which took place in Kissimmee / Florida (GOMES DOS SANTOS et al., 2015).

7.2 Future works

This thesis is far from exhausting the subject presented here and modeling improvements can be accomplished. Future innovations related to this work could concentrate in the following implementations:

- formulate and implement the evolution of the CoM position in the dynamics equations;
- consider different shapes of body vehicles and RCS set-ups in the mathematical formulation;
- apply a multiobjective optimization approach to the RCS design problem;
- consider sloshing and flexible appendages in the spacecraft modeling;
- evaluate the proposed approach in the docking process;
- implement and test the proposed algorithms in a simple micro-controller (such as 8051) for controlling a group of real hardware actuators.

Additional improvements could be accomplished by taking advantage of information provided by real spacecraft missions as well as from eventual actuators failures. At last, the novelty of this research can lead to a wide range of further works.

REFERENCES

ANKERSEN, F.; WU, S.; ALESHIN, A.; VANKOV, A.; VOLOCHINOV, V. Optimization of spacecraft thruster management function. **Journal of Guidance, Control and Dynamics**, v. 28, n. 6, p. 1283–1290, 2005. 3, 23

ARANTES JR., G.; ROCCO, E. M.; KOMANDURI, A. S. Far and close approaching strategies for rendezvous and docking operations applied to on-orbit servicing. In: SIVASUNDARAM, S. (Ed.). **Mathematical analysis and applications in engineering aerospace and sciences**. Embry Riddle Aeronautical University, USA: Cambridge Scientific, 2010. v. 5, p. 1–29. 300 pp. 11

ÄSTRöM, K. J.; WITTENMARK, B. **Computer-controlled systems**: theory and design. Beijing, China: Prentice Hall, 1997. 557 p. 19

BALS, J.; FICHTER, W.; SURAUER, M. Optimization of magnetic attitude- and angular momentum control for low earth orbit satellites. In: INTERNATIONAL CONFERENCE ON SPACECRAFT GUIDANCE, NAVIGATION AND CONTROL SYSTEMS, ESA SP-381., 1997, Noordwijk, The Netherlands. **Proceedings...** Noordwijk: ESA, 1997. p. 559–567. 4

BASIC, M. On hardware-in-the-loop simulation. In: CONFERENCE ON DECISION AND CONTROL, 2005, Seville, Spain. **Proceedings...** Seville: IEEE, 2005. p. 3194–3198. 4

BAZOVSKY, I. **Reliability theory and practice**. Englewood Cliffs, New Jersey: Prentice-Hall, 1961. 292 p. p. 28, 29

BENNETT, S. A brief history of automatic control. **IEEE Control Systems Magazine**, v. 16, n. 3, p. 17–25, 1996. 1

BENNINGHOFF, H.; REMS, F.; BOGE, T. Development and hardware-in-the-loop test of a guidance, navigation and control system for on-orbit servicing. **Acta Astronautica**, v. 102, p. 67–80, 2014. 4

BISHOP, R. H. **The mechatronics handbook**. Florida, USA: CRC Press LLC, 2002. 2

BOGE, T. **EPOS user manual**. Oberpfaffenhofen/Germany, 2011. Technical Report, 54 p. 103, 104

BOGE, T.; BENNINGHOFF, H.; TZSCHICHHOLZ, T. Hardware-in-the-loop rendezvous simulation using a vision based sensor. In: INTERNATIONAL ESA CONFERENCE ON GUIDANCE, NAVIGATION AND CONTROL SYSTEMS, 2011, Karlovy, Czech Republic. **Proceedings...** Karlovy: ESA, 2011. 30, 31, 32, 101, 104, 105, 106, 107, 109

BOGE, T.; BENNINGHOFF, H.; ZEBENAY, M.; REMS, F. Using robots for advanced rendezvous and docking simulation. In: SIMULATION AND EGSE FACILITIES FOR SPACE PROGRAMMES, 2012, Noordwijk, The Netherlands. **Proceedings...** Noordwijk: SESP, 2012. 4

BRUALDI, R. A. **Introductory combinatorics**. New York: Pearson Education, 1992. 58

BRUNO, D. Contigency mixed actuator controller implementation for the dawn asteroid rendezvous spacecraft. In: CONFERENCE AND EXPOSITION, AIAA 2012-5289., 2012, Pasadena, California. **Proceedings...** Pasadena: AIAA, 2012. 3

CHAGAS, R. A. J.; GALSKI, R. L.; DE SOUZA, F. L. Orbgeo - an orbit selection tool for satellite constellations using the multiobjective generalized extremal optimization (mgeo) algorithm. In: INTERNATIONAL CONFERENCE ON SYSTEMS & CONCURRENT ENGINEERING FOR SPACE APPLICATIONS, 2014, Stuttgart, Germany. **Proceedings...** Stuttgart: SECESA, 2014. 4

COHON, J. L. **Multiobjective programming and planning**. Mineola, NY: Dover Publications, 2003. 4, 34, 36

COLLETTE, Y.; SIARRY, P. **Multiobjective optimization**: principles and case studies. Berlin: Springer-Verlag, 2003. 293 p. p. 33, 35, 36, 37, 38, 39, 40

COSTA FILHO, A. C. **Coupling Analysis Between Attitude Control and Orbital Maneuvering Trajectory During Continuous Thrust (in portuguese)**. 135 p. Dissertation (Master of Science in Space Mechanics and Control) — Instituto Nacional de Pesquisas Espaciais (INPE), São José dos Campos, 2010. 43

CRAWFORD, B. S. Configuration design and efficient operation of redundant multi-jet systems. In: GUIDANCE CONTROL AND FLIGHT MECHANICS CONFERENCE, AIAA 69-845., 1969, Princeton, New Jersey. **Proceedings...** Princeton: AIAA, 1969. 22

DENNEHY, C. J. Spacecraft hybrid (mixed-actuator) attitude control experiences on nasa science missions. In: INTERNATIONAL ESA CONFERENCE ON GUIDANCE, NAVIGATION & CONTROL SYSTEMS, 2014, Porto, Portugal. **Proceedings...** Porto: ESA, 2014. 3

DUMMER, G. W. A.; WINTON, R. C. **An elementary guide to reliability**. Oxford, UK: Pergamon Press, 1968. 59 p. p. 28

EHRGOTT, M.; GANDIBLEUX, X. **Multiple criteria optimization**: state of the art annotated bibliographic surveys. New York: Kluwer Academic Publishers, 2003. Chapter 8. 34

EUROPEAN SPACE AGENCY. **ESA atv blog**. 2011. Available from: <`blogs.esa.int/atv/?attachment_id=1013`>. Access in: January 21th, 2015. 20

FAN, Z.; HUA, S.; CHUNDI, M.; YUCHANG, L. An optimal attitude control of small satellite with momentum wheel and magnetic torqrods. In: WORLD CONGRESS ON INTELLIGENT CONTROL AND AUTOMATION, 2002, Shanghai, China. **Proceedings...** Shanghai: IEEE, 2002. p. 1395–1398. 4

FEHSE, W. **Automated rendezvous and docking of spacecraft**. Cambridge, UK: Cambridge University Press, 2003. 7, 8, 10, 11, 18, 19, 21, 22, 32, 33, 73, 84

FINLAY, C. C.; MAUS, S.; BEGGAN, C. D.; BONDAR, T. N.; CHAMBODUT, A.; CHERNOVA, T. A.; CHULLIAT, A.; GOLOVKOV, V. P.; HAMILTON, B.; HAMOUDI, M.; HOLME, R.; HULOT, G.; KUANG, W.; LANGLAIS, B.; LESUR, V.; LOWES, F. J.; LÜHR, H.; MACMILLAN, S.; MANDEA, M.; MCLEAN, S.; MANOJ, C.; MENVIELLE, M.; MICHAELIS, I.; OLSEN, N.; RAUBERG, J.; ROTHER, M.; SABAKA, T. J.; TANGBORG, A.; TØFFNER-CLAUSEN, L.; THÉBAULT, E.; THOMSON, A. W. P.; WARDINSKI, I.; WEI, Z.; ZVEREVA, T. I. International geomagnetic reference field: the eleventh generation. **Geophysical Journal International**, v. 183, n. 3, p. 1216–1230, 2010. 26

FONSECA, I. J.; LOURENCAO, P. T. M.; OLIVEIRA, J. R. F. Procedimentos para a estabilização passiva de um satélite sob condições inerciais críticas. In: CONGRESSO BRASILEIRO DE ENGENHARIA MECANICA, 1985, São José dos Campos, SP. **Proceedings...** São José dos Campos: COBEM, 1985. 19

GARCIA, R. V. **Sigma Point Nonlinear Kalman Filter with Unscented Algorithm Applied to Attitude Dynamics Estimation of Artificial**

Satellites (in portuguese). 192 p. Thesis (Doctorate in Space Engineering and Technology) — National Institute for Space Research (INPE), São José dos Campos, 2011. 14

GE, S.; CHENG, H. A comparative design of satellite attitude control system with reaction wheel. In: CONFERENCE ON ADAPTIVE HARDWARE AND SYSTEMS, 2006, Istambul, Turkey. **Proceedings...** Istambul: IEEE, 2006. p. 359–364. 24

GOMES DOS SANTOS, W. **Aeroassisted Maneuvers Simulations of a Spacecraft Controlled by Adjustable Aerodynamic Plates and Thruster System (in portuguese)**. 272 p. Dissertation (Master of Science in Space Mechanics and Control) — Instituto Nacional de Pesquisas Espaciais (INPE), São José dos Campos, 2011. 18, 43

GOMES DOS SANTOS, W. **EPOS 2.0 - SW documentation**: actuators model (actmod) - 1.0. Oberpfaffenhofen/Germany, 2014. 38 p. - Technical Report. 123

GOMES DOS SANTOS, W.; KUGA, H. K.; ROCCO, E. M. Application of the kalman filter to estimate the state of an aerobraking maneuver. **Mathematical Problems in Engineering**, v. 2013, 2013. 18, 43

GOMES DOS SANTOS, W.; ROCCO, E. M. Trajectory control with continuous thrust applied to a rendezvous maneuver. **Journal of Physics: Conference Series**, v. 465, n. 1, 2013. 13

GOMES DOS SANTOS, W.; ROCCO, E. M.; BOGE, T.; REMS, F.; BENNINGHOFF, H. Discrete multiobjective optimization methodology applied to the mixed actuators problem and tested in a hardware-in-the-loop rendezvous simulator. In: GUIDANCE, NAVIGATION AND CONTROL CONFERENCE, AIAA 2015-1991., 2015, Kissimmee, Florida. **Proceedings...** Kissimmee: AIAA, 2015. 123

GOMES DOS SANTOS, W.; ROCCO, E. M.; CARRARA, V. Trajectory control during an aeroassisted maneuver between coplanar circular orbits. **Journal of Aerospace Technology and Management**, v. 6, n. 2, p. 159–168, 2014. 18, 43

GONCALVES, L. D.; ROCCO, E. M.; DE MORAES, R. V. Orbital disturbance analysis due to the lunar gravitational potential and deviation minimization through the trajectory control in closed loop. **Journal of Physics**, v. 465, n. 1, 2013. 43

GONNAUD, J. L.; PASCAL, V. Atv guidance navigation and control for rendezvous with iss. In: INTERNATIONAL CONFERENCE ON SPACECRAFT GUIDANCE, NAVIGATION AND CONTROL SYSTEM, ESA SP-425., 2000, The Netherlands. **Proceedings...** The Netherlands: ESA, 2000. p. 501–510. 3

HALL, C. D.; PANAGIOTIS, T.; SHEN, H. Tracking rigid body motion using thrusters and momentum wheels. **Journal of the Astronautical Sciences**, v. 50, n. 3, p. 311–323, 2002. 3

HARTLEY, R.; ZISSERMAN, A. **Multiple view geometry in computer vision**. Cambridge, UK: Cambridge University Press, 2004. 2nd ed. 30

HIBBELER, R. C. **Engineering mechanics**: dynamics. Upper Saddle River, New Jersey: Pearson Prentice Hall, 2010. 12th ed. 13, 14

HIGUCHI, T.; SUZUMORI, K.; TADOKORO, S. **Next-generation actuators leading breakthroughs**. London, UK: Springer, 2010. 2

IDA, N. **Sensors, actuators, and their interfaces**: a multidisciplinary introduction. United Kingdom: Scitech Publishing, 2014. 1

JAZWINSKI, A. H. **Stochastic processes and filtering theory**. New York: Academic Press, 1970. 30

JEON, S. W.; JUNG, S. Hardware-in-the-loop simulation for the reaction control system using pwm-based limit cycle analysis. **IEEE Transactions on Control Systems Technology**, v. 20, n. 2, p. 538–545, 2012. 4

JIN, J.; PARK, B.; PARK, Y.; TAHK, M. Attitude control of a satellite with redundant thrusters. **Aerospace Science and Technology**, v. 10, n. 7, p. 644–651, 2006. 4

JOHNSON, M. A.; MORADI, M. H. **PID control**: new identification and design methods. London, UK: Springer, 2005. 543 p. 19

KRISTIANSEN, R.; HAGEN, D. Modelling of actuator dynamics for spacecraft attitude control. **Journal of Guidance, Control, and Dynamics**, v. 32, n. 3, p. 1022–1025, 2009. 20, 60

L-3 COMMUNICATIONS SPACE & NAVIGATION. **RWA-15 - High Torque Reaction Wheel Assembly**. 2014. Available from: <`www2.l-3com.com/spacenav/space_and_nav/space_products/RWA-15.htm`>. Access in: December 20th, 2014. 24

LAU, V.; DE SOUZA, F. L.; GALSKI, R. L.; ROCCO, E. M.; BECCENERI, J. C.; DOS SANTOS, W. A.; SANDRI, S. A. A multidisciplinary design optimization tool for spacecraft equipment layout conception. **Journal of Aerospace Technology and Management**, v. 5, n. 4, p. 431–446, 2014. 4

LEY, W.; WITTMANN, K.; HALLMANN, W. **Handbook of space technology**. United Kingdom: John Wiley & Sons, 2009. 3, 21, 25

LUO, Y.; LEI, Y.; TANG, G. Optimal multi-objective nonlinear impulsive rendezvous. **Journal of Guidance, Control, and Dynamics**, v. 30, n. 4, p. 994–1002, 2007. 4

MA., O.; FLORES-ABAD, A.; BOGE, T. Use of industrial robots for hardware-in-the-loop simulation of satellite rendezvous and docking. **Acta Astronautica**, v. 81, n. 1, p. 335–347, 2012. 4

MACALA, G. A.; LEE, A. Y.; WANG, E. K. Feasibility study of two cassini reaction wheel/thruster hybrid controllers. **Journal of Spacecraft and Rockets**, v. 51, n. 2, p. 574–585, 2014. 3

MARCELINO, E. W. **Control of Orbital Trajectory in Maneuvers with Continuous Thrust of Long Term (in portuguese)**. 186 p. Dissertation (Master of Science in Space Mechanics and Control) — Instituto Nacional de Pesquisas Espaciais (INPE), São José dos Campos, 2009. 43

MARLER, R. T.; ARORA, J. S. Survey of multi-objective optimization methods for engineering. **Structural and Multidisciplinary Optimization**, v. 26, n. 6, p. 369–395, 2004. 4, 38, 39

MARTEL, F. Optimal 6 axis command of a space vehicle with a precomputed thruster selection catalogue table. In: INTERNATIONAL SYMPOSIUM ON SPACE FLIGHT DYNAMICS, ESA SP-548., 2004, Munich, Germany. **Proceedings...** Munich: ESA, 2004. 23

MORADI, R.; POURTAKDOUST, S. H.; KAMYAR, R. Optimal coupled spacecraft rendezvous and docking using multi-objective optimization. In: BIENNIAL CONFERENCE ON ENGINEERING SYSTEMS DESIGN AND ANALYSIS, ESDA2010-24847., 2010, Istambul, Turkey. **Proceedings...** Istambul, Turkey: ASME, 2010. 4

NASH JR., J. F. The bargaining problem. **Econometrica**, v. 18, n. 2, p. 155–162, 1950. 38

OGATA, K. **Modern control engineering**. 5th. ed. Upper Saddle River, New Jersey: Prentice hall, 2010. 912 p. 47, 49

OLIVEIRA, T. C.; ROCCO, E. M.; FERREIRA, J. L.; PRADO, A. F. B. A. Minimum fuel low-thrust for satellites using a permanent magnet hall thruster. **Mathematical Problems in Engineering**, v. 2013, 2013. 43

PARETO, V. **Manuale de economia politica**. New York: Societa Editrice Libraria, 1992. Translated into English by A. S. Schwier as "Manual of political economy", edited by A. S. Schwier and A. N. Page, A.M. Kelley. 36

PENA, R. S. S.; ALONSO, R.; ANIGSTEIN, P. A. Robust optimal solution to the attitude/force control problem. **IEEE Transactions on Aerospace and Electronic Systems**, v. 36, n. 3, p. 784–792, 2000. 23

PRESS, W. H.; TEUKOLSKY, S. A.; VETTERLING, W. T.; FLANNERY, B. P. **Numerical recipes**: the art of scientific computing. Cambridge, UK: Cambridge University Press, 2007. 3rd. ed. 22

PROTTER, M. H.; MORREY JR., C. B. **College calculus with analytic geometry**. [S.l.]: Addison-Wesley, 1970. 2nd ed. 41

ROBERTS, B. A.; KRUK, J. W.; AKE, T. B.; ENGLAR, T. S.; CLASS, B. F.; ROVNER, D. M. Three-axis attitude control with two reaction wheels and magnetic torquer bars. In: GUIDANCE, NAVIGATION, AND CONTROL CONFERENCE AND EXHIBIT, AIAA 2004-5245., 2004, Providence, Rhode Island. **Proceedings...** Providence: AIAA, 2004. 3

ROCCO, E. M. **Manutenção orbital de constelações simétricas de satélites utilizando manobras impulsivas ótimas com vínculo de tempo**. 177 p. Thesis (Doctorate in Space Engineering and Technology) — Instituto Nacional de Pesquisas Espaciais (INPE), São José dos Campos, 2002. 38, 41

ROCCO, E. M. Perturbed orbital motion with a pid control system for the trajectory. In: BRAZILIAN COLLOQUIUM ON ORBITAL DYNAMICS, 2008, Águas de Lindóia, Brazil. **Proceedings...** Águas de Lindóia: CBDO, 2008. 42

ROCCO, E. M.; SOUZA, M. L. O.; PRADO, A. F. B. A. Multi-objective optimization approach apply of the station keeping of satellite constellations. **Advances in the Astronautical Sciences**, v. 109, p. 641–656, 2002. 4

_____. Multi-objective optimization applied to satellite constellations i: Formulation of the smallest loss criterion. In: INTERNATIONAL ASTRONAUTICAL CONGRESS, IAC-03-A.3.01., 2003, Bremen, Germany. **Proceedings...** Bremen: IAC, 2003. 41, 42

_____. Further application of the smallest loss criterion in the multi-objective optimization of a satellite constellation. In: INTERNATIONAL ASTRONAUTICAL CONGRESS, 2005, Fukuoka, Japan. **Proceedings...** Fukuoka: IAC, 2005. p. 3165–3172. 41

_____. Multi-objective optimization applied to satellite constellation ii: Initial applications of the smallest loss criterion. In: INTERNATIONAL WORKSHOP ON SATELLITE CONSTELLATIONS AND FORMATION FLYING, 2005, São José dos Campos, Brazil. **Proceedings...** São José dos Campos: INPE, 2005. p. 123–132. 41

_____. Station keeping of constellations using multiobjective strategies. **Mathematical Problems in Engineering**, v. 2013, 2013. 41

SCHILLING, D. A.; REVELLE, C.; COHON, J. An approach to the display and analysis of multiobjective problems. **Socio-Economic Planning Sciences**, v. 17, n. 2, p. 57–63, 1983. 65, 68

SERVIDIA, P. A.; NA, R. S. P. Spacecraft thruster control allocation problems. **IEEE Transactions on Automatic Control**, v. 50, n. 2, p. 245–249, 2005. 3

SHAHROKNI, A.; DRUMMOND, P.; FUA, P. Texture boundary detection for real-time tracking. In: EUROPEAN CONFERENCE ON COMPUTER VISION, 2004, Prague, Czech Republic. **Proceedings...** Prague: Springer Berlin Heidelberg, 2004. p. 566–577. 109

SIDI, M. J. **Spacecraft dynamics and control**: a practical engineering approach. Cambridge, UK: Cambridge University Press, 1997. 3, 10, 13, 14, 16, 19, 21, 22, 24, 25, 26, 27, 82

SILANI, E.; LOVERA, M. Magnetic spacecraft attitude control: A survey and some new results. **Control Engineering Practice**, v. 13, n. 3, p. 357–371, 2005. 26

SILVA, N.; MARTEL, F.; DELPY, P. Automated transfer vehicle thrusters selection and management function. In: INTERNATIONAL ESA CONFERENCE

ON GUIDANCE, NAVIGATION AND CONTROL SYSTEMS, ESA SP-606., 2006, Greece. **Proceedings...** Greece: ESA, 2006. 3

SOBEL, I.; FELDMAN, G. A 3x3 isotropic gradient operator for image processing. **A talk at the Stanford Artificial Project**, p. 271–272, 1968. 109

SPACE RESEARCH ON UNIQUE TECHNOLOGY. **Satellite System**. 2014. Available from: <`sat.aero.cst.nihon-u.ac.jp/sprout-e/1-System-e.html`>. Access in: December 20th, 2014. 26

SUTTON, G. P.; BIBLARZ, O. **Rocket propulsion elements**. New York: John Wiley & Sons, 2001. 7th ed. 24, 82

TEWARI, A. **Modern control design**: with matlab and simulink. West Sussex, England: John Wiley & Sons Ltd., 2002. 518 p. p. 49

_____. **Atmospheric and space flight dynamics**: modeling and simulation with matlab and simulink. New York, USA: Birkhauser Boston, 2007. 556 p. p. 14, 15, 17, 18

VENDITTI, F. C. F.; ROCCO, E. M.; PRADO, A. F. B. A. Trajectory control around non-spherical bodies modelled by parallelepipeds. **Journal of Physics**, v. 465, n. 1, 2013. 43

VENDITTI, F. C. F.; ROCCO, E. M.; PRADO, A. F. B. A.; SUHKANOV, A. Gravity-assisted maneuvers applied in the multi-objective optimization of interplanetary trajectories. **Acta Astronautica**, v. 67, p. 1255–1271, 2010. 4

WANG, M.; XIE, Y. Design of the optimal thruster combinations table for the real time control allocation of spacecraft thrusters. In: CONFERENCE ON DECISION AND CONTROL, 2009, Shangai, China. **Proceedings...** Shangai: IEEE, 2009. p. 5063–5068. 3

WERTZ, J. H. **Spacecraft attitude determination and control**. Boston, MA: Reidel Publishing Company, 1978. 858 p. p. 26, 27

WIE, B. **Space vehicle dynamics and control**. Reston, VA: American Institute of Aeronautics and Astronautics, Inc., 1998. 662 p. 14

WIKTOR, P. J. Minimum control authority plot: A tool for designing thruster systems. **Journal of Guidance, Control, and Dynamics**, v. 17, n. 5, p. 998–1006, 1994. 4

WON, C. Comparative study of various control methods for attitude control of a leo satellite. **Aerospace Science and Technology**, v. 3, n. 5, p. 323–333, 1999. 3

YAMANAKA, K.; ANKERSEN, F. New state transition matrix for relative motion on an arbitrary elliptical orbit. **Journal of Guidance, Control and Dynamics**, v. 25, n. 1, p. 60–66, 2002. 11

ZHANG, X.; ZENG, M. Multi-objective control of spacecraft attitude maneuver based on takagi-sugeno fuzzy model. **Journal of Control Engineering and Applied Informatics**, v. 14, n. 1, p. 31–36, 2012. 4

PUBLICAÇÕES TÉCNICO-CIENTÍFICAS EDITADAS PELO INPE

Teses e Dissertações (TDI)

Teses e Dissertações apresentadas nos Cursos de Pós-Graduação do INPE.

Notas Técnico-Científicas (NTC)

Incluem resultados preliminares de pesquisa, descrição de equipamentos, descrição e ou documentação de programas de computador, descrição de sistemas e experimentos, apresentação de testes, dados, atlas, e documentação de projetos de engenharia.

Propostas e Relatórios de Projetos (PRP)

São propostas de projetos técnico-científicos e relatórios de acompanhamento de projetos, atividades e convênios.

Publicações Seriadas

São os seriados técnico-científicos: boletins, periódicos, anuários e anais de eventos (simpósios e congressos). Constam destas publicações o Internacional Standard Serial Number (ISSN), que é um código único e definitivo para identificação de títulos de seriados.

Pré-publicações (PRE)

Todos os artigos publicados em periódicos, anais e como capítulos de livros.

Manuais Técnicos (MAN)

São publicações de caráter técnico que incluem normas, procedimentos, instruções e orientações.

Relatórios de Pesquisa (RPQ)

Reportam resultados ou progressos de pesquisas tanto de natureza técnica quanto científica, cujo nível seja compatível com o de uma publicação em periódico nacional ou internacional.

Publicações Didáticas (PUD)

Incluem apostilas, notas de aula e manuais didáticos.

Programas de Computador (PDC)

São a seqüência de instruções ou códigos, expressos em uma linguagem de programação compilada ou interpretada, a ser executada por um computador para alcançar um determinado objetivo. Aceitam-se tanto programas fonte quanto os executáveis.